Laser Cooling and Trapping of Rubidium using a Narrow Transition

A
Thesis submitted
in Partial Fulfilment of the Requirements
for the Degree of

Doctor of Philosophy

by

Rajnandan Choudhury Das

Department of Physics
Indian Institute of Technology Guwahati
Guwahati, Assam - 781039

May, 2024

Dedicated to

Maa, **Deota**, and **Bhaiti**

DECLARATION

I, hereby, declare that the thesis entitled **"Laser Cooling and Trapping of Rubidium using a Narrow Transition"**, submitted by me to the Indian Institute of Technology Guwahati, for the award of the degree of Doctor of Philosophy, is a bonafide work carried out by me under the supervision of Dr. Kanhaiya Pandey. The content of this thesis, in full or in parts, has not been submitted to any other University or Institute for the award of any degree or diploma. I also wish to state that to the best of my knowledge and understanding, nothing in this report amounts to plagiarism.

Rajnandan Choudhury Das
Roll No. 186121020,
Department of Physics,
Indian Institute of Technology Guwahati,
Guwahati, Assam - 781039

CERTIFICATE

This is to certify that the thesis entitled **“Laser Cooling and Trapping of Rubidium using a Narrow Transition”**, submitted by **Rajnandan Choudhury Das** (186121020), a Ph.D. scholar in the Department of Physics, Indian Institute of Technology Guwahati, for the award of the degree of Doctor of Philosophy, is a record of an original research work carried out by him under my supervision and guidance. The thesis has fulfilled all requirements as per the regulations of the institute and in my opinion, has reached the standard needed for submission. The results embodied in this thesis have not been submitted to any other University or Institute for the award of any degree or diploma.

Dr. Kanhaiya Pandey
Department of Physics,
Indian Institute of Technology Guwahati,
Guwahati, Assam - 781039

ACKNOWLEDGEMENTS

I begin by expressing my gratitude to my supervisor, Dr. Kanhaiya Pandey, for his guidance and mentorship throughout my Ph.D. journey. His expertise, feedback, patience, and support have significantly contributed to the successful completion of my thesis. His dedication to building and developing the lab, along with his impressive analytical skills, reasoning abilities, mathematical expertise, and his teaching, have always motivated me. I sincerely appreciate his enduring impact on my academic and personal development.

I also express my gratitude to the members of my doctoral committee, Dr. Pankaj Kumar Mishra, Prof. Ashwini Kumar Sharma, and Prof. Gagan Kumar, for their insightful guidance and constructive feedback. I also acknowledge the earlier contribution of Dr. Tapan Mishra, whose insights shaped the direction of my research. Collectively, I express my gratitude to each committee member for enriching my doctoral experience.

I appreciate the support and motivation from Prof. Perumal, Prof. Subhradeep Ghosh, Prof. Alika Khare, Dr. Subhaditya Bhattacharya, and Prof. Tarak Nath Dey. Their mentorship and engaging discussions have significantly enriched my research endeavors. I am grateful to Prof. Vasant Natarajan, Prof. Gagan Kumar, Prof. Alika Khare, and Prof. Anugrah Singh for allowing me to borrow various instruments from their lab, whenever needed.

I am grateful to IIT Guwahati for the necessary support, facilities, and resources, including the Institute Fellowship and access to the Central Workshop. Special thanks to the Ministry of Education for the Prime Minister's Research Fellowship (PMRF), which provided financial stability and motivation.

To my lab members, Dr. Ogaro, Dr. Dangka, Thilagaraj, Arka, Heramb, Samir, Samrat, Chirantan, Deepak, and Dr. Bilal, thank you for the collaborative efforts that enhanced my academic experience. This thesis would have never been completed without you. Special thanks to Dr. Ogaro and Dr. Dangka for their guidance during my initial days, imparting crucial details about the experiments. I extend my appreciation to Arka and Samir for their tireless day and night support in the experimental work. Thilagaraj and Heramb, your ability to extract vital information whenever needed and your hard work in ordering and constructing various experiment components have been instrumental.

I appreciate the support from all my batchmates especially Debu, Monu, Suchitji, Bhagwan, Prantik, Mandira, and Angana, starting from our coursework days right from day one. A special thanks to Debu and Monu for providing emotional support and motivation whenever needed. Gratitude extends to the huge cricket group, including Debu 2.0, Vishal, Sanu, Shailesh, Shivam, Dipu, Ankan, Mijjanur, Pranjal, Nayan, Ravinder, Bhagwat, Shoaib, Subhankar, Sanket Da, Ravi, Lwithwsa, Biraj, Shanku, NmB da, Shekhar Da, Deepak Bhaiya, Ankush Bhaiya, Amit and Aniruddha, for the countless matches in LPL, PPL, CL, IPL, ISPL or random, and for the friendships that enriched my PhD journey. The numbers 117M-1670R-114W-285J have kept me motivated throughout this long journey; without them, submitting the thesis might have been challenging.

A sincere thanks goes out to Sampreet Da, who goes beyond the boundaries of friendship, acting more like a true brother. His support, always ready and selfless, extends beyond the typical bonds of friendship. Sampreet Da's guidance, care, and kindness have made a significant impact, and I feel blessed to have him accompanying me during my Ph.D. journey.

I want to express my gratitude to all my teachers from Sankardev Sishu Vidya Niketan Ambari, Cotton College, and Impact Education Centre. Umesh Sir's help with physics made me really like the subject, and Manav Sir's guidance at a critical time was really important. All my teachers have played a big part in my education. I owe them a lot for making me love learning and reaching this academic milestone.

I am profoundly grateful to Upasana for being my constant source of support and inspiration during my entire Ph.D. journey, through both the highs and lows. Her consistent encouragement, patience, and understanding made the tough times easier and the successes more enjoyable. Her presence brought a sense of comfort to the often solitary path of doctoral studies and personal well-being. I owe a significant portion of my success to her steadfast companionship, and I am profoundly thankful for having her by my side on this remarkable journey.

Finally, to my incredible parents and my brother, your unwavering encouragement, boundless support, and belief have been my guiding lights throughout this journey. The results of your collective hard work and sacrifices are now vividly evident in this moment. Words fall short of expressing the immeasurable impact of your guidance and the independence you graciously granted me. This achievement is not just mine; it stands as a testament to the enduring support and sacrifices of all three of you.

PUBLICATIONS

List of publications resulting from the work reported in this thesis:

[**1**] Rajnandan Choudhury Das, Dangka Shylla, Arkapravo Bera, and Kanhaiya Pandey, *"Narrow-line cooling of* ^{87}Rb *using* $5S_{1/2} \rightarrow 6P_{3/2}$ *open transition at 420 nm"*, Journal of Physics B: Atomic, Molecular and Optical Physics **56**, 025301 (2023) [1].

[**2**] Rajnandan Choudhury Das, Samir Khan, Thilagaraj Ravi, and Kanhaiya Pandey, *"Direct spectroscopy of Rubidium using a narrow-line transition at 420 nm"*, The European Physical Journal D **78**, 40 (2024) [2].

[**3**] Rajnandan Choudhury Das, Thilagaraj R, Samir Khan, and Kanhaiya Pandey, *"Continuous loading of magneto-optical trap of Rb at narrow transition", Physical Review A (2024) (accepted)* [3].

[**4**] Rajnandan Choudhury Das, Samir Khan, Thilagaraj R, and Kanhaiya Pandey, *"Role of spontaneously generated coherence (SGC) in laser cooling of atoms"* [4] (under review).

Additional publications:

[**1**] Dangka Shylla, Elijah Ogaro Nyakang'o, Rajnandan Choudhury Das, and Kanhaiya Pandey, *"Effect of detuning on velocity induced population oscillation"*, The European Physical Journal D **76**, 125 (2022) [5].

[**2**] Dangka Shylla, Rajnandan Choudhury Das, and Kanhaiya Pandey, *"Atomic coherence based multi lasers interferometry"* (under preparation).

ABSTRACT

Laser cooling and trapping serve as a crucial gateway, offering insights into fundamental physics and opening the way for diverse quantum technologies. Among the various elements, Rb is one of the most extensively studied elements in atomic physics. Until now, the cold atom community has mainly used Infrared lasers to cool and trap Rb atoms in Magneto-optical trap (MOT), usually through the $5S_{1/2} \rightarrow 5P_{3/2}$ transition at 780 nm. In this thesis, we explore the laser cooling and trapping of Rb atoms in MOT using the $5S_{1/2} \rightarrow 6P_{3/2}$ narrow-line transition at 420 nm (blue MOT). Despite its large branching ratio, we observe efficient cooling with the 420 nm transition, achieving around 10^8 atoms in the blue MOT at a typical temperature of 54 μK. We also present a method for the continuous loading of Rb atoms in the blue MOT and a theoretical framework for cooling atoms with two simultaneous transitions. We also describe the direct spectroscopy of Rb at 420 nm, which is challenging due to its weak transition strength. Furthermore, we numerically analyze the role of spontaneously generated coherence (SGC) in polarization gradient cooling with $F = 1 \rightarrow 2$ transition and investigate the feasibility of blue-detuned cooling at this transition in the absence of SGC. We experimentally demonstrate blue detuned cooling in type-I and type-II MOT. Additionally, we study various configurations of red-detuned as well as blue-detuned blue MOT, achieving temperatures as low as 24 μK in D_1 MOT and 31 μK in D_2 MOT. Our studies may find applications in quantum technologies based on the narrow-line cooling transitions.

Permissions and Attributions

- The content of Chapter 4 is based on the following work
  - Eur. Phys. J. D **78**, 40 (2024) in collaboration with Samir Khan, Thilagaraj Ravi, and Kanhaiya Pandey
- The content of Chapter 5 is based on the following work
  - J. Phys. B: At. Mol. Opt. Phys. **56** 025301 (2023) in collaboration with Dangka Shylla, Arkapravo Bera, and Kanhaiya Pandey
- The content of Chapter 6 is based on the following work
  - Phys. Rev. A (2024) (accepted) in collaboration with Thilagaraj Ravi, Samir Khan, and Kanhaiya Pandey
- The content of Chapter 7 is based on the following work
  - arXiv:2401.04234 [physics.atom-ph] in collaboration with Samir Khan, Thilagaraj R, and Kanhaiya Pandey

Contents

List of Figures

List of Tables

Chapter 1

Introduction

Contents

1.1 Introduction

Laser cooling stands as a revolutionary technique in atomic physics. It employs the mechanical effects of light to manipulate and control the motion of atoms [6, 7, 8, 9, 10, 11]. This method is rooted in the transfer of momentum from the laser to the atoms, inducing a force that counteracts their motion, resulting in the reduction of temperature. In three-dimensional space, atoms can move in six different directions. Thus for laser cooling in three-dimensional space, three pairs of counterpropagating laser beams form orthogonal directions are commonly used. This configuration of the laser-cooled cloud is termed optical molasses (OM). The OM encounters a limitation - atoms in this configuration, despite being cooled, diffuse away due to insufficient spatial confinement. To address this issue, a trapping force is required. This is done by using a quadrupole magnetic field. This force creates a three-dimensional trapping potential, effectively holding the laser-cooled atoms at the center of the trap. The combination of laser cooling and the trapping force gives rise to the Magneto-Optical Trap (MOT).

The journey towards achieving cold atoms through laser cooling and trapping is a crucial gateway, offering insights into fundamental physics and paving the way for diverse quantum technologies. These technologies are used in various applications, ranging from atomic sensors to quantum computers [12, 13, 14], quantum simulators [15, 16], atomic clocks [17, 18]. The 1997 Nobel Prize in Physics, awarded to Prof. Steven Chu, Prof. Claude Cohen-Tannoudji, and Prof. William D. Phillips, marked the initiation of global efforts to cool various atoms, revealing unique properties and pathways for exploration [7, 19, 20, 21].

Among the various elements, Rubidium (Rb) is one of the easiest atoms to handle in atomic physics. It is one of the most extensively studied atoms in atomic physics. Until now, cold atom community have mainly used Infrared (IR) lasers to cool and trap Rb atoms in MOT, usually through the $5S_{1/2} \rightarrow 5P_{3/2}$ transition at 780 nm. Despite Rb's accessibility and versatility, the loading process has been limited to IR lasers. As quantum technologies advance, there is a growing need to explore new loading techniques for Rb. Utilizing the well-known properties of Rb and its easy manipulation makes it an ideal candidate for pushing the boundaries of MOT loading methods.

Laser cooling and trapping of atoms in MOT, although exceptionally effective, encounters a fundamental limit known as the Doppler temperature [6]. This limit is the minimum achievable temperature in MOT, preventing them from reaching absolute zero. It is given by:

$$T_{\mathrm{D}} = \hbar\Gamma/2k_{\mathrm{B}} \tag{1.1}$$

Here, Γ represents the linewidth of the transition, $\hbar$ is the reduced Planck's constant, and k_{B} is the Boltzmann constant.

To attain temperatures below T_{D}, commonly referred to as sub-Doppler temperatures, additional sub-Doppler cooling techniques, such as polarization-gradient cooling (PGC), and Raman Sideband cooling are employed. For certain elements like Li and K, where PGC proves ineffective due to their closely spaced hyperfine levels, the gray molasses (GM) technique has emerged as a reliable approach to achieve sub-Doppler temperatures [22, 23, 24, 25, 26, 27, 28, 29, 30]. The GM technique is also extensively applied in various other elements such as Na [31, 32], Rb [33, 34], Cs [35, 36], He [37], and Cr [38].

Although these sub-Doppler cooling techniques are powerful, they come with challenges and complexities. In sub-Doppler cooling, the MOT quadrupole magnetic field needs to be switched off. Without the MOT quadrupole magnetic field, the atoms do not have the trapping force. As a result, the cloud expands, cloud density decreases, and becomes inefficient for loading into the optical dipole trap (ODT) for evaporative cooling. Further, expansion of the cloud causes a gain in the potential energy for subsequent capture in a magnetic quadrupole trap [39]. For efficient transfer to a magnetic trap, the cloud size should be small. Additionally, sub-Doppler cooling is very fragile to the magnetic fields [40, 41, 42, 43, 44, 45]. It requires magnetic shielding and/or active cancellation to maintain zero stray magnetic fields. It also requires careful balance and optimization of cooling beam intensity and detuning, adding to the experimental complexity.

The significance of Eq. 1.1 becomes apparent as it reveals that the Doppler temperature is directly proportional to the linewidth of transitions. This implies that lower temperatures can be achieved by using narrow-line cooling transitions. Unlike sub-Doppler cooling, laser cooling and trapping at narrow transition ensures that atoms remain trapped in the MOT, which is very useful for loading into the ODT for evaporative cooling and also for atom interferometry [46]. Utilizing levels with different principal quantum numbers becomes a feasible choice for achieving narrow transitions. This is due to the smaller electric dipole matrix element between these levels, resulting from the reduced overlap of their wave functions. Consequently, this reduced overlap makes the transition weak or narrow, offering an advantageous approach for enhancing the cooling efficiency in laser cooling experiments.

Even though there is a preference for narrow-line cooling transitions to achieve lower temperatures, a noteworthy trade-off arises in terms of the capture velocity in the MOT, which is directly proportional to the linewidth of the transition. This implies that for efficient loading of a large number of atoms into the MOT, a broad linewidth transition is preferable. However, to attain lower temperatures, a narrow linewidth transition is favored. To manage this trade-off, a two-stage MOT strategy is employed. In the initial stage, the MOT is loaded using a transition with a broad linewidth, and subsequently, the atoms are transferred to a narrow-line MOT to achieve lower temperatures. This two-stage MOT approach has been successfully employed across various elements, including Ca [47, 48], Sr [49, 50], Yb [51, 52], Dy [53, 54], Er [55, 56, 57], Cd [58], and Eu [59]. In the context of alkali atoms, narrow-line cooling has been demonstrated in Li using the $2S_{1/2} \rightarrow 3P_{3/2}$ transition at 323 nm [60, 61], and in K using the $4S_{1/2} \rightarrow 5P_{3/2}$ transition at 405 nm [62]. Furthermore, its superiority over GM for loading atoms into an ODT has been demonstrated in Li [63].

Returning to Rb, its $5S_{1/2} \rightarrow 5P_{3/2}$ transition at 780 nm has been extensively explored, both in spectroscopy as well as in laser cooling. Interestingly, the $5S_{1/2} \rightarrow 6P_{3/2}$ transition at 420 nm has received relatively less attention, despite its clear advantages - most notably, a significantly narrower linewidth ($2\pi \times 1.4$ MHz) compared to conventional IR transitions ($2\pi \times 6$ MHz). This blue transition finds applications in various domains such as Rydberg excitation of Rb atoms [64, 65, 66, 67, 68], quantum gate implementations [69], improved atom interferometers [70], compact Rb optical frequency standards [71], creation of narrow-bandwidth Faraday optical filters [72, 73], demonstration of non-linear magneto-optical rotation [74], and the study of various atomic systems [5, 75, 76, 77].

One of the most promising advantages is the lower Doppler temperature achievable with the 420 nm transition. The Doppler temperature of Rb in a MOT at 780 nm is 146 μK, whereas, at 420 nm, it reduces to 34 μK, nearly four times lower. This transition may present promising opportunities for achieving lower-temperature MOTs for Rb. Even though the narrow line cooling works in Li and K, it is uncertain that it will work in Rb due to its large branching ratio. It is important to experimentally demonstrate the temperature reduction in the narrow-line cooling of Rb and it forms the core focus of our work.

The strategy involves a two-stage MOT, where atoms are initially cooled and trapped using the $5S_{1/2}$, F $= 2 \rightarrow 5P_{3/2}$, F $= 3$ transition at 780 nm and subsequently transferred to the MOT at 420 nm using the $5S_{1/2}$, F $= 2 \rightarrow 6P_{3/2}$, F $= 3$ transition. Throughout this thesis, we refer to the MOTs as the IR MOT for the IR transition at 780 nm and the blue MOT for the narrow-line cooling transition at 420 nm. Remarkably, this approach traps approximately 10^8 Rb atoms at a typical temperature of 54(10) μK. Despite the open transition nature and a large branching ratio, the blue MOT demonstrates efficient cooling, even with a repumper laser at 780 nm.

In narrow-line MOT, the conventional approach separates the two key steps in time. In the first step, atoms are loaded in MOT using broad transition, and in the second step, they are transferred to the MOT at narrow line transition. However, an alternative method involves converting these steps in time into steps in space, which enables the continuous loading of atoms into the narrow-line MOT. This technique has proven crucial in producing the continuous Bose-Einstein Condensate (BEC) of Sr [78]. The concept of continuous loading in MOTs, particularly at narrow transitions, holds considerable promise for generating a continuous beam of cold atoms at lower temperatures. This continuous loading approach may present an advantage for atomic-based quantum sensors by eliminating dead time.

The realization of loading of continuous MOT at narrow transitions, pre-cooled by broad transitions, has been successfully demonstrated for certain elements such as Yb [51], Sr [78], and Dy [54]. For these elements, the ratio of the linewidth of broad to narrow transition is in order of magnitude. Notably, in the case of Yb, continuous loading at narrow transitions outperforms the broader transitions in terms of both number of atoms and temperature reduction [51, 79, 80]. Yb MOTs driven by broader transitions even in the presence of repumper lasers tend to exhibit lower atom numbers as compared to the narrow transitions [81]. Although narrow-line cooling has been realized in Li [60], K [62], and Rb [1, 82], continuous loading for alkali atoms is yet to be demonstrated.

We employ a core-shell MOT configuration similar to Yb [79], where a significant advantage was reported. This technique involves creating a hole in the core of the laser beam driving the broad transition, subsequently filled by the laser beam at the narrow transition. The relative dimensions of the core and the filling beam are crucial and depend on the ratio of the linewidths of the broad and narrow transitions. Yb presents a distinctive characteristic with a broad linewidth to narrow linewidth ratio of approximately 150. Consequently, in the case of Yb, optimal efficiency is achieved when the core is precisely filled. This is attributed to the fact that in the presence of the broad linewidth transition, the weak transition laser (with intensity comparable to the saturation intensity) does not significantly influence temperature reduction. In contrast, alkali atoms exhibit a considerably lower ratio of approximately $4-5$. Under these conditions, a larger filling area is required as compared to the core area. The significance of this lies in the overlapped region, where the narrow transition linewidth plays an important role in temperature reduction, even in the presence of the broad transition.

We present a method for continuous loading of Rb atoms in the narrow-line MOT. This is achieved by using the 780 nm laser addressing the $5S_{1/2}$, F = 2 → $5P_{3/2}$, F = 3 transition and the 420 nm laser addressing the $5S_{1/2}$, F = 2 → $6P_{3/2}$, F = 3 transition. In the IR MOT beam, we make a hollow core. Then, we place the blue laser beam inside this hollow core of the IR MOT beam. Using this technique, we load around 10^8 Rb atoms continuously in the blue MOT. We study the behavior of the blue MOT with various parameters such as magnetic field gradient, detuning, power and diameter of blue MOT beam, and the spot inside the IR MOT beam.

Furthermore, it is important to note that the atomic transitions are classified into two categories: type-I transition ($F_g \rightarrow F_e = F_g + 1$) and type-II transition ($F_g \rightarrow F_e \leq F_g$). Here F_g and F_e are the ground state and excited state angular momentum, respectively. A vast majority of MOT uses type-I transitions, and this MOT is therefore known as type-I MOT. Atoms can also be cooled and trapped in MOT using a type-II transition. The distinction between these systems becomes particularly relevant when considering the Doppler and sub-Doppler cooling techniques. While both systems utilize red-detuned light for initial Doppler cooling, the sub-Doppler cooling conditions differ. Systems with type-I transition still require red-detuned light for sub-Doppler cooling, as the signs of the Doppler and sub-Doppler forces are the same. In contrast, systems with type-II transition, due to the opposite sign of these forces, require blue-detuned light for effective sub-Doppler cooling [44, 45].

In a system with type-I transitions, PGC is suppressed by the magnetic fields, whereas in the case of type-II transitions, PGC remains effective even in the presence of magnetic fields of the MOT [44, 45]. Consequently, blue-detuned cooling works in type-II transitions, and is demonstrated with significant advantages in Rb experiments [45, 83, 84]. Blue-detuned MOTs have also been successfully demonstrated in molecules, and it has become a crucial tool for experiments involving cold atomic molecules [85, 86, 87, 88]. It is important to note that while blue-detuned cooling works in type-II MOTs, its efficacy is notably absent in type-I MOTs.

The sensitivity of PGC in type-I systems to magnetic fields can be attributed to the important role of spontaneously generated coherence (SGC) in sub-Doppler cooling mechanisms. These mechanisms depend on multi-level atomic systems [89, 90]. SGC holds a crucial role in the field of spectroscopy and has been the subject of extensive investigation within multi-level atomic systems [91, 92, 93, 94, 95, 96, 97, 98, 99]. As laser cooling and the atomic spectrum profile are related to each other, it becomes apparent that SGC is a significant factor in laser cooling processes. The spontaneous decay of atoms from an excited state typically occurs due to the interactions with the different modes of the vacuum field. SGC can arise from two scenarios. First, when the same vacuum mode drives two transitions simultaneously, it can create a spontaneously generated coherence between the ground states due to the decay of the population [100]. Secondly, when the same vacuum mode drives two transitions simultaneously, coherence between the excited states transfers to the ground states, resulting in spontaneously generated coherence between the ground states [96]. SGC is particularly sensitive to magnetic fields, as it occurs when the energy difference between the excited and ground states is nearly equal. In the absence of magnetic fields, the degeneracy of Zeeman levels allows for effective SGC and, consequently, efficient PGC. Conversely, in the presence of a magnetic field, the degeneracy of the Zeeman levels is lifted, averaging out the effect of SGC and making PGC fragile to magnetic fields.

To understand the role of SGC in laser cooling, we employ a numerical analysis using the density matrix. Specifically, we concentrate on the $F_g = 1 \rightarrow F_e = 2$ transition to understand the Doppler and sub-Doppler forces in the context of SGC. Our primary objective is to investigate the possibility of achieving blue-detuned cooling in this transition. Additionally, we conduct experiments to demonstrate the blue-detuned cooling in both type-I transition and type-II transition using the blue MOT of Rb. We demonstrate various configurations of red-detuned as well as blue-detuned blue MOT and compare their temperatures. Notably, we achieve temperatures as low as 24 μK in the D_1 MOT and 31 μK in the D_2 MOT.

In summary, this thesis represents a comprehensive exploration of laser cooling and trapping of Rb atoms in MOT using the $5S_{1/2} \rightarrow 6P_{3/2}$ narrow-line transition at 420 nm. We begin with the direct spectroscopy of Rb using the narrow-line transition at 420 nm, which is challenging due to its weak transition strength. We demonstrate the blue MOT of Rb utilizing this narrow-line transition. We observe that narrow-line cooling works in Rb blue MOT. Further, we present a method for the continuous loading of Rb atoms in the blue MOT. We also numerically study the role of SGC in PGC in atomic systems with $F_g = 1 \rightarrow F_e = 2$ transition and investigate the possibility of blue-detuned cooling in this transition. We experimentally demonstrate the blue detuned cooling in type-I and type-II MOT. Additionally, we demonstrate various configurations of red-detuned as well as blue-detuned blue MOT and compare their temperatures.

1.2 Thesis Outlook

The organization of the thesis is outlined as follows:

Chapter 1, titled "Introduction," introduces the importance of laser cooling and trapping of atoms in MOT. It highlights the challenge of sub-Doppler cooling techniques. It outlines the motivation and structure of the thesis, providing a foundation for further exploration.

Chapter 2, titled "Theoretical Framework," explores the physics of light-atom interactions. It covers writing the Hamiltonian and Lindbladian of a system and solving the density matrix equation. It also covers a brief overview of spontaneously generated coherence (SGC) and the relationship of density matrix elements with the absorption of light by the atom, and consequently, the force experienced by the atoms. It discusses the mathematical formulation of laser cooling and trapping for different atomic systems.

Chapter 3, titled "Experimental Details," offers a concise overview of the tools and techniques utilized in the following chapters. It covers the atomic structure of Rubidium, the laser system, spectroscopy techniques, details about the MOT chamber, characterization techniques for the MOT, and an outline of the computer control system.

Chapter 4, titled "Direct Spectroscopy of Rubidium at 420 nm," begins with the significance of the 420 nm transition and covers the complexities of direct spectroscopy at the 420 nm narrow-line transition. It emphasizes saturated absorption spectroscopy (SAS) of Rb at 420 nm and examines the impact of Rb cell temperature, control beam power, and beam size on SAS dip heights and linewidths. Additionally, it presents all eight error signals of Rb for the 5S→6P transition at 420 nm and 421 nm.

Chapter 5, titled "The Blue Magneto-Optical Trap," explores the laser cooling and trapping of Rb using the narrow line transition at 420 nm. It covers the experimental setup and provides characterization of the 420 nm blue MOT. It also presents the behavior of the blue MOT with various parameters such as detuning, power of the trapping and repumper beams, and hold time.

Chapter 6, titled "Continuous Loading of the Blue MOT," begins with the concept of continuously loading atoms in the narrow-line MOT. It details the experimental setup for loading Rb atoms continuously into the blue MOT. It discusses the behavior of the blue MOT with parameters like magnetic field gradient, detuning, power, and diameter of the blue MOT beam, as well as the diameter of the hollow core inside the IR MOT beam. The theoretical framework for cooling atoms with two simultaneous transitions is also presented.

Chapter 7, titled "Role of SGC in Laser cooling," numerically investigates the role of SGC in $F = 1 \rightarrow 2$ system using the density matrix analysis. It also presents the experimental results, which show that the blue detuning cooling works in type-I and type-II transitions. It also examines the role of the repumper laser in lowering the temperature of type-I and type-II narrow-line MOT, along with exploring different configurations producing both red and blue-detuned blue MOTs of Rb.

Chapter 8, titled "Conclusions and Future Work," highlights successes in laser cooling and trapping of Rb using the 420 nm narrow-line transition. It summarizes key findings from direct spectroscopy, the experimental characterization of the 420 nm blue MOT, continuous loading of the blue MOT, and the role of spontaneously generated coherence in laser cooling. It suggests promising directions for future research.

* * *

Chapter 2

Theoretical Framework

Contents

This chapter aims to provide a basic understanding of laser cooling and trapping of atoms in a magneto-optical trap (MOT). To understand laser cooling, we explore how the force acting on an atom correlates with its velocity. For simplicity, a cooling force can be modeled as $F = -\beta v$, where β represents a positive damping coefficient. On the other hand, trapping requires a central force of the form $F = -\alpha x$, where x is the position and α is a positive constant analogous to the spring constant in simple harmonic motion.

In general, the force on an atom is related to the difference in absorption from the two counterpropagating lasers. This dependence is influenced by system characteristics, transition strengths, polarization, detuning, and Rabi frequency of the lasers driving multiple transitions. Knowing these parameters allows the derivation of absorption of light by the atoms through the density matrix approach. This involves specifying the Hamiltonian and considering the decay of population and coherence due to spontaneous emission caused by vacuum fields. Interesting phenomena like spontaneously generated coherence (SGC) emerge when the same vacuum mode drives two transitions.

The chapter begins with the density matrix formalism. It starts with the derivation of the Hamiltonian of a two-level system, then moves towards the generalization for multi-level systems. Subsequently, the construction of the decay matrix is detailed, followed by the derivation of the relationship between density matrix elements and light absorption. The connection between force and density matrix is then derived, offering insights into the Doppler and sub-Doppler cooling mechanisms. The chapter further presents the basic structure of a MOT.

2.1 Density matrix formalism

The density matrix is a key concept in quantum mechanics. It describes an ensemble of atoms and provides a statistical description. It forms a direct link with the observable quantities, serving as a powerful mathematical tool for doing calculations and describing the behavior of the systems [6].

For a quantum system described by a pure state $|\psi\rangle$, the density operator is given by the outer product of the state vector with itself:

$$\rho = |\psi\rangle \langle\psi| \tag{2.1}$$

For a system of a statistical mixture of states $|\psi_k\rangle$, the density matrix is a weighted sum of the outer products of the pure states. It is given by:

$$\rho = \sum_k p_i |\psi_k\rangle \langle\psi_k| \tag{2.2}$$

where p_i is the probability of the system being in the pure state $|\psi_k\rangle$ and $\sum_k p_k = 1$.

The density matrix elements with respect to an orthonormal basis $|i\rangle$ are given by,

$$\rho_{ij} = \langle i| \rho |j\rangle = \sum_k p_k \langle i|\psi_k\rangle \langle\psi_k|j\rangle \tag{2.3}$$

The density matrix is a Hermitian, positive semi-definite matrix. Important properties of the density matrix are listed below:

1. $\rho^\dagger = \rho$ i.e $\rho^*_{ji} = \rho_{ij}$.
2. $\mathrm{Tr}\rho = 1$.
3. For any state χ, $|\chi\rangle \rho \langle\chi| \geq 0$.
4. For pure quantum state, $\rho^2 = \rho$ and Tr $\rho^2 = 1$.

5. For a mixed quantum state, $0 < \text{Tr}\ \rho^2 < 1$.
6. For an operator A, $\langle A \rangle = \text{Tr}(\rho A)$.

For a two-level atom with ground state $|1\rangle$ and excited state $|2\rangle$, the wavefunction can be written as $|\psi(t)\rangle = c_1(t)\,|1\rangle + c_2(t)\,|2\rangle$ and the density matrix can be written as:

$$\rho = \begin{bmatrix} \rho_{11} & \rho_{12} \\ \rho_{21} & \rho_{22} \end{bmatrix} = \begin{bmatrix} c_1(t)c_1^*(t) & c_1(t)c_2^*(t) \\ c_1^*(t)c_2(t) & c_2(t)c_2^*(t) \end{bmatrix} \tag{2.4}$$

The diagonal terms (ρ_{ii}) represent the probability of atoms to be in state, $|i\rangle$. The off-diagonal terms (ρ_{ij}) are the coherence between the states $|i\rangle$ and $|j\rangle$. Thus, the sum of the diagonal terms always gives 1. For the two-level system, the density matrix has four elements. The diagonal elements are always non-negative real numbers, and the off-diagonal elements are complex numbers. In general, for an n-level atomic system, the density matrix has n^2 elements.

2.2 Time evolution of the density matrix

The time evolution of the density matrix is governed by the Lindblad master equation given by [101, 102],

$$\dot{\rho} = -\frac{i}{\hbar}[H, \rho] + L\rho \tag{2.5}$$

Here, H is the Hamiltonian of the system, and $L\rho$ is the Lindbladian of the system. The Lindbladian accounts for the spontaneous decay of atoms. We discuss constructing the Hamiltonian and decay terms in the following sections 2.3 and 2.4. We intentionally placed these two sections after discussing methods for solving the density matrix equation. This decision is based on the fact that our approach necessitates a specific form for H and L.

The Eq. 2.5 is a system of coupled differential equations. While analytical solutions are feasible for simpler systems, for a general system, it is not easy to have an analytical solution. In our discussion, emphasis is primarily given to the numerical approach for solving the density matrix equations. There are many different ways to solve these equations numerically. In this section, we discuss one of these methods to solve these density matrix equations. This method is used throughout the works mentioned in this thesis. We first reshape the equations to reach the following form:

$$\dot{\rho} = M\rho \tag{2.6}$$

Here, ρ is a column vector of size $n^2 \times 1$ of the form $[\rho_{11}, \rho_{12}, \rho_{13}, ..., \rho_{21}, \rho_{22}, \rho_{23}, ..., \rho_{nn}]^T$ and M is a square matrix of dimension $n^2 \times n^2$ which stores the coeffiecients of the ρ of the RHS of the Eq. 2.5.

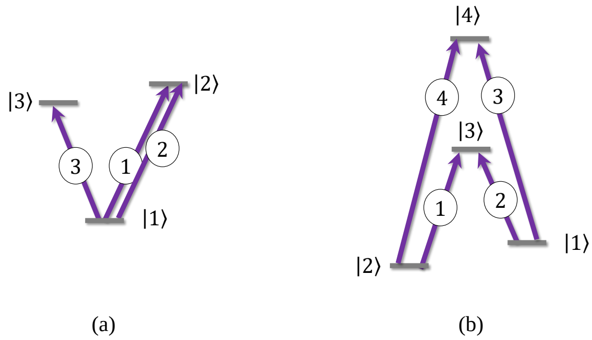

Figure 2.1: The energy level diagram of various multi-level systems forming a closed loop. Here, all the laser driving various transitions are labeled with numbers inside a circle.

2.2.1 When H and L are time-independent

This is a very simple, specific, yet common case encountered in many systems [103, 104, 105]. Before going into more detail, let us explore how to solve this case. If the H and L are time-independent, the matrix M in Eq. 2.6 is also time-independent. In this case, solving the system of coupled differential equations becomes straightforward. In general, the solution can be expressed in terms of the matrix exponential function, given by:

$$\rho = \quad \rho_0 \times \text{expm}(Mt) \tag{2.7}$$

Here ρ_0 is the initial conditions of ρ at $t = 0$. It is important to note that $expm(M) \neq e^M$. There are built-in functions in programming languages to obtain the matrix exponentials numerically. In MATLAB, the inbuilt function is expm(M) [106].

2.2.2 When H or L is time dependent

The Hamiltonian (H) can be a function of time in many cases [77, 107, 108, 109]. For example, H is time-dependent in systems with a closed loop formed by lasers addressing various transitions or in systems where multiple lasers drive the same transition, as shown in Fig. 2.1.

M can also be time-dependent even though H is time independent. Although L is time-independent in most systems, it is possible to have time-dependent L in some specific cases, such as in systems with spontaneously generated coherence [96]. If M is time-dependent and the time-dependence is periodic, we can numerically solve the Eq. 2.6 using the Floquet expansion method. This is applicable when M can be written as follows:

$$M = \sum_{k=-\infty}^{+\infty} M^{(k)} e^{ik\Delta t} \tag{2.8}$$

In general, M contains terms only up to the 2nd or 3rd order, making it a finite sum, and higher orders are neglected depending upon the choice. We write the density matrix elements as:

$$\rho_{ij} = \sum_{m=-\infty}^{+\infty} \rho_{ij}^{(m)} e^{im\Delta t} \tag{2.9}$$

Now using Eq. 2.6, 2.8 and 2.9, we can construct the following equation:

$$\frac{\partial}{\partial t}\begin{bmatrix} . \\ . \\ \rho^{(-2)} \\ \rho^{(-1)} \\ \rho^{(0)} \\ \rho^{(+1)} \\ \rho^{(+2)} \\ . \\ . \end{bmatrix} = M' \cdot \begin{bmatrix} . \\ . \\ \rho^{(-2)} \\ \rho^{(-1)} \\ \rho^{(0)} \\ \rho^{(+1)} \\ \rho^{(+2)} \\ . \\ . \end{bmatrix} \tag{2.10}$$

Here, $\rho^{(m)}$ is a column vector of the form $[\rho_{11}^{(m)}, \rho_{12}^{(m)}, \rho_{13}^{(m)}, ..., \rho_{21}^{(m)}, \rho_{22}^{(m)}, \rho_{23}^{(m)}, ..., \rho_{nn}^{(m)}]^T$ and M' is a supermatrix with the different matrices, $M^{(m)}$ where $M^{(m)}$contains the coefficient of $e^{im\Delta t}$ of every elements of M. M' is given by:

$$M' =$$

$$\begin{bmatrix} . & . & . & . & . & . & . & . & . \\ . & . & . & . & . & . & . & . & . \\ M^{(+2)} & M^{(+1)} & M^{(0)}+2i\Delta & M^{(-1)} & M^{(-2)} & . & . & . & \\ . & M^{(+2)} & M^{(+1)} & M^{(0)}+i\Delta & M^{(-1)} & M^{(-2)} & . & . & . \\ . & . & M^{(+2)} & M^{(+1)} & M^{(0)} & M^{(-1)} & M^{(-2)} & . & . \\ . & . & . & M^{(+2)} & M^{(+1)} & M^{(0)}-i\Delta & M^{(-1)} & M^{(-2)} & . \\ . & . & . & . & M^{(+2)} & M^{(+1)} & M^{(0)}-2i\Delta & M^{(-1)} & M^{(-2)} \\ . & . & . & . & . & . & . & . & . \\ . & . & . & . & . & . & . & . & . \end{bmatrix} \tag{2.11}$$

Again, Eq. 2.39 can be solved by following the same idea as in Eq. 2.6 and 2.7. Once all the coefficients $\rho_{ij}^{(m)}$ are known, $\rho_{ij}(t)$ can be evaluated by using Eq. 2.9. We plan to use the Floquet expansion method when H or L is time-dependent the time-dependence is periodic.

2.3 Constructing the Hamiltonian

So far, we have discussed the procedure to solve the density matrix equation. In this section, we discuss in detail how to write the Hamiltonian of a system. We begin

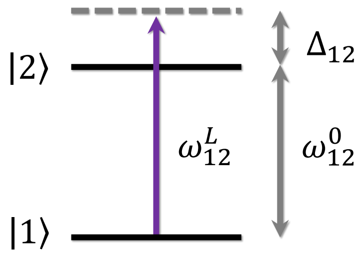

Figure 2.2: The energy level diagram of a two-level system.

this section by considering a two-level system and carefully outline the crucial steps in deriving its Hamiltonian. Following this, we introduce a formalism that simplifies writing the Hamiltonian for complex atomic systems. Through this method, one can avoid the mathematical steps typically involved in obtaining the expression of the Hamiltonian.

2.3.1 Two-level system

A two-level system is the simplest system that exists in atomic physics. Fig. 2.2 shows the energy levels of a two-level system with ground state $|1\rangle$ and excited state $|2\rangle$ with energy $\hbar\omega_1$ and $\hbar\omega_2$ respectively. The separation between the energy level is $\hbar\omega_{12}^0 = \hbar(\omega_2 - \omega_1)$. The system is driven by a monochromatic laser of frequency ω_{12}^L. The detuning of the laser is:

$$\Delta_{12} = \omega_{12}^L - \omega_{12}^0 \tag{2.12}$$

When $\Delta_{12} > 0$ i.e. $\omega_{12}^L > \omega_{12}^0$, the laser is said to be blue-detuned and when $\Delta_{12} < 0$ i.e. $\omega_{12}^L < \omega_{12}^0$, the laser is said to be red-detuned.

The Hamiltonian of the two-level system can be written as:

$$H = H_0 + H_I \tag{2.13}$$

Here, H_0 is the Hamiltonian of the free atom such that $H_0\,|1\rangle = \hbar\omega_1\,|1\rangle$ and $H_0\,|2\rangle = \hbar\omega_2\,|2\rangle$. H_I is the atom-field interaction Hamiltonian, given by:

$$H_I = -\vec{d}.\vec{E} \tag{2.14}$$

Here $\vec{d} = -e\vec{r}$ is the electric dipole moment, and $\vec{E}$ is the electric field of the laser, given by:

$$\vec{E} \quad = \hat{e}E_0 \cos{(\vec{k}.\vec{r} - \omega_{12}^L t)} = \hat{e}\tfrac{1}{2}E_0[e^{i(\vec{k}.\vec{r}-\omega_{12}^L t)} + e^{-i(\vec{k}.\vec{r}-\omega_{12}^L t)}] \tag{2.15}$$

Under dipole approximation, we can neglect the spatial dependence of the field since the wavelength of the laser is much larger than the size of the atom. Thus the Eq. 2.15 can be simplified as:

$$\vec{E} \quad = \hat{e}\tfrac{1}{2}[E_0' e^{i\omega^L_{12}t} + c.c.] \tag{2.16}$$

Here, $E_0' = E_0 e^{-i\vec{k}.\vec{r}}$ and $c.c.$ denotes the complex conjugate. Thus, H_I can be written as:

$$H_I = -1/2 \sum_{i,j} |i\rangle \langle i| \vec{d}.\hat{e}[E_0' e^{i\omega^L_{12}t} + E_0'^* e^{-i\omega^L_{12}t}] |j\rangle \langle j| \tag{2.17}$$

Defining the Rabi frequency, $\Omega_{ij} = -\langle i| \vec{d}.\hat{e}E_0' |j\rangle /\hbar$ and considering $\langle i| \vec{d} |j\rangle = 0$ if states $|i\rangle$ and$|j\rangle$ have same parity $[(-1)^l]$, we can simplify the Eq. 2.17 as:

$$H_I = 1/2(\Omega_{12}e^{i\omega^L_{12}t} + \Omega^*_{12}e^{-i\omega^L_{12}t})(|1\rangle\langle 2| + |2\rangle\langle 1|) \tag{2.18}$$

The wavefunction of the atom, $|\psi(t)\rangle$ can be expressed as a linear superposition of the states $|1\rangle$ and $|2\rangle$, given by:

$$|\psi(t)\rangle = c_1(t)e^{-i\omega_1 t} |1\rangle + c_2(t)e^{-i\omega_2 t} |2\rangle \tag{2.19}$$

where $c_1(t)$ and $c_2(t)$ are complex coefficients satisfying the condition $|c_1(t)|^2 + |c_2(t)|^2 = 1$. The evolution of the system is given by the time-dependent Schrodinger's equation:

$$i\hbar |\dot{\psi}(t)\rangle = H |\psi(t)\rangle \tag{2.20}$$

Using Eq. 2.13 - 2.20, we obtain the following coupled differential equations:

$$\begin{aligned} i\dot{c_1}(t) &= \frac{1}{2}(\Omega_{12}e^{i(\omega^L_{12}-\omega^0_{12})t} + \Omega^*_{12}e^{-i(\omega^L_{12}+\omega^0_{12})t})c_2(t) \\ i\dot{c_2}(t) &= \frac{1}{2}(\Omega_{12}e^{-i(\omega^L_{12}+\omega^0_{12})t} + \Omega^*_{12}e^{i(\omega^L_{12}-\omega^0_{12})t})c_1(t) \end{aligned} \tag{2.21}$$

The rapidly oscillating terms with frequency $(\omega^L_{12} + \omega^0_{12})$ can be neglected under the rotating wave approximation (RWA). Finally using the Eq. 2.12, Eq. 2.21 can be simplified as:

$$\begin{aligned} i\dot{c_1}(t) &= \quad \tfrac{1}{2}\Omega_{12}e^{i\Delta_{12}t}c_2(t) \\ i\dot{c_2}(t) &= \quad \tfrac{1}{2}\Omega^*_{12}e^{-i\Delta_{12}t}c_1(t) \end{aligned} \tag{2.22}$$

It is to be noted that we will reach the same equation of motion (Eq. 2.22) even if we chose the electric field as $\vec{E} = \hat{e}E_0' e^{i\omega^L_{12}t}/2$ instead of Eq. 2.16. This information will simplify the calculation of finding the Hamiltonian of the complex systems.

Thus, the Hamiltonian of the two-level system under RWA can be written as:

$$H = \frac{1}{2}\hbar\Omega_{12}e^{i\Delta_{12}t} |1\rangle \langle 2| + c.c. \tag{2.23}$$

If multiple lasers access the same transitions, the Hamiltonian under RWA (as in Eq. 2.23) can be generalized easily. For example, if there is one additional laser of Rabi frequency Ω'_{12} acting in this same two-level system at detuning Δ'_{12}, the modified Hamiltonian can be written as:

$$H = \frac{1}{2}\hbar(\Omega_{12}e^{i\Delta_{12}t} + \Omega'_{12}e^{i\Delta'_{12}t})\left|1\right\rangle\left\langle 2\right| + c.c. \tag{2.24}$$

We return to the original problem of the two-level system with one laser driving the transition. The Hamiltonian (as in Eq. 2.23) is time-dependent. Using rotating frame approximation (RFA), we can simplify and make the Hamiltonian time independent. The following unitary transformations are used:

$$\begin{aligned} \tilde{c}_1(t) &= \quad c_1(t) \\ \tilde{c}_2(t) &= \; c_2(t)e^{i\Delta_{12}t} \end{aligned} \tag{2.25}$$

Under the RWA and RFA, the final Hamiltonian can be written as:

$$\begin{aligned} H &= -\hbar\Delta_{12}\left|2\right\rangle\left\langle 2\right| + \tfrac{1}{2}\hbar\Omega_{12}\left|1\right\rangle\left\langle 2\right| + c.c. && (2.26) \\ &= \begin{bmatrix} 0 & \frac{1}{2}\hbar\Omega_{12} \\ \frac{1}{2}\hbar\Omega^*_{12} & -\hbar\Delta_{12} \end{bmatrix} && (2.27) \end{aligned}$$

Although the bra-ket form of the Hamiltonian (Eq. 2.26) is a concise way of representing the Hamiltonian, we adopt the matrix form of the Hamiltonian (Eq. 2.27) for the numerical analysis part as it can be directly translated to any programming language. It is to be noted that if multiple lasers are addressing the same transition, then the Hamiltonian can not be made time-independent.

2.3.2 Multi-level simple system

In this section, we discuss how to write the Hamiltonian of a multi-level system directly without going through the calculations as we did for the two-level system in Sec. 2.3.1. First, we consider an atom at rest with having N energy levels with M lasers driving different transitions. We make the following two assumptions:

1. No closed loops are formed by lasers.
2. No two lasers are driving the same transition.

For example, this shortcut technique can be used for writing the H of the atomic system of the type, as shown in Fig. 2.3 (a)-(e). Here, all the laser driving various transitions are labeled with numbers inside a circle.

The atomic system, as shown in Fig. 2.1 (a) and (b), can not be written directly using the same technique as these systems do not follow the assumptions. In Fig. 2.1

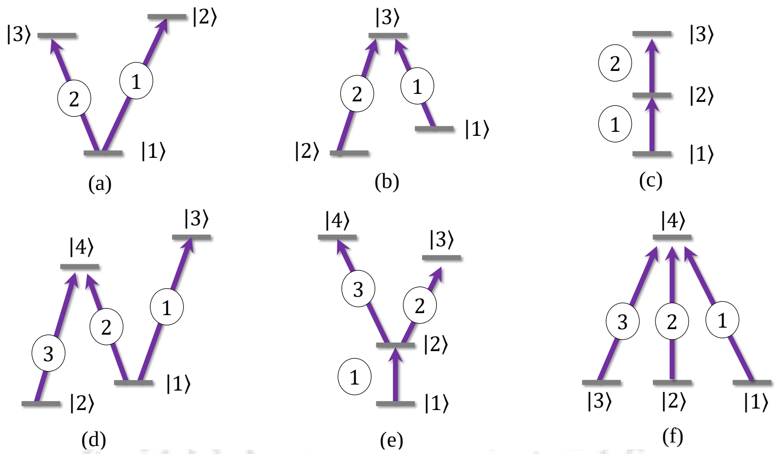

Figure 2.3: The energy level diagram of various multi-level systems.

(a), there are two lasers (1) and (2) addressing the same transitions, which violates assumption (2). Fig. 2.1 (b) is also not allowed because the lasers (1), (2), (3), and (4) have formed a closed loop, which violates assumption (1). We shall discuss the modification required for these kinds of systems in Sec. 2.3.4 and 2.3.5.

Assuming the atomic systems follow the two assumptions, the following steps can be used to write the Hamiltonian :

1. Label the energy levels starting from the ground state. We use the convention of numbering the levels from right to left. Suppose there are N levels.

2. Consider the Rabi frequency and detuning of the lasers driving $|i\rangle \rightarrow |j\rangle$ transition as Ω_{ij} and Δ_{ij}. Note that Ω_{ij} also includes the effect of the Clebsch-Gordan (CG) coefficients. If a laser with Ω_0 is driving $|i\rangle \rightarrow |j\rangle$ transition (with CG coefficient CG_{ij}), then $\Omega_{ij} = \mathrm{CG}_{ij}\Omega_0$.

3. Construct the Hamiltonian, H as $N \times N$ square matrix with all elements as zero.

4. For each laser addressing the $|i\rangle \rightarrow |j\rangle$ transition, update each $H(i,j) = \Omega_{ij}/2$ and $H(j,i) = \Omega^*_{ij}/2$, where $H(i,j)$ denotes the element of the matrix H at i^{th} row and j^{th} column.

5. Update every diagonal element of H as $H(i,i) = \Delta(i)$. The method of writing the $\Delta(i)$ is explained in the next points.

6. Fix $\Delta(i) = 0$ for one specific energy level $|i\rangle$.

7. If a laser is driving $|i\rangle \rightarrow |j\rangle$ and $\Delta(i)$ is known then update $\Delta(j) = \Delta(i) - \Delta_{ij}$. If $\Delta(j)$ is known then update $\Delta(i) = \Delta(j) + \Delta_{ij}$. The signs are very important. Repeat this step until all the diagonal entries are updated.

We now use these steps to write the Hamiltonian of the 3-level V system as shown in Fig. 2.3 (a).

$$H = \begin{bmatrix} 0 & 0 & 0 \\ 0 & 0 & 0 \\ 0 & 0 & 0 \end{bmatrix} \xrightarrow[\text{step (4)}]{\text{after}} \begin{bmatrix} 0 & \Omega_{12}/2 & \Omega_{13}/2 \\ \Omega_{12}^*/2 & 0 & 0 \\ \Omega_{13}^*/2 & 0 & 0 \end{bmatrix} \tag{2.28}$$

$$\xrightarrow[\text{after step (7)}]{\text{fixing } \Delta(1)=0} \begin{bmatrix} 0 & \Omega_{12}/2 & \Omega_{13}/2 \\ \Omega_{12}^*/2 & -\Delta_{12} & 0 \\ \Omega_{13}^*/2 & 0 & -\Delta_{13} \end{bmatrix} \tag{2.29}$$

Similarly, following the same procedure, we can write the Hamiltonian of the 3-level Λ system as:

$$H = \begin{bmatrix} 0 & 0 & \Omega_{13}/2 \\ 0 & -\Delta_{13} + \Delta_{23} & \Omega_{23}/2 \\ \Omega_{13}^*/2 & \Omega_{23}^*/2 & -\Delta_{13} \end{bmatrix} \tag{2.30}$$

2.3.3 Multi-level complex system

We now advance to more complicated systems such as $F = 1 \rightarrow F = 1$, $F = 1 \rightarrow F = 2$, $F = 2 \rightarrow F = 1$, $F = 2 \rightarrow F = 2$, $F = 2 \rightarrow F = 3$, and $F = 3 \rightarrow F = 2$. These systems also follow the same assumptions 2.3.2 made at the beginning of this section. Although all the levels are coupled via decay channels, for writing the H, they can be split into two or more than two subsystems. Then, the Hamiltonian can also be written directly for this system following the same steps (2.3.2).

For example, consider the system $F = 1 \rightarrow F = 1$ as shown in Fig. 2.4 (a), which is a (3+3) level system. All the off-diagonal terms of the H can be written directly. For writing the diagonal terms, it can be split into subsystems (b) and (c). We can fix one $\Delta(i) = 0$ from each subsystem to get all the diagonal terms. Here, we have chosen $\Delta(1) = 0$ and $\Delta(2) = 0$. So the H is given by:

$$H = \begin{bmatrix} 0 & 0 & 0 & 0 & \Omega_{15}/2 & 0 \\ 0 & 0 & 0 & \Omega_{24}/2 & 0 & \Omega_{26}/2 \\ 0 & 0 & -\Delta_{15} + \Delta_{35} & 0 & \Omega_{35}/2 & 0 \\ 0 & \Omega_{24}^*/2 & 0 & -\Delta_{24} & 0 & 0 \\ \Omega_{15}^*/2 & 0 & \Omega_{35}^*/2 & 0 & -\Delta_{15} & 0 \\ 0 & \Omega_{26}^*/2 & 0 & 0 & 0 & -\Delta_{26} \end{bmatrix} \tag{2.31}$$

2.3.4 Multi-level closed loop system

For completeness, we now discuss the procedure of writing the Hamiltonian for a closed-loop system. Remove one laser from the loop so that the H can be written

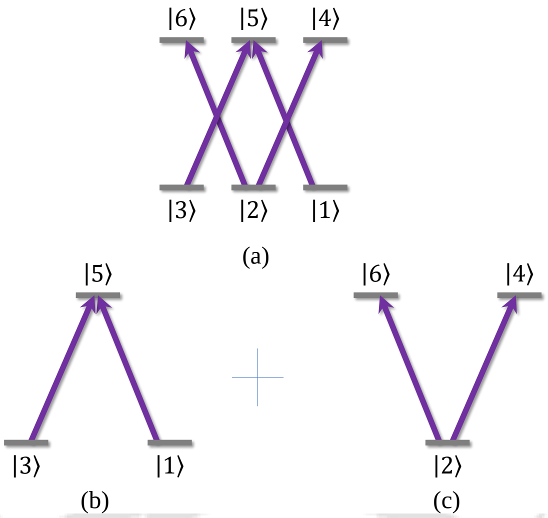

Figure 2.4: The energy level diagram of $F = 1 \rightarrow F = 1$ atomic system

using the above procedure (2.3.2) for the modified system. Suppose a laser driving $|i\rangle \rightarrow |j\rangle$ is removed. First, write the H for the modified system. Then update the $H(i,j) = (1/2)\Omega_{ij}e^{i\Delta t}$ and $H(j,i) = (1/2)\Omega^*_{ij}e^{-i\Delta t}$, where $\Delta = \Delta(j) - \Delta(i) + \Delta_{ij}$.

For example, the Hamiltonian for the 4 level double Λ system (as shown in Fig. 2.1(b)) can be written as:

$$H = \begin{bmatrix} 0 & 0 & \Omega_{13}/2 & (1/2)\Omega_{14}e^{i\Delta t} \\ 0 & -\Delta_{13}+\Delta_{23} & \Omega_{23}/2 & \Omega_{24}/2 \\ \Omega^*_{13}/2 & \Omega^*_{23}/2 & -\Delta_{13} & 0 \\ (1/2)\Omega^*_{14}e^{-i\Delta t} & \Omega^*_{24}/2 & 0 & -\Delta_{13}+\Delta_{23}-\Delta_{24} \end{bmatrix} \tag{2.32}$$

where, $\Delta = -\Delta_{13} + \Delta_{23} - \Delta_{24} + \Delta_{14}$.

2.3.5 Multi-level system with multiple lasers addressing the same transition

Finally, we end this section by discussing the procedure for writing the Hamiltonian when multiple lasers address the same transition. First, modify the system such that only one transition is driven by one laser by removing the additional lasers. Suppose a laser driving $|i\rangle \rightarrow |j\rangle$ with Rabi frequency Ω'_{ij} and detuning $\Delta'_{ij}$is removed. First, write the H for the modified system. Then update $H(i,j)$ by adding one additional quantity $(1/2)\Omega'_{ij}e^{i\Delta t}$ per extra laser. Here, $\Delta = \Delta'_{ij} - \Delta_{ij}$. Also update $H(j,i) = H(i,j)^*$.

For example, the Hamiltonian for the 3 level V system with one additional laser driving $|1\rangle \rightarrow |2\rangle$ (as shown in Fig. 2.1(a)) can be written as:

$$H = \begin{bmatrix} 0 & \Omega_{12}/2 + (1/2)\Omega_{12}^{'} e^{i\Delta t} & \Omega_{13}/2 \\ \Omega_{12}^{*}/2 + (1/2)\Omega_{12}^{*'} e^{-i\Delta t} & -\Delta_{12} & 0 \\ \Omega_{13}^{*}/2 & 0 & -\Delta_{13} \end{bmatrix} \tag{2.33}$$

where, $\Delta = \Delta_{12}^{'} - \Delta_{12}$.

2.3.6 Modification for moving atom

So far, we have considered that the atom is always at rest. For an atom moving with instantaneous speed v in the direction of $\hat{z}$, the following modifications should be made in the Hamiltonian. If the atom interacts with a laser which is addresing $|i\rangle \rightarrow |j\rangle$ and propagating along $+(-)\hat{z}$, every Δ_{ij} should be replaced with $\Delta_{ij} - kv$ $(\Delta_{ij} + kv)$. Accordingly, $\Delta_{ij}t$ in the exponentail terms should be replaced with $\Delta_{ij}t - kz$ $(\Delta_{ij}t + kz)$.

2.3.7 Summary

In this section, we have discussed how to write the Hamiltonian of an atomic system. We have started the section 2.13 with a two-level system and discussed all the crucial steps to derive its Hamiltonian. Then, we have formulated a method for writing the Hamiltonian of any atomic system. Initially, we have considered two assumptions. First, no two lasers are driving the same transition, and second, no loop formation by the driving lasers. We have used the method to write the Hamiltonian of 3 level V and Λ system without going through rigorous calculation. We extend this method to write the Hamiltonian for any complex system such as $F = 1 \rightarrow F = 1$, $F = 1 \rightarrow F = 2$, $F = 2 \rightarrow F = 1$, $F = 2 \rightarrow F = 2$, $F = 2 \rightarrow F = 3$, $F = 3 \rightarrow F = 2$. Additionally, we have also discussed how to write the Hamiltonian in case the assumptions we have made do not hold. We have discussed two examples: a four-level double lambda system and a three-level system with two lasers driving the same transitions. Finally, we have concluded this section with the technique of how to write the Hamiltonian for a moving atom. The above formalism allows us to write the Hamiltonian of moving atoms of any system without going through calculations, which helps us save time and effort. In the following sections, we shall use this formalism to write the Hamiltonian of the different systems.

2.4 Constructing the Lindbladian

In the absence of a driving electromagnetic field, the Hamiltonian of the system is zero. This implies that an atom if prepared in a superposition state, will remain in the same state if we do not consider the effect of the environment. However, in reality, an atom in an excited state always relaxes to a lower energy state via spontaneous emission of photons. This is due to the excitation by the different modes of the vacuum electric field [110].

The effect of spontaneous decay can be incorporated phenomenologically. If the population is decaying from $|i\rangle \rightarrow |j\rangle$ with decay rate Γ_{ij}, then the rate of decrease in population of the state $|i\rangle$ is proportional to the population in the state $|i\rangle$ with proportionality constant, Γ_{ij}. This is the same rate at which the population of state $|j\rangle$ will increase due to conservation of population. The time evolution of the density matrix due to spontaneous decay can be given by,

$$\dot{\rho}_{ii} = -\Gamma_{ij}\rho_{ii} \tag{2.34}$$

$$\dot{\rho}_{jj} = +\Gamma_{ij}\rho_{ii} \tag{2.35}$$

$$\dot{\rho}_{ij} = -(1/2)(\Gamma_i + \Gamma_j)\rho_{ij} \tag{2.36}$$

where Γ_i and Γ_j are total decay rate of states $|i\rangle$ and $|j\rangle$ respectively.

We use this formalism to write the decay part of the density matrix equation for the generalized atomic system below.

2.4.1 Two level system

We start with a two-level system with ground state, $|1\rangle$, and excited state, $|2\rangle$. Suppose the decay rate of $|2\rangle$ is Γ_{21}. So the equations can be written as:

$$\begin{aligned}
\dot{\rho}_{11} &= +\Gamma_{21}\rho_{22} \\
\dot{\rho}_{12} &= -(1/2)\Gamma_{21}\rho_{12} \\
\dot{\rho}_{21} &= -(1/2)\Gamma_{21}\rho_{21} \\
\dot{\rho}_{22} &= -\Gamma_{21}\rho_{22}
\end{aligned} \tag{2.37}$$

These equations can be written in the matrix form as follows:

$$\begin{bmatrix} \dot{\rho}_{11} & \dot{\rho}_{12} \\ \dot{\rho}_{21} & \dot{\rho}_{22} \end{bmatrix} = \begin{bmatrix} +\Gamma_{21}\rho_{22} & -(1/2)\Gamma_{21}\rho_{12} \\ -(1/2)\Gamma_{21}\rho_{21} & -\Gamma_{21}\rho_{22} \end{bmatrix} = K \tag{2.38}$$

We define the RHS of the Eq. 2.38 as the decay matrix, K. Our formalism of solving the master equation given in Eq. 2.6 demands our equations to be reshaped in the following specific form: $\dot{\rho} = L\rho$.

$$\begin{bmatrix} \dot{\rho}_{11} \\ \dot{\rho}_{12} \\ \dot{\rho}_{21} \\ \dot{\rho}_{22} \end{bmatrix} = \begin{bmatrix} 0 & 0 & 0 & \Gamma_{21} \\ 0 & -\Gamma_{21}/2 & 0 & 0 \\ 0 & 0 & -\Gamma_{21}/2 & 0 \\ 0 & 0 & 0 & -\Gamma_{21} \end{bmatrix} \cdot \begin{bmatrix} \rho_{11} \\ \rho_{12} \\ \rho_{21} \\ \rho_{22} \end{bmatrix} \tag{2.39}$$

Here, $L\rho$ is the Lindbladian of the system. The exact mathematical expression of the Lindbladian is given in Sec. 2.4.3. For the two-level system, the decay matrix K is a square matrix of dimension 2×2, and L is a square matrix of dimension 4×4.

2.4.2 Multi-level system

In this section, we discuss the procedure of constructing the decay matrix in the form L of the size $N^2 \times N^2$ for a general N-level system.

1. Create a square matrix Γ of size $N \times N$ with all elements as zero.
2. Update the decay rates in Γ such that $\Gamma(j,i) = \Gamma_{ij}$. Here, Γ_{ij} is decay rate from $|i\rangle \to |j\rangle$.
3. Update the diagonal entries of Γ such that $\Gamma(i,i) = -\Gamma_i^T$. Here, Γ_i^T is the total decay rate of state $|i\rangle$.
4. Create the square matrix L of the size $N^2 \times N^2$ with all elements as zero.
5. Update all the entries of L using $L(N\times(i-1)+j, N\times(i-1)+j) = -(1/2)(\Gamma_i^T + \Gamma_j^T)$. This incorporates the effect of decay of the coherences between states $|i\rangle$ and $|j\rangle$.
6. Finally update all the entries L using $L(N\times(i-1)+i, N\times(j-1)+j) = \Gamma(i,j)$. This incorporates the effect of population transfer from $|j\rangle \to |i\rangle$.
7. Additionally, in case we need to incorporate the effect of ρ_{mn} artificially on the ρ_{ij}, then update L using $L(N\times(i-1)+j, N\times(m-1)+n) =$CE and $L(N\times(j-1)+i, N\times(n-1)+m) =$CE*. Here, CE the coefficient such that $\dot{\rho}_{ij} = \text{CE}\ \rho_{mn}$.

We use the above procedure to find the L of the two-level system.

$$\Gamma = \begin{bmatrix} 0 & 0 \\ 0 & 0 \end{bmatrix} \xrightarrow[\text{step (2)}]{\text{after}} \begin{bmatrix} 0 & \Gamma_{21} \\ 0 & 0 \end{bmatrix} \xrightarrow[\text{step (3)}]{\text{after}} \begin{bmatrix} 0 & \Gamma_{21} \\ 0 & -\Gamma_{21} \end{bmatrix} \tag{2.40}$$

$$L = \begin{bmatrix} 0 & 0 & 0 & 0 \\ 0 & 0 & 0 & 0 \\ 0 & 0 & 0 & 0 \\ 0 & 0 & 0 & 0 \end{bmatrix} \xrightarrow[\text{step (5)}]{\text{after}} \begin{bmatrix} 0 & 0 & 0 & 0 \\ 0 & -\Gamma_{21}/2 & 0 & 0 \\ 0 & 0 & -\Gamma_{21}/2 & 0 \\ 0 & 0 & 0 & -\Gamma_{21} \end{bmatrix} \tag{2.41}$$

$$\xrightarrow[\text{step (6)}]{\text{after}} \begin{bmatrix} 0 & 0 & 0 & \Gamma_{21} \\ 0 & -\Gamma_{21}/2 & 0 & 0 \\ 0 & 0 & -\Gamma_{21}/2 & 0 \\ 0 & 0 & 0 & -\Gamma_{21} \end{bmatrix} \tag{2.42}$$

This is an effective way to write the decay matrix of any multi-level system and applies to most of the systems as long as the effect of spontaneously generated coherence (SGC) is negligible. In the next section, we discuss SGC and how to incorporate its effect.

2.4.3 Spontaneously generated coherence (SGC)

In general, atomic coherence can be created by coherent electromagnetic fields such as laser fields and microwave fields. It can also be generated by an incoherent field via spontaneous emission [91, 110, 111]. Spontaneous decay occurs because of the excitation by the different modes of vacuum electric field. In general, spontaneous decay is responsible for destroying the atomic coherence. However, interesting phenomena can occur when a vacuum mode drives two transitions simultaneously to generate an unconventional atomic coherence [112]. This is known as spontaneously generated coherence (SGC). Because this coherence is induced by the vacuum fields, it is also called vacuum-induced coherence (VIC).

SGC is a very interesting and important phenomenon and has been the subject of extensive investigation within multi-level atomic systems [92, 93, 94, 95, 96, 97, 98, 99]. SGC requires two or more near-degenerate energy levels and non-orthogonal electric-dipole matrix elements of the two or more spontaneous decay channels (when the atom is placed in free space) [98, 111, 113]. For non-degenerate energy levels, the effect of SGC is averaged out [92]. SGC can also be generated for orthogonal dipole moments but in an anisotropic vacuum, [114]. We restrict our discussion to an isotropic vacuum in this thesis.

SGC holds a crucial role in the field of spectroscopy, and it can change the steady state response of the medium. When the same vacuum mode drives two transitions simultaneously, then it can create SGC between the ground states due to the decay of the population [100]. Furthermore, when the same vacuum mode drives two transitions simultaneously, coherence between the excited states transfers to the ground states, resulting in SGC between the ground states [96]. In a Ladder system, SGC can also be created if the energy levels are nearly spaced [115]. However, a Ladder system with equally spaced energy levels is not feasible in an atomic system.

The atomic spectrum profile and the laser cooling are related to each other. Since SGC affects the spectrum profile, it becomes apparent that SGC is also a significant factor in laser cooling processes. That is why we need to incorporate the effect of SGC in our density matrix equation. SGC is particularly sensitive to magnetic fields, as it occurs when the energy difference between the excited and ground states is nearly equal. In the absence of magnetic fields, the degeneracy of Zeeman levels allows for effective SGC and, consequently, efficient PGC. Conversely, in the presence of a magnetic field, the degeneracy of the Zeeman levels is lifted, averaging out the effect of SGC and making PGC fragile to magnetic fields.

In this section, we construct the formalism to incorporate the effect of SGC on any atomic system. Suppose there are N levels with M different decay channels. The Lindbladian can be written as follows [91, 102]:

$$L = (1/2) \times \sum_{i,j=1}^{M} \gamma_{ij}[-S_i^+ S_j^- \rho + 2S_j^- \rho S_i^+ - \rho S_i^+ S_j^-] e^{i(w_i - w_j)t} \tag{2.43}$$

Here,

$$\omega_i = \omega_{nm} \text{ where } (n > m) \tag{2.44}$$

$$S_i^+ = A_{nm} = |n\rangle \langle m| \tag{2.45}$$

$$S_i^- = A_{mn} = |m\rangle \langle n| \tag{2.46}$$

$$\gamma_{ij} = \sqrt{\gamma_i \gamma_j} \cos(\theta_i - \theta_j) \tag{2.47}$$

It is to be noted that the sum is over the number of transitions, not on the number of energy levels. The allowed decay transitions are $|m\rangle \to |n\rangle$. $(\theta_i - \theta_j)$ denotes the relative angle between the two dipole moment vectors, $\vec{\mu}_i$ and $\vec{\mu}_j$. If $\vec{\mu}_i$ and $\vec{\mu}_j$ are perpendicular, then $\gamma_{ij} = 0$. If $\vec{\mu}_i$ and $\vec{\mu}_j$ are parallel, then γ_{ij} is maximum, and $\gamma_{ij} = \sqrt{\gamma_i \gamma_j}$. This indicates that decay channels corresponding to σ_+, σ_- and π transitions can not result in SGC with each other.

Let us now write the Lindbladian for the 3-level Λ system (as shown in Fig. 2.3 (b)) and understand the effect of SGC. Suppose the difference in energy level between the ground states $|1\rangle$ and $|2\rangle$ is $\hbar\delta$. Here, the allowed decay transitions are $|3\rangle \to |1\rangle$ and $|3\rangle \to |2\rangle$. Suppose the decay rates are Γ_{31} and Γ_{21} respectively. So, the allowed values of S_i^- are $|3\rangle\langle 1|$ and $|3\rangle\langle 2|$. The Linbladian can be written in the K matrix form as:

$$K = \begin{bmatrix} \Gamma_{31}\rho_{33} & \sqrt{\Gamma_{31}\Gamma_{32}} e^{i\delta t}\rho_{33} & -(\Gamma_{31}+\Gamma_{32})\rho_{13}/2 \\ \sqrt{\Gamma_{31}\Gamma_{32}} e^{-i\delta t}\rho_{33} & \Gamma_{32}\rho_{33} & -(\Gamma_{31}+\Gamma_{32})\rho_{23}/2 \\ -(\Gamma_{31}+\Gamma_{32})\rho_{31}/2 & -(\Gamma_{31}+\Gamma_{32})\rho_{32}/2 & -(\Gamma_{31}+\Gamma_{32})\rho_{33} \end{bmatrix} \tag{2.48}$$

It is to be noted that the effect of SGC is directly affecting the coherence between the ground states $|1\rangle$ and $|2\rangle$ and is proportional to the population of the excited state. If δ is large as compared to the linewidth of the transition or detuning of the laser, then the effect of rapidly oscillating term $e^{i\delta t}$ is averaged out to zero. Also, if the dipole moments are orthogonal, then the terms arising from the cross-correlation will become zero.

Thus, in the absence of SGC, the decay matrix reduces to the following, which can also be written directly using the procedure mentioned in Sec. 2.3.2:

$$K_{SGC}^{w.o.} = \begin{bmatrix} \Gamma_{31}\rho_{33} & 0 & -(\Gamma_{31}+\Gamma_{32})\rho_{13}/2 \\ 0 & \Gamma_{32}\rho_{33} & -(\Gamma_{31}+\Gamma_{32})\rho_{23}/2 \\ -(\Gamma_{31}+\Gamma_{32})\rho_{31}/2 & -(\Gamma_{31}+\Gamma_{32})\rho_{32}/2 & -(\Gamma_{31}+\Gamma_{32})\rho_{33} \end{bmatrix} \tag{2.49}$$

SGC plays a significant role in sub-Doppler cooling. The sub-Doppler cooling with a red-detuned laser can only be explained using SGC. Without SGC, it may give heating. In the absence of SGC, the sub-Doppler temperature in MOT may be achieved using the blue-detuned laser. This will be studied in detail in the final chapter of this thesis.

2.4.4 Summary

In this section, we have discussed how to write the decay matrix of any atomic system. We have started with the 2-level system and constructed the decay matrix using the phenomenological approach. When solving the master equation, the decay matrix needs to be reshaped to a different form. We have developed a procedure for writing the Lindbladian of any level system, which can be incorporated directly into a programming language. Then, we have discussed the spontaneously generated coherence, which is a very important phenomenon in sub-Doppler cooling and blue-detuned cooling. We have also discussed how to construct the Lindbladian to study the effect of SGC.

2.5 Absorption from density matrix elements

So far, we have discussed how to construct the Hamiltonian and decay matrix of any atomic system. We have also discussed how to solve the density matrix equations. Thus we can find how the density matrix elements vary with different parameters such as time, detuning, velocity of the atom, and power of the laser. In this section, we derive the relationship of the density matrix elements to the absorption of the lasers by the atoms. In general, the absorption is proportional to the imaginary part of the corresponding off-diagonal density matrix elements. The exact formula is derived below.

2.5.1 Wave propagation equation

The propagation of light through a medium can be described by the Maxwell's equation, given by:

$$\begin{aligned}
\nabla \cdot \vec{D} &= \rho_f, && \text{(Gauss Law)} \\
\nabla \cdot \vec{B} &= 0, && \text{(Gilbert's Law)} \\
\nabla \times \vec{E} &= -\tfrac{\partial \vec{B}}{\partial t}, && \text{(Faradey's Law)} \\
\nabla \times \vec{H} &= \vec{J}_f + \tfrac{\partial \vec{D}}{\partial t}, && \text{(Ampere's Law)} \qquad (2.50)
\end{aligned}$$

In the above equations, $\vec{E}$ and $\vec{B}$ are the electric field and magnetic field at any point ($\vec{r}$) at any time (t), respectively, ρ_f and $\vec{J}_f$ are the free charge density and free current density in the medium at the same point in the space-time. The electric displacement ($\vec{D}$) and magnetic field intensity ($\vec{H}$) are given by:

$$\begin{aligned}
\vec{D} &= \epsilon_0 \vec{E} + \vec{P} \\
\vec{B} &= \mu_0 \vec{H} + \vec{M} \qquad (2.51)
\end{aligned}$$

Here, $\vec{P}$ and $\vec{M}$ are the polarization and magnetization of the medium. In the atomic medium, which is a nonmagnetic and non-conducting medium with no free charge and no free current, the above equations 2.50 and 2.51 simplify to the following:

$$\nabla \cdot \vec{D} = 0, \tag{2.52}$$

$$\nabla \cdot \vec{B} = 0, \tag{2.53}$$

$$\nabla \times \vec{E} = -\frac{\partial \vec{B}}{\partial t}, \tag{2.54}$$

$$\nabla \times \vec{H} = \frac{\partial \vec{D}}{\partial t}, \tag{2.55}$$

and

$$\vec{D} = \epsilon_0 \vec{E} + \vec{P} \tag{2.56}$$

$$\vec{B} = \mu_0 \vec{H} \tag{2.57}$$

Taking curl on both sides of Eq. 2.54, using Eq. 2.56 and 2.57 along with the fact that for a homogeneous and isotropic medium $\nabla \cdot \vec{E} = 0$:

$$\nabla^2 \vec{E} - \frac{1}{c^2}\frac{\partial^2 \vec{E}}{\partial t^2} = \mu_0 \frac{\partial^2 \vec{P}}{\partial t^2} \tag{2.58}$$

The Eq. 2.58 is Maxwell's equation for propagation of EM field through a dielectric medium. This is a second-order inhomogeneous wave equation, which is difficult to solve analytically. Under certain approximations discussed below, this equation can be solved numerically.

Let us consider a quasi-monochromatic wave with frequency (ω) propagating inside a medium along $\hat{z}$ direction with wave vector $\vec{k}$ and polarization along $\hat{e}$. The electric field and polarization can be written as:

$$\begin{aligned} \vec{E}(x,y,z,t) &= \hat{e}E(x,y,z,t)e^{i(kz-\omega t)} + c.c. \\ \vec{P}(x,y,z,t) &= \hat{e}P(x,y,z,t)e^{i(kz-\omega t)} + c.c. \end{aligned} \tag{2.59}$$

Here, c.c. is the complex conjugate. Under the slowly varying envelope approximation (SVEA), neglecting the higher order time and space derivative and the transverse variation, the Eq. 2.58 for a continuous wave reduces to the following:

$$\frac{\partial E}{\partial z} = \frac{i\mu_0\omega^2}{2k}P \tag{2.60}$$

Using $P = \epsilon_0 \chi E$ where χ is the succeptibilty of the medium ($\chi = \chi_R + i\chi_I$), the solution of the Eq. 2.60 becomes:

$$\begin{aligned} E &= E_0 e^{ik\chi z/2} \\ &= E_0 e^{-k\chi_I z/2} e^{ik\chi_R z/2} \end{aligned} \tag{2.61}$$

Now, defining the medium opacity α as follows:

$$\alpha = k\chi_I \tag{2.62}$$

The final transmitted electric field of the EM field after propagating a distance L is given by:

$$E(L,t) = \quad E_0 e^{-k\chi_I z/2} e^{ik\chi_R z/2} e^{i(kz-\omega t)} + c.c. \tag{2.63}$$

Considering I_0 is the intensity of the incident EM field, the final transmitted intensity of the EM field after propagating a distance L is given by:

$$I = I_0 e^{-\alpha L} \tag{2.64}$$

The absorption of the laser by the medium thus can be written as:

$$\begin{aligned} A &= -\ln\left(\tfrac{I}{I_0}\right) \\ &= \alpha L \\ &= k\chi_I L \\ &= kL\ \mathrm{Im}(\chi) \end{aligned} \tag{2.65}$$

where, Im(.) denotes the imaginary part of the quantity.

2.5.2 Relationship: Absorption and density matrix

When a laser beam of frequency ω_L propagates through a medium, it induces dipole moments $\vec{d}$ on the atoms. Suppose the atomic medium consists of two-level atoms with the number density n_0. Consider the dipole matrix elements d_{12} and d_{21} are real. The induced polarization can be written as:

$$\begin{aligned} P &= n_0\langle d\rangle \\ &= n_0 \times \mathrm{Trace}(\rho d) \\ &= n_0(d_{12}\rho_{21} + d_{21}\rho_{12}) \\ &= n_0|d_{12}|(\rho_{12} + \rho_{21}) \\ &= n_0|d_{12}|(\tilde{c}_2\tilde{c}_1^* e^{-i\omega_L t} + \tilde{c}_1\tilde{c}_2^* e^{i\omega_L t}) \\ &= \tfrac{n_0|d_{12}|}{E_0}\tilde{c}_2\tilde{c}_1^* E_0 e^{-i\omega_L t} + c.c. \\ &= \tfrac{n_0|d_{12}|}{E_0}\tilde{\rho}_{21} E + c.c. \\ &= \tfrac{n_0|d_{12}|^2}{\hbar\Omega_{12}}\tilde{\rho}_{21} E + c.c. \end{aligned} \tag{2.66}$$

Comparing the above equation with $\vec{P} = \epsilon_0\chi\vec{E}$, the susceptibility of an atomic medium can be written as:

$$\chi \quad = \frac{n_0|d_{12}|^2}{\epsilon_0\hbar\Omega_{12}}\tilde{\rho}_{21} \tag{2.67}$$

Using the Eq. 2.62 and 2.66 the absorption by an atomic medium is given by:

$$A \quad = \frac{n_0 L}{\epsilon_0 c\hbar}\frac{\omega|d_{12}|^2}{\Omega_{12}}\mathrm{Im}(\tilde{\rho}_{21}) \tag{2.68}$$

This is a very important formula in the field of atomic physics, as most of the parameters are related to the absorption of the laser by the atomic medium. Since dipole matrix elements are proportional to the CG co-efficient and Rabi frequency is also proportional to the dipole matrix elements, the absorption can be related to the CG coefficient as:

$$A \quad \propto \mathrm{CG}_{12} \times \mathrm{Im}(\tilde{\rho}_{21}) \tag{2.69}$$

2.6 Relationship: Force and density matrix

Building on our earlier discussion about the relationship between the density matrix elements and absorption, we now shift our focus to understanding how the force experienced by an atom relates to the density matrix elements.

In simpler terms, the force on an atom is due to the momentum exchange between the atom and light during absorption and spontaneous emission. When an atom absorbs a photon carrying momentum $\hbar\vec{k}$, it undergoes a momentum kick equivalent to $\hbar\vec{k}$ and gets excited to a higher energy state. Subsequently, when the atom relaxes to the ground state through spontaneous emission, it emits a photon in a random direction. Notably, the average change in the momentum of the atom in this emission process amounts to zero.

As a consequence, the atom encounters an average force from the light from the absorption and spontaneous emission cycle. This force is anticipated to be directly proportional to the momentum kick imparted by the laser, denoted as $\hbar\vec{k}$. Additionally, it should exhibit proportionality to the rate of absorption, implying a correlation with the imaginary part of the off-diagonal density matrix elements.

In the next section, we derive the exact formula of the force.

2.6.1 Two level system

Consider an atom moving along $\hat{z}$ direction interacts with a traveling wave with an electric field given by:

$$\vec{E} = (1/2)\vec{E}_0 e^{i(kz-wt)} + c.c. \tag{2.70}$$

Considering $\hbar\Omega_0 = \vec{d}.\vec{E}_0$, the interaction Hamiltonian can be written as:

$$H_I = (1/2)\hbar\Omega_0 e^{i(kz-\omega t)} \left|1\right\rangle \left\langle 2\right| + c.c. \tag{2.71}$$

Now, the force experienced by an atom can be written as:

$$\begin{aligned}\vec{F} =& \quad \mathrm{Re}\big(-\langle\nabla H_I\rangle\big)\\ =& \quad \mathrm{Re}\big(-1/2ik\hbar\Omega_0\tilde{\rho}_{21}+c.c.\big)\\ =& \quad \hbar\vec{k}\Omega_0\mathrm{Im}\big(\tilde{\rho}_{12}\big)\end{aligned} \tag{2.72}$$

Here, Re(.) and Im(.) denote the real and imaginary parts. This force expression can be written in many different forms such as in terms of ρ_{22} or ρ_{11} [6]. We stick to the above formalism as it helps to write the force for a complicated level system. In the next section, we shall discuss how to generalize this formulation to write the force on a multi-level system. Physically, we can consider this force as the momentum kick received from the laser during each absorption cycle times the average rate (γ_p) at which the atom is absorbing the photon. Thus γ_p can be written as:

$$\gamma_p = \Omega_0\mathrm{Im}\big(\tilde{\rho}_{12}\big) \tag{2.73}$$

2.6.2 Generalization: Multi-level system

Suppose we want to write down the force for a multi-level N-system in the presence of M lasers. Consider one transition is driven by only one laser. Suppose the laser i with wavevector $\vec{k}_i$ with Rabi frequency Ω_i is driving the $|j\rangle$ to $|k\rangle$ transition. Then, the force experienced by the atom can be generalized as:

$$\vec{F} = \sum_{i=1}^{M}\hbar\vec{k}_i\Omega_i\mathrm{Im}\big(\tilde{\rho}_i\big) \tag{2.74}$$

Here $\tilde{\rho}_i = \tilde{\rho}_{jk}$.

2.6.3 Example: 3 level V system

For example, let us consider an atom moving along $\hat{z}$ direction. Assume the atomic system as a 3-level V system as shown in Fig. 2.3(a). Suppose $|2\rangle$ and $|3\rangle$ are degenerate. Both the lasers (L_1 and L_2) are of same frequency (ω_L) and Rabi frequency (Ω_0) with wavevectors $+\hbar k\hat{z}$ and $-\hbar k\hat{z}$ respectively. So, the force experienced by the atom can be written as:

$$\vec{F} = \hat{z}\hbar k\Omega_0\mathrm{Im}\big(\tilde{\rho}_{12}-\tilde{\rho}_{13}\big) \tag{2.75}$$

2.6.4 Example: 3 level Λ system

Consider an atomic system as a 3-level Λ system as shown in Fig. 2.3(b). Suppose the ground states, $|1\rangle$ and $|3\rangle$ are degenerate. Both the lasers (L_1 and L_2) are of same frequency (ω_L) and Rabi frequency (Ω_0) with wavevectors $+\hbar k\hat{z}$ and $-\hbar k\hat{z}$ respectively. So, the force experienced by the atom can be written as:

$$\vec{F} = \hat{z}\hbar k\Omega_0 \mathrm{Im}\big(\tilde{\rho}_{13} - \tilde{\rho}_{23}\big) \tag{2.76}$$

2.6.5 Example: (3+3) level system

Consider the atomic system $F = 1 \rightarrow F = 1$, which is a (3+3) level system as shown in Fig. 2.3(b). Suppose the ground states, $|1\rangle$, $|2\rangle$ and $|3\rangle$ are degenerate and the excited states, $|4\rangle$, $|5\rangle$ and $|6\rangle$ are degenerate. Let the lasers (L_1 and L_2) are of same frequency (ω_L) and Rabi frequency (Ω_0) with wavevectors $+\hbar k\hat{z}$ and $-\hbar k\hat{z}$ respectively. Let L_1 (L_2) drives the $|2\rangle \rightarrow |4\rangle$ and $|3\rangle \rightarrow |5\rangle$ ($|1\rangle \rightarrow |5\rangle$ and $|2\rangle \rightarrow |6\rangle$) transitions. So, the force experienced by the atom can be written as:

$$\vec{F} = \hat{z}\hbar k\Omega_0 \mathrm{Im}\big(\tilde{\rho}_{24} + \tilde{\rho}_{35} - \tilde{\rho}_{15} - \tilde{\rho}_{26}\big) \tag{2.77}$$

If the Ω of the different transitions are different (ex. $\Omega_{ij} = \mathrm{CG}_{ij}\Omega_0$), then the force can be written as:

$$\vec{F} = \hat{z}\hbar k\Omega_0 \mathrm{Im}\big(\mathrm{CG}_{24}\tilde{\rho}_{24} + \mathrm{CG}_{35}\tilde{\rho}_{35} - \mathrm{CG}_{15}\tilde{\rho}_{15} - \mathrm{CG}_{26}\tilde{\rho}_{26}\big) \tag{2.78}$$

2.7 Laser Cooling

So far, we have discussed that a laser beam can exert force on an atom. When a moving atom experiences a force from the opposite direction, its momentum decreases. This means its speed decreases, and the atom slows down. The RMS speed of an atom (v) of mass (m) is related to the temperature (T) as per the relation given below [6]:

$$\frac{1}{2}mv^2 = \frac{1}{2}k_\mathrm{B}T \tag{2.79}$$

Here k_B is the Boltzmann constant. When the speed decreases, we say that the temperature decreases and cooling occurs.

When an atom moving with speed v encounters a laser beam of frequency ω_L, the frequency observed by the atom (ω_L') is modified as per the Doppler effect, given by:

$$\omega_L' = \omega_L \pm kv \tag{2.80}$$

When the atom is moving in the same (opposite) direction of the laser beam, the sign is positive (negative). Here $k = \omega_L/c$.

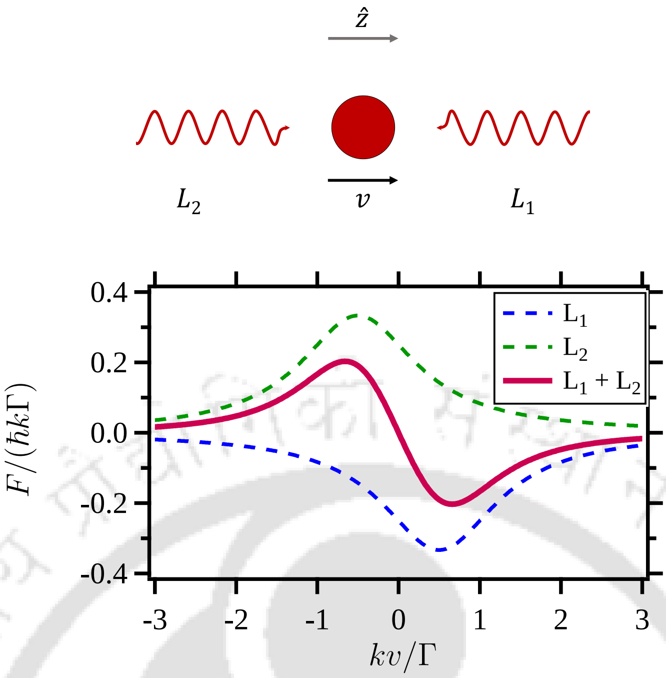

Figure 2.5: Force vs. velocity in a two-level system. The red line represents the net force on the atom. The blue (green) dashed line represents the force from the L_1 (L_2) laser. Parameters used: $\Gamma = 2\pi \times 6$ MHz, $\Omega = \Gamma$, $\Delta_{12} = -\Gamma/2$, $\lambda = 780$ nm.

Consider now an ideal case of a monochromatic laser of frequency ω_L interacting with a two-level system. For an atom at rest, the probability that the atom absorbs a photon from the laser is maximum if the laser is resonant. If the atom is moving along the $+\hat{z}$ direction and the detuning of the laser is zero, as a result of the Doppler shift, the frequency of the laser observed by the atom is changed and the probability of absorption decreases. If a red-detuned laser is propagating towards the atom, when the frequency observed by the atom approaches resonance, the probability of absorption increases and the atom slows down. This is the principle of Doppler cooling.

Let us find the force experienced by an atom that is moving with speed v along the $+\hat{z}$ direction in the presence of two counterpropagating lasers L_1 and L_2 with wavevectors along the $-\hat{z}$ and $+\hat{z}$ directions respectively. The schematic diagram of the system is shown in Fig. 2.5, and the force experienced by the atom is shown below. Let the Rabi frequency and the detuning of the lasers be Ω and Δ_{12} respectively. Let both the lasers be red-detuned (i.e., $\Delta_{12} < 0$).

The force exerted by the laser L_1 on the atom is shown as a blue dashed line. The force is of Lorentzian behavior and is in a negative direction. Similarly, the force exerted by the laser L_2 on the atom is shown as a green dashed line. This is also Lorentzian behavior, but it is acting in a positive direction. The net force by the two lasers is shown as a red line. From the figure, we can see that the force is negative for the positive velocity of atoms. This means if an atom is moving towards the $\hat{z}$

direction, it will experience a drag force along the $-\hat{z}$ direction, and its speed will decrease. Similar behavior is observed for the atom moving in a negative direction. If the atom is moving towards the $-\hat{z}$ direction, it will experience a drag force along the $+\hat{z}$ direction, and its speed will decrease. This principle of laser cooling is known as Doppler cooling.

When the lasers are made blue-detuned, the nature of the graph is reversed. This means that an atom moving along the $+(-)\hat{z}$ direction will experience a force along the $+(-)\hat{z}$ direction and its speed will increase. This is called Doppler heating.

The above concept of Doppler cooling can be extended from 1 Dimension to 3 Dimensions by applying two more pairs of counterpropagating lasers from the other two perpendicular directions. This configuration is referred to as optical molasses (OM).

2.7.1 Limit of Doppler cooling

The nature of the force for small velocity can be given by $\vec{F} = -\beta\vec{v}$. Here, β can also be thought of as the slope of F vs. v curve at $v = 0$. If we solve this equation, we get $v = v_0 e^{-\beta t/m}$. This means that after a very long time, v should become zero, which means the velocity distribution function becomes a delta function with width zero. This indicates that the temperature of the atom should become zero, which violates Heisenberg's uncertainty principle.

This artifact appears because we ignored the heating effect because of the momentum kick on the atom due to the spontaneous emission of photons. Although the average change in momentum ($\langle\Delta p\rangle$) during the spontaneous emission cycle is zero, the variance in momentum is non-zero, i.e. $\langle\Delta p^2\rangle \neq 0$. The atom performs a random walk in momentum space during each absorption and spontaneous emission cycle, which results in diffusion in momentum space with diffusion coefficient D_0, which is given by:

$$2D_0 = 2\Delta p^2/\Delta t = 2 \times (\hbar k)^2 \times 2 \times \gamma_p \tag{2.81}$$

Here, the first factor, 2, appears because the atom receives the random momentum kick in both absorption and emission cycles. The second factor $(\hbar k)^2$ is the variance in momentum due to each momentum kick. The third factor (2) is due to the presence of two lasers from which atoms can get the momentum kick. Finally, the last factor (γ_p) is the rate at which it gets a momentum kick. Using the Eq. 2.73, for the 2-level atom, the Eq. 2.81 can be modified as:

$$2D_0 = 4(\hbar k)^2\Omega_{12}\mathrm{Im}(\tilde{\rho}_{12}) \tag{2.82}$$

Now, using the theory of Brownian motion, the steady state temperature can be written as [6]:

$$T = D_0/\beta \tag{2.83}$$

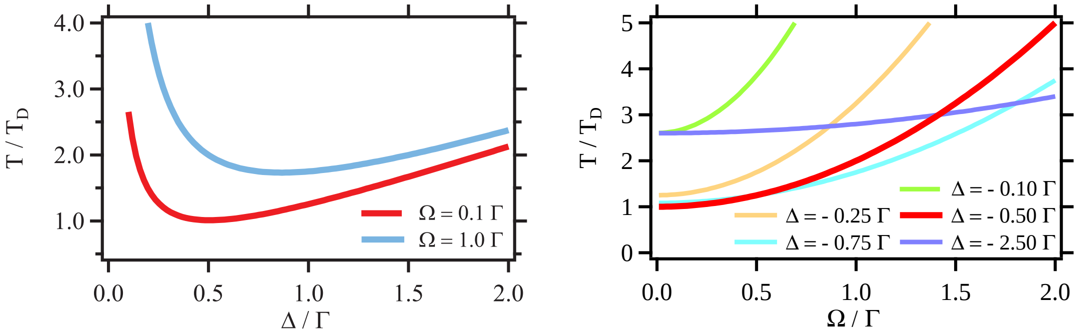

(a) (b)

Figure 2.6: Temperature vs. (a) detuning (magnitude) and (b) Rabi frequency of the lasers in a two-level system at different (a) Rabi frequencies and (b) detunings respectively.

For the two-level system, we use the above formalism and plot the normalized temperature (T/T_{D}) with the magnitude of the detuning (Δ) of the lasers for two different Rabi frequencies, $\Omega = 0.1\Gamma$ (red line) and 1.0Γ and is shown in Fig. 2.6 (a). Here, T_{D} is the Doppler temperature given by the formula:

$$T_{\mathrm{D}} = \hbar\Gamma/2k_{\mathrm{B}} \tag{2.84}$$

The temperature initially decreases, reaches a minimum, and then increases. At low intensity, the minimum temperature, i.e., T_{D}, is achieved at detuning equal to half the linewidth of the transition. If the Rabi frequency is increased, the minimum temperature of the atom increases, and also the position of the minima shifts away from the resonance. Thus, it is better to use lower power to achieve a lower OM temperature.

Next, we study the effect of Ω/Γ on the temperature at various detuning of the laser. The T/T_{D} vs. Ω/Γ plot is shown in Fig. 2.6 (b). The red line corresponds to the minimum temperature condition, i.e., when $\Delta = -\Gamma/2$. When the laser is close to resonance (green and orange curve), the temperature rises faster with Ω as compared to when the lasers are far red-detuned.

2.7.2 Temperature limit in a multi-level system

We extend these concepts to find the temperature of OM in a multi-level system, given by:

$$T = \frac{\sum_{i=1}^{M} (\hbar k_i)^2 \Omega_i \mathrm{Im}\left(\tilde{\rho}_i\right)\Big|_{v=0}}{\beta\Big|_{v=0}} \tag{2.85}$$

Here, M is the number of lasers. k_i is the wave vector of the i^{th} laser with rabi frequency $\Omega_i = \Omega_{mn}$ which drives the $|m\rangle \rightarrow |n\rangle$ transition. The CG coefficients should also be taken care of by using $\Omega_{ij} = \text{CG}_{ij}\Omega_0$ if $\text{CG}_{ij} \neq 1$. $\rho_i = \rho_{mn}$. β is the slope of the force vs. velocity curve at v=0, where the force can be calculated using the Eq. 2.74.

2.8 Sub-Doppler Cooling

Initially, the Doppler limit was considered to be the minimum achievable temperature in optical molasses (OM). However, Williams Philips' group, in an experiment, measured the temperature of the cold atomic cloud of sodium below the Doppler limit [7, 116]. This challenged the existing model of laser cooling. Cohen-Tannoudji introduced an explanation for this sub-Doppler cooling, considering the multiplicity of sub-levels within atomic states [89].

Two configurations were proposed based on laser polarization gradients: Lin $\perp$ Lin Polarization Gradient Cooling and $\sigma^+ - \sigma^-$ Polarization Gradient Cooling. The former involves spatially modulating the light shifts of ground-state Zeeman sublevels, inducing dipole forces and a Sisyphus effect. In the latter, the cooling mechanism differs significantly. At very low velocities, atomic motion generates a population difference among ground-state sublevels, leading to unbalanced radiation pressures [89].

We are focusing our discussions on $\sigma^+ - \sigma^-$ Polarization Gradient Cooling in this thesis because we have utilized laser beams in the $\sigma^+ - \sigma^-$ configuration in our experiments.

As discussed in Sec. 2.4.3, spontaneously generated coherence (SGC) plays a very important role in atomic systems with degenerate energy levels, causing modification in the absorption spectrum. We discuss the sub-Doppler cooling in $\sigma^+ - \sigma^-$, incorporating the important aspect of SGC. We continue our mathematical modeling discussed in the previous sections to study the sub-Doppler cooling of multi-level systems. Let us consider the $F = 1 \rightarrow 2$ (8 level) atomic system in the presence of two counterpropagating lasers in $\sigma^+ - \sigma^-$ configuration shown in Fig. 2.7. The objective is to determine the force experienced by the atom in this configuration. For that, we need to solve the density matrix equations (as discussed in Sec. 2.2). It requires the Hamiltonian of the moving atom (as discussed in Sec. 2.3.6) and the decay matrix (as discussed in Sec. 2.4.2).

In this system, there are three degenerate ground states and five degenerate excited states. It is possible to have SGC in this system since it has multiple decay matrix elements parallel to each other.

First, we shall write the Hamiltonian for a stationary atom following the steps

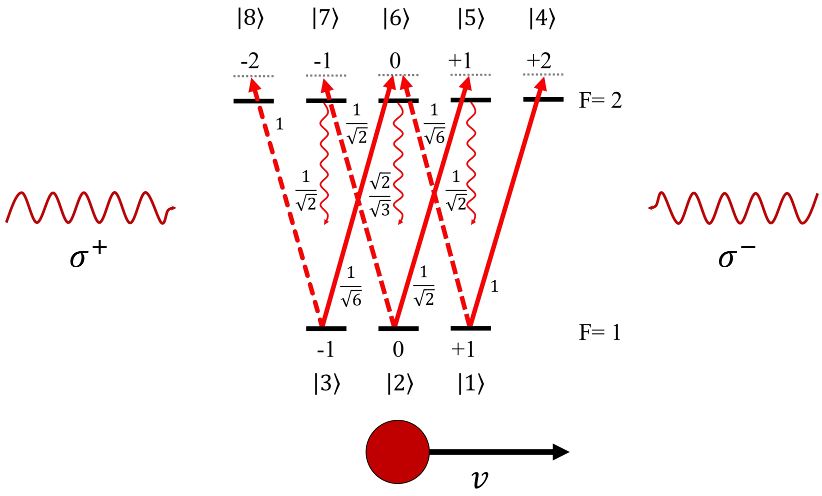

Figure 2.7: Energy level diagram of $F = 1 \rightarrow 2$ atomic system in presence of two counterpropagating lasers in $\sigma^+ - \sigma^-$ configuration. CG coefficients are shown near the transitions.

mentioned in Sec. 2.3.2.

$$H = \begin{bmatrix} 0 & 0 & 0 & \Omega_{14}/2 & 0 & \Omega_{16}/2 & 0 & 0 \\ 0 & 0 & 0 & 0 & \Omega_{25}/2 & 0 & \Omega_{27}/2 & 0 \\ 0 & 0 & -\Delta_{16}+\Delta_{36} & 0 & 0 & \Omega_{36}/2 & 0 & \Omega_{38}/2 \\ \Omega^*_{14}/2 & 0 & 0 & -\Delta_{14} & 0 & 0 & 0 & 0 \\ 0 & \Omega^*_{25}/2 & 0 & 0 & -\Delta_{25} & 0 & 0 & 0 \\ \Omega^*_{16}/2 & 0 & \Omega^*_{36}/2 & 0 & 0 & -\Delta_{16} & 0 & 0 \\ 0 & \Omega^*_{27}/2 & 0 & 0 & 0 & 0 & -\Delta_{27} & 0 \\ 0 & 0 & \Omega^*_{38}/2 & 0 & 0 & 0 & 0 & -\Delta_{16}+\Delta_{36}-\Delta_{38} \end{bmatrix}$$

For moving atoms, the following terms get modified:

$$\Delta_{14} = \Delta_{25} = \Delta_{36} = \Delta - kv \tag{2.86}$$

$$\Delta_{16} = \Delta_{27} = \Delta_{38} = \Delta + kv \tag{2.87}$$

Next, considering the CG coefficients and Rabi frequency as real, the following terms can be simplified:

$$\Omega_{14} = \Omega_{38} = \Omega \tag{2.88}$$

$$\Omega_{25} = \Omega_{27} = \Omega/\sqrt{2} \tag{2.89}$$

$$\Omega_{16} = \Omega_{36} = \Omega/\sqrt{6} \tag{2.90}$$

Thus, for the moving atoms, the Hamiltonian for the $F = 1 \rightarrow 2$ can be written as:

$$H = \begin{bmatrix} 0 & 0 & 0 & \frac{1}{2}\Omega & 0 & \frac{1}{2\sqrt{6}}\Omega & 0 & 0 \\ 0 & 0 & 0 & 0 & \frac{1}{2\sqrt{2}}\Omega & 0 & \frac{1}{2\sqrt{2}}\Omega & 0 \\ 0 & 0 & -2kv & 0 & 0 & \frac{1}{2\sqrt{6}}\Omega & 0 & \frac{1}{2}\Omega \\ \frac{1}{2}\Omega & 0 & 0 & -\Delta + kv & 0 & 0 & 0 & 0 \\ 0 & \frac{1}{2\sqrt{2}}\Omega & 0 & 0 & -\Delta + kv & 0 & 0 & 0 \\ \frac{1}{2\sqrt{6}}\Omega & 0 & \frac{1}{2\sqrt{6}}\Omega & 0 & 0 & -\Delta - kv & 0 & 0 \\ 0 & \frac{1}{2\sqrt{2}}\Omega & 0 & 0 & 0 & 0 & -\Delta - kv & 0 \\ 0 & 0 & \frac{1}{2}\Omega & 0 & 0 & 0 & 0 & -\Delta - 3kv \end{bmatrix}$$

This Hamiltonian is used for the further calculation. It can also be written in the shorter form: $H = H_A + H_I$, where

$$\begin{aligned} H_A = & -\hbar\big\{2kv\,|3\rangle\langle 3| + (kv-\Delta)\,|4\rangle\langle 4| + (kv-\Delta)\,|5\rangle\langle 5| \\ & -(kv+\Delta)\,|6\rangle\langle 6| - (kv+\Delta)\,|7\rangle\langle 7| \\ & -(3kv+\Delta)\,|8\rangle\langle 8|\big\} \end{aligned} \tag{2.91}$$

and

$$\begin{aligned} H_I = & \frac{1}{2}\hbar\Omega\big\{\,|1\rangle\langle 4| + \frac{1}{\sqrt{6}}|1\rangle\langle 6| + \frac{1}{\sqrt{2}}|2\rangle\langle 5| + \frac{1}{\sqrt{2}}|2\rangle\langle 7| \\ & + \frac{1}{\sqrt{6}}|3\rangle\langle 5| + |3\rangle\langle 8|\,\big\} + h.c. \end{aligned} \tag{2.92}$$

Now, let us first form the K matrix in the absence of SGC. Following the discussion as in Sec. 2.4.1, K can be given by a 8×8 matrix.

$$K = \Gamma \begin{bmatrix} \rho_{44} + \frac{1}{2}\rho_{55} + \frac{1}{6}\rho_{66} & 0 & 0 & -\frac{1}{2}\rho_{14} & -\frac{1}{2}\rho_{15} & -\frac{1}{2}\rho_{16} & -\frac{1}{2}\rho_{17} & -\frac{1}{2}\rho_{18} \\ 0 & \frac{1}{2}\rho_{55} + \frac{2}{3}\rho_{66} + \frac{1}{2}\rho_{55} & 0 & -\rho_{24} & -\frac{1}{2}\rho_{25} & -\frac{1}{2}\rho_{26} & -\frac{1}{2}\rho_{27} & -\frac{1}{2}\rho_{28} \\ 0 & 0 & \frac{1}{6}\rho_{66} + \frac{1}{2}\rho_{77} + \rho_{88} & -\frac{1}{2}\rho_{34} & -\frac{1}{2}\rho_{35} & -\frac{1}{2}\rho_{36} & -\frac{1}{2}\rho_{37} & -\frac{1}{2}\rho_{38} \\ -\frac{1}{2}\rho_{41} & -\frac{1}{2}\rho_{42} & -\frac{1}{2}\rho_{43} & -\rho_{44} & -\rho_{45} & -\rho_{46} & -\rho_{47} & -\rho_{48} \\ -\frac{1}{2}\rho_{51} & -\frac{1}{2}\rho_{52} & -\frac{1}{2}\rho_{53} & -\rho_{54} & -\rho_{55} & -\rho_{56} & -\rho_{47} & -\rho_{58} \\ -\frac{1}{2}\rho_{61} & -\frac{1}{2}\rho_{62} & -\frac{1}{2}\rho_{63} & -\rho_{64} & -\rho_{65} & -\rho_{66} & -\rho_{67} & -\rho_{68} \\ -\frac{1}{2}\rho_{71} & -\frac{1}{2}\rho_{72} & -\frac{1}{2}\rho_{73} & -\rho_{74} & -\rho_{75} & -\rho_{76} & -\rho_{77} & -\rho_{78} \\ -\frac{1}{2}\rho_{81} & -\frac{1}{2}\rho_{82} & -\frac{1}{2}\rho_{83} & -\rho_{84} & -\rho_{85} & -\rho_{86} & -\rho_{87} & -\rho_{88} \end{bmatrix} \tag{2.93}$$

Furthermore, the dipole moments associated with the transitions $|1\rangle \rightarrow |4\rangle$, $|2\rangle \rightarrow |5\rangle$, and $|3\rangle \rightarrow |6\rangle$ align parallelly (in σ^+). This alignment allows for SGC the decays channels $|4\rangle \rightarrow |1\rangle$, $|5\rangle \rightarrow |2\rangle$, and $|6\rangle \rightarrow |3\rangle$. Similarly, SGC is feasible through the decay channels $|6\rangle \rightarrow |1\rangle$, $|7\rangle \rightarrow |2\rangle$, and $|8\rangle \rightarrow |3\rangle$ (corresponding to σ^-) as well as $|6\rangle \rightarrow |1\rangle$, $|7\rangle \rightarrow |2\rangle$, and $|8\rangle \rightarrow |3\rangle$ (corresponding to π).

We incorporate the presence of SGC, and the following six terms of the K matrix get modified.

$$\begin{aligned}
K_{12} &= \Gamma(\tfrac{1}{\sqrt{2}}\rho_{45} + \tfrac{1}{\sqrt{3}}\rho_{56} + \tfrac{1}{2\sqrt{3}}\rho_{67}),\\
K_{13} &= \Gamma(\tfrac{1}{\sqrt{6}}\rho_{46} + \tfrac{1}{2}\rho_{57} + \tfrac{1}{\sqrt{6}}\rho_{68}),\\
K_{23} &= \Gamma(\tfrac{1}{2\sqrt{3}}\rho_{56} + \tfrac{1}{\sqrt{3}}\rho_{67} + \tfrac{1}{\sqrt{2}}\rho_{78}),\\
K_{21} &= \Gamma(\tfrac{1}{\sqrt{2}}\rho_{54} + \tfrac{1}{\sqrt{3}}\rho_{65} + \tfrac{1}{2\sqrt{3}}\rho_{76}),\\
K_{31} &= \Gamma(\tfrac{1}{\sqrt{6}}\rho_{64} + \tfrac{1}{2}\rho_{75} + \tfrac{1}{\sqrt{6}}\rho_{86}),\\
K_{32} &= \Gamma(\tfrac{1}{2\sqrt{3}}\rho_{65} + \tfrac{1}{\sqrt{3}}\rho_{76} + \tfrac{1}{\sqrt{2}}\rho_{87}) \qquad (2.94)
\end{aligned}$$

Finally, we solve the density matrix equation and obtain 64 simultaneous differential equations, presented in Sec. 7.2. We convert the K matrix to the form L following the steps in Sec. 2.4.2. The equations are numerically solved in MATLAB, and the force experienced by the atom is evaluated using the relation:

$$F_{\text{damp}} = \hbar k \Omega \, \text{Im}\Big[(\rho_{14} - \rho_{38}) + \frac{1}{\sqrt{2}}(\rho_{25} - \rho_{27}) + \frac{1}{\sqrt{6}}(\rho_{36} - \rho_{16})\Big] \qquad (2.95)$$

The force vs. velocity curve in the presence of a red-detuned laser is shown in Fig. 2.8. For a large velocity range (as shown in Fig. 2.8 (a)), the atoms experience the Doppler force in the direction opposite to its velocity, which leads to Doppler cooling. An interesting feature appears near the zero velocity group (as shown in Fig. 2.8 (b)), where the slope of the force vs. velocity curve is larger than the usual Doppler force. This feature appears due to the presence of multiple zeeman levels and the polarization gradient. This unusual feature is the origin of the sub-Doppler force. Since the slope of the sub-Doppler force is larger than the Doppler force, this results in the cooling below the Dopper temperature and is known as sub-Doppler cooling.

There are a few very important points associated with sub-Doppler cooling worth noting. The origin of the sub-Doppler force is associated with the SGC, which directly affects the terms in the decay matrix (given by Eq. 2.94 in our example). Since SGC is very sensitive to the degeneracy of the Zeeman energy levels, it is very fragile to the magnetic field. Thus, in MOT, SGC is averaged out, and sub-Doppler cooling is not possible. For sub-Doppler cooling to occur, the magnetic fields, including the stray magnetic field, need to be properly nullified; thus for sub-Doppler cooling, optical molasses are used. With this motivation, the effect of SGC in the laser cooling of atoms is further explored in Chapter 7.

2.9 Magneto-Optical Trap

Up to this point, we have explored the workings of laser cooling in optical molasses (OM). Despite achieving low temperatures for atoms, there is an issue- they tend

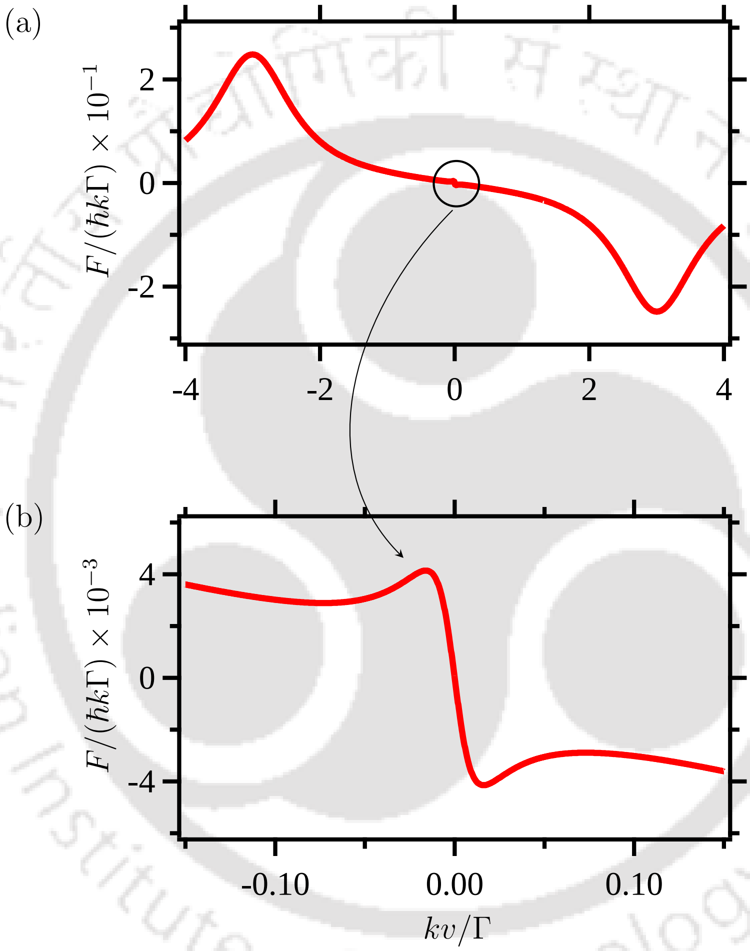

Figure 2.8: Force vs. velocity plots for the $F = 1 \rightarrow 2$ for (a) a large velocity range and (b) a small velocity range. The black-circled portion in (a) is magnified and illustrated in (b). Parameters: $\Delta_{1\rightarrow 2} = -3\Gamma$ and $\Omega = \Gamma/\sqrt{2}$.

to diffuse away due to a lack of proper spatial confinement in OM. To tackle this, we need a force of the form $F = -\alpha z$, where α is a positive constant. This force is achievable by using both optical and magnetic fields, creating what is known as a Magneto-Optical Trap (MOT). The first MOT was successfully demonstrated in 1987 [9]. In contrast to optical molasses, MOT stands out as a robust trap. It does not rely heavily on power balancing of the counterpropagating laser beams, and it is not overly sensitive to beam polarizations [6]. This robustness and ease of operation make the MOT a widely adopted method for laser cooling and trapping of neutral atoms.

Typically, a quadrupole magnetic field is used in MOT and is created by using a pair of current-carrying coils arranged in an anti-Helmholtz configuration. This setup generates a magnetic field gradient represented as $B = B'z$. In this configuration, the magnetic field is zero at the center and increases linearly away from the center. The MOT utilizes the Zeeman effect, where the presence of a magnetic field causes shifts in the Zeeman energy levels. By applying a magnetic field gradient represented as $B = B'z$, the degeneracy of Zeeman levels is altered by:

$$\Delta E = g_{\mathrm{F}} m_{\mathrm{F}} \mu_{\mathrm{B}} B \tag{2.96}$$

Here, g_{F} is the Lande-g factor, m_{F} is a magnetic quantum number, and μ_{B} is the Bohr magneton.

To understand the mechanism, let us consider a simple system: $F_{\mathrm{g}} = 0 \rightarrow F_{\mathrm{e}} = 1$ in the presence of two red-detuned counterpropagating lasers in $\sigma^+ - \sigma^-$ configuration. $F_{\mathrm{g}} = 0$ has one zeeman level ($|1\rangle$) and $F_{\mathrm{e}} = 1$ has 3 zeeman levels corresponding to $m_{\mathrm{F}} = +1, 0$ and -1. $m_{\mathrm{F}} = 0$ of the excited state can be ignored as no atom is excited to this state due to the selection rules. Let us label the levels corresponding to $m_{\mathrm{F}} = +1$ and $m_{\mathrm{F}} = -1$ as $|2\rangle$ and $|3\rangle$ respectively. In the absence of the magnetic field, $|2\rangle$ and $|3\rangle$ remains degenerate (as shown in Fig. 2.9 (b)). In the presence of a uniform magnetic field along the $-\vec{z}$ and $+\vec{z}$ directions, the energy levels shift according to the relation Eq. 2.96 and are shown in (a) and (c) respectively.

In the presence of a positive magnetic field, atoms scatter more photons from the σ^- light than the σ^+ light as the σ^- light is closer to the resonance. Thus, it experiences more force from the σ^- light than the σ^+ light. For trapping, as the atom needs to move towards the origin, it needs the net equivalent force along the negative direction. This is possible only when $\sigma^{-(+)}$ light propagates along the $-(+)\vec{z}$ direction.

Similarly, in the presence of a negative magnetic field, atoms experience larger force from the σ^+ light than the σ^- light. It needs the net equivalent force along the positive direction. Thus, the $\sigma^{-(+)}$ light must be along the $-(+)\vec{z}$ direction.

Now, in the presence of the quadrupole magnetic field of the form $B = B'z$, the energy levels of $|2\rangle$ and $|3\rangle$ vary spatially, as shown in Fig. 2.10. For $z \neq 0$, atoms experience a position-dependent force towards the center of the MOT. For two atoms

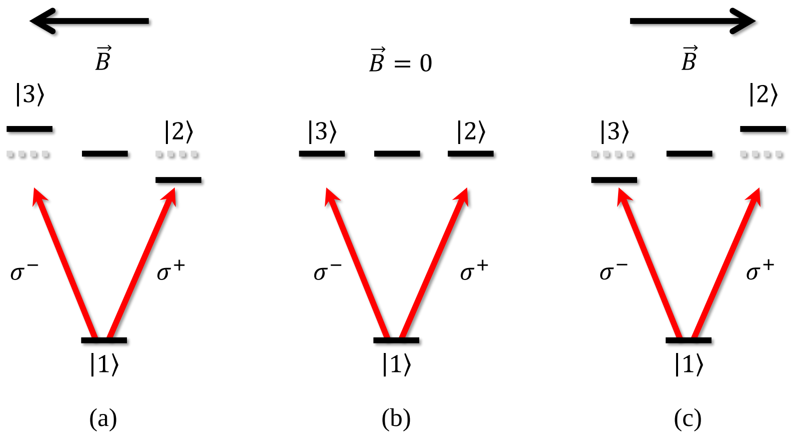

Figure 2.9: $F = 0 \rightarrow 1$ atom in the presence of (a) negative, (b) no and (c) positive magnetic fields.

with the same velocity, the atom closer to the center experiences lesser force than the atom away from the center. Thus, when the atom moves closer and closer to the center of the trap, it experiences lesser and lesser force. This force is dominantly from the $\sigma^-(+)$ light for the atom in the $+(-)$ direction.

This scenario is similar to the velocity damping observed in optical molasses due to the Doppler effect. However, there is a key distinction: here, the effect operates in position space, whereas in optical molasses, the effect operates in velocity space.

The force experienced by the atom in MOT can be given by the same expression as in 3 level V system:

$$\vec{F} = \hat{z}\hbar k \Omega_0 \mathrm{Im}\big(\tilde{\rho}_{12} - \tilde{\rho}_{13}\big) \tag{2.97}$$

However, the detuning terms of the Hamiltonian of the 3-level system are modified as:

$$\Delta_{12} = \Delta - kv + \alpha z \tag{2.98}$$

$$\Delta_{13} = \Delta + kv - \alpha z \tag{2.99}$$

Here $\alpha = \mu' B'/\hbar$ and $\mu' = (g_e m_e - g_g m_g)\mu_B$ is the effective magnetic moment for the transitions [6].

When both the Doppler shift and the Zeeman shifts are small, in that case, the force can be simplified as [6]:

$$\vec{F} = -\beta\vec{v} - \kappa\vec{z} \tag{2.100}$$

where the terms of the orders $(kv/\Gamma)^4$ or higher are neglected. $\beta = \frac{8\hbar k^2 \Delta s_0}{\Gamma(1+s_0+(2\Delta/\Gamma)^2)^2}$, $s_0 = 2\Omega^2/\Gamma^2$ and $\kappa = \frac{\mu' B'}{\hbar k}\beta$.

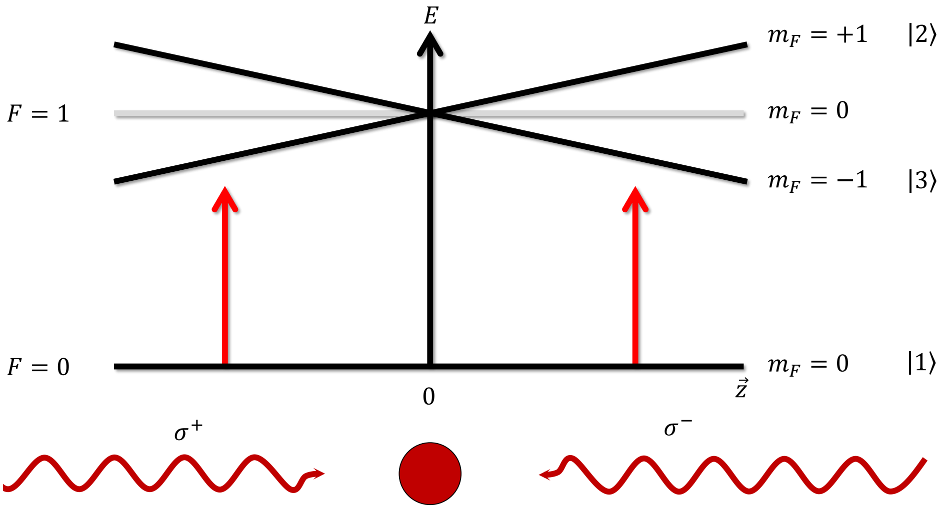

Figure 2.10: One dimensional schematic of a MOT for $F = 0 \rightarrow 1$ transition. Magnetic sublevels are split in the magnetic field gradient, making it more likely for atoms to absorb the red-detuned photons that tend to push them toward the center of the trap.

The force given by Eq. 2.100 results in the overdamped harmonic motion of the atoms.

Another important term associated with the MOT is capture velocity. It is defined as the maximum velocity of the atoms below which they can be trapped in the MOT. Assuming that the atoms scatter photons at the maximum possible rate $\Gamma/2$ across an entire beam diameter D, an expression for the capture velocity is given by,

$$v_c = \sqrt{2\frac{\hbar k \Gamma}{2m} D} \tag{2.101}$$

where m is the atomic mass and $k = 2\pi/\lambda$ is the wave number of the MOT light [117, 118].

2.10 Conclusion

To summarize, we have discussed in detail the cooling and trapping of atoms in a magneto-optical trap. Starting with the density matrix formalism, we discussed how to construct the Hamiltonian for different systems, even for those involving moving atoms. The Lindbladian of the system was then discussed, and we covered a brief overview of spontaneously generated coherence and how to include it in the density matrix equations. Using this framework, we discussed the Doppler cooling in a two-level system and the sub-Doppler cooling in optical molasses with a transition from $F = 1 \rightarrow 2$. We also gave the formalism to extend these concepts to other complicated atomic systems. Finally, we gave a quick overview of the magneto-optical trap. In the next chapter, we discuss the experimental details associated with the magneto-optical trap.

CHAPTER 3

Experimental Details

Contents

Carrying out a successful laser cooling and trapping experiment involves paying close attention to important details. Knowing the energy levels and transition wavelengths of the target atom is crucial for laser-based excitations. Stable laser frequencies are achieved through spectroscopy techniques like saturated absorption spectroscopy, polarization spectroscopy, and/or double resonance spectroscopy. The three pairs of counterpropagating laser beams from three orthogonal directions along with the quadrupole magnetic field make the basic structure of the magneto-optical trap (MOT). The MOT setup also requires an ultra-high vacuum. The absorption imaging techniques become crucial for the characterization of cold atoms. As experiments advance, the need for precision in controlling experimental parameters highlights the necessity of a computer control system.

In this chapter, we explore the atomic structure of Rubidium, mainly the relevant energy levels, hyperfine structures, and transition wavelengths crucial for our experiments. Following this, we provide an overview of our laser system, and discuss the strategies for frequency stabilization using spectroscopy techniques. From converting the atomic spectra into error signals to addressing transitions within the Magneto-Optical Trap (MOT) chamber, this chapter discusses key aspects of our experimental setup. We also discuss the characterization of the MOT and conclude with a discussion of our computer control system.

3.1 Atomic structure of Rubidium

In this section, we discuss the structure of the Rubidium (Rb) atom. It is an alkali metal with an atomic number of 37, placing it in Group 1 of the periodic table below Li, Na, and K. It has two stable isotopes: ^{85}Rb (72.2% abundance) and ^{87}Rb (27.8% abundance). The electronic configuration of Rb is [Kr]5s^1. It has a single valence electron in its outermost shell, which determines its high reactivity in chemical processes, requiring a high vacuum for conducting any atomic physics experiment with Rb. In terms of spectroscopic notation, Rb has a ground state of 5S$_{1/2}$, where the outermost electron resides in the $n = 5$, $L = 0$ shell with an angular momentum quantum number $J = \frac{1}{2}$.

The fine structure of Rb includes the ground state 5S$_{1/2}$ and important excited states such as 5P$_{1/2}$, 5P$_{3/2}$, 6P$_{1/2}$ and 6P$_{3/2}$ etc. These fine structures result from the coupling of the orbital angular momentum (L) of the outermost electron with the spin angular momentum (S). In general, $J = L+S$ and J take values in between $|L - S|$ to $L + S$. The relevant fine structures of ^{85}Rb and ^{87}Rb are shown in Fig. 3.1. Transitions such as 5S$_{1/2}$ → 5P$_{1/2}$ at 795 nm (D$_1$ line) and 5S$_{1/2}$ → 5P$_{3/2}$ at 780 nm (D$_2$ line) lies in infrared (IR) spectrum of the electromagnetic (EM) radiation. Transitions such as 5S$_{1/2}$ → 6P$_{1/2}$ at 421 nm (D$_1$ line) and 5S$_{1/2}$ → 6P$_{3/2}$ at 420 nm (D$_2$ line) lies in blue spectrum of the EM radiation. These transitions are commonly used in any atomic physics experiments with Rb.

Additionally, the isotopes, ^{85}Rb and ^{87}Rb exhibit nuclear spins of $I = \frac{5}{2}$ and $I = \frac{3}{2}$. The nuclear angular momentum (I) couples with J to further split the fine structures into hyperfine structures (F). In general, $F = I + J$ and F take values in between $|I - J|$ to $I + J$. Relevant hyperfine levels with the energy splittings are shown in Fig. 3.1. For example, 6P$_{3/2}$ state of ^{87}Rb has $J = 3/2$ and $I = 3/2$. Thus F can take values in between 0 and 3. Thus, this splits into the hyperfine states $F = 0, 1, 2,$ and 3.

Furthermore, each hyperfine level consists of $2F+1$ degenerate zeeman levels. Each Zeeman level is characterized by the magnetic quantum number m_{F} which takes the values from $-F$ to $+F$ with an increase of 1. For example, 6P$_{3/2}$, $F = 2$ state of ^{87}Rb has 5 degenerate Zeeman energy levels and are given by $m_{\mathrm{F}} = -2, -1, 0, +1,$ and $+2$. In the presence of a magnetic field, this degeneracy is lifted. The corresponding energy level shift is given by [6]:

$$\Delta E = g_{\mathrm{F}} m_{\mathrm{F}} \mu_{\mathrm{B}} B \tag{3.1}$$

Here, g_{F} is the Lande-g factor, m_{F} is a magnetic quantum number, μ_{B} is the Bohr magneton, and B is the applied magnetic field.

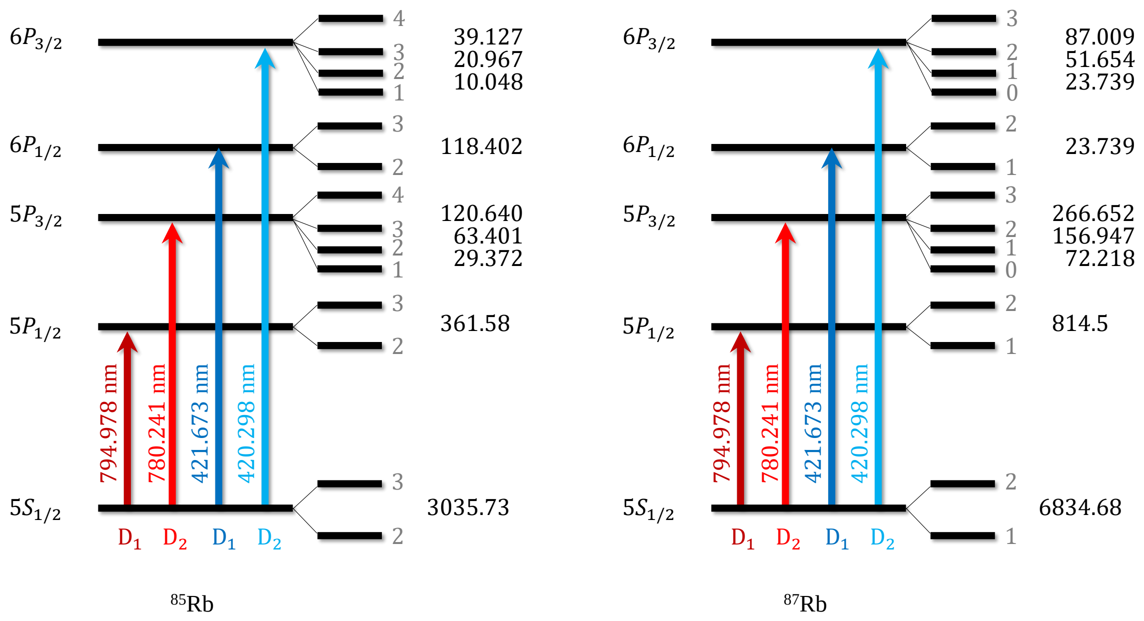

Figure 3.1: Relevant energy levels of ^{85}Rb and ^{87}Rb. The hyperfine splittings are shown in MHz units.

3.1.1 Selection Rules

Not all the excitation and de-excitations are possible in an atomic system. They are governed by some selection rules [6]. The dipole-allowed hyperfine transitions occur with changes in the quantum number ΔF, where ΔF represents the difference between the initial state F_i and the final state F_j for a given transition. Specifically, these transitions are characterized by $\Delta F = 0, \pm 1$. Notably, the transition $F = 0 \rightarrow 0$ is not allowed as it is a forbidden transition.

Moving to Zeeman transitions, the allowed changes in magnetic quantum number Δm_{F} are limited to 0 and ± 1. Here, Δm_{F} corresponds to the difference between the initial state $m_{\mathrm{F_i}}$ and the final state $m_{\mathrm{F_j}}$ for a given transition. It's crucial to emphasize that the transition $m_{\mathrm{F}} = 0 \rightarrow 0$ is not allowed when $\Delta F = 0$. Furthermore, the transitions $\Delta m_{\mathrm{F}} = 0, +1$, and -1 are selectively permitted, corresponding to π, σ^+, and σ^- polarized radiations, respectively.

3.2 Laser system

Lasers play a significant role in atomic physics, offering unique capabilities that drive advancements in precise control and manipulation of atoms. The significance of lasers lies in their ability to provide coherent, monochromatic light with well-defined characteristics, such as a specific wavelength and narrow linewidth. Typically, a laser diode has a resonator length of around 300 μm which corresponds to the free spectral range of the order of 100 GHz. However, the linewidths of atomic transitions are of the order of MHz. Therefore, it is necessary to have laser linewidth as narrow as possible. In this context, the External Cavity Diode Laser (ECDL) serves as the most crucial laser system due to its narrow linewidth and continuous frequency tunability.

The setup of an ECDL involves a laser diode, a collimating lens, and a diffraction grating configured in the Littrow or Littman configuration. In principle, both configurations allow a similar range of frequency tunability. In Littrow configuration, the first order diffracted beam is fed back to the laser diode and the zeroth order beam serves as the output. The Littman configuration uses an additional mirror for reflecting the first-order diffracted beam to the laser diode. This makes the Littman configuration more complex than the Littrow configuration and prone to more acoustic and thermal noise. Because the grating face forms an additional cavity with the back face of the laser diode (apart from the internal cavity of the laser diode), both configurations are known as external cavity diode lasers. For our work, we have used the Littow configuration of the ECDLs.

Refer to Fig. 3.2 for a typical image of our self-assembled ECDL in the Littrow configuration. The grating is mounted over a piezo, which undergoes length changes upon applied voltage via the piezo driver. The position of the grating in the Littrow configuration is such that when it rotates, the length of the cavity is also changed, effectively changing the output laser's frequency. The output laser frequency is determined by the interplay between the laser diode gain profile, grating profile, and internal and external resonator mode structures. The following equation can be used for roughly selecting the required grating.

$$2d \sin\alpha = \lambda \tag{3.2}$$

Here, d is the spacing between the successive grooves, α is measured with reference to the grating normal and λ is the wavelength. Typically available different types of gratings are 3600 l/mm, 2400 l/mm, 1800 l/mm, 1400 l/mm, 1100 l/mm, and 1000 l/mm for 380 nm - 450 nm, 600 nm - 650 nm, 650 nm - 910 nm, 910nm - 1100 nm, 1100 nm - 1400 nm, and 1400 nm - 1600 nm respectively. As an example, for wavelength at 780 nm, a grating with 1800 l/mm can be used and it should be put at an angle of $\alpha = 44.59^0$. Similarly for 420 nm, a grating with 3600 l/mm can be used and it should be put at an angle of $\alpha = 49.12^0$. By changing the piezo voltage, continuous frequency tuning can be achieved.

Two types of ECDLs have been used in our experiments: one is commercially available ECDL at 420 nm from Toptica (model: DL Pro HP) and others are home-assembled 780 nm ECDLs. The 780 nm ECDLs include laser diodes from Thorlabs (model: L785H1 (high power) and L785P090 (low power)). Additionally, we have used the commercially available current and temperature controllers from Toptica (Model: DCC 110 and DTC 110) for controlling the laser diode currents and temperatures. For tuning the piezo voltage for the 780 nm lasers, we have used a Piezo

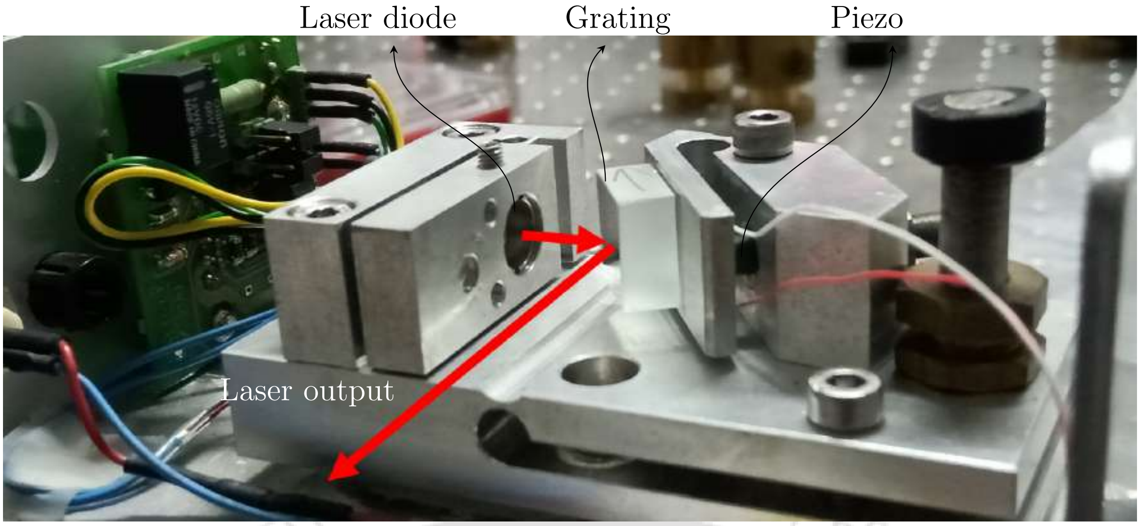

Figure 3.2: Image of the home assembled ECDL in Littorw configuration.

controller from Thorlabs (model: MDT693B) and for the 420 nm laser, a scan controller (model: SC 110) from Toptica is used. All the controllers from Toptica are placed in a double-stage supply rack (Make: Toptica).

The single-mode operation and the wavelength of the blue laser are monitored on a wavelength meter from Highfinesse GmbH (model: WS7-60). Two isolators (I-80-U4 from Isowave, and IO-5-780-HP from Thorlabs) are used in front of the IR lasers. These isolators protect the laser diodes by preventing back-reflections from the optical elements used in the experiments.

3.3 Frequency stabilization techniques

Although the ECDL provides continuous frequency tunability and narrow linewidth, it faces the challenge of undesirable frequency drift, often induced by external factors such as temperature fluctuations, mechanical disturbances, and environmental conditions. This can compromise the accuracy and reliability of the laser system, making it essential to address this challenge, especially in the context of experiments like MOT.

Spectroscopic techniques emerge as valuable tools for countering these challenges. By employing methods like saturated absorption spectroscopy and polarization spectroscopy, researchers can actively monitor the laser frequency and implement feedback mechanisms. These techniques enable real-time adjustments, actively locking the ECDL onto the desired atomic transition. The result is a stabilized laser system that maintains precise control over its frequency, providing the necessary foundation for conducting detailed and reliable atomic physics experiments, particularly in the context of cold atom manipulation and trapping.

Mainly three spectroscopic techniques have been used in our experiments: Saturated absorption spectroscopy (SAS), Polarization spectroscopy (PS), and double resonance spectroscopy (DRS).

3.3.1 Saturated absorption spectroscopy

SAS is a common technique in atomic physics, particularly for exploring the hyperfine spectrum of atoms [119]. The method involves sending a pump beam and a probe beam through a vapor cell, typically in counterpropagating directions. When the probe beam goes through the vapor cell without the pump beam and is detected on a photodetector, it exhibits a Doppler profile due to its interaction with atoms moving at different velocities. This scenario does not reveal the hyperfine spectrum.

However, in the presence of the pump beam, when the pump beam frequency matches with the resonant frequency, it induces excitation. The high power of the pump beam ensures saturation, preventing further atom excitation. Consequently, when the probe beam frequency matches the resonance frequency, it encounters no absorption, resulting in a distinctive saturated absorption dip within the absorption profile. This dip signifies the presence of allowed hyperfine transitions.

In addition to the distinctive saturated absorption dips corresponding to allowed hyperfine transitions, SAS reveals extra features known as crossover peaks. These additional peaks originate from the interaction of two distinct velocity groups of atoms with the probe and pump lasers. Notably, the crossover peaks occur precisely in the middle of two real peaks in the absorption spectrum. Furthermore, the hyperfine pumping mechanism plays an important role in SAS where atoms have multiple hyperfine ground states [120]. Both the real and cross-over peaks can be utilized for frequency stabilization of the ECDL.

The SAS spectrum cannot directly be used for the frequency stabilization of the ECDL. First, it must be converted to an error signal. This conversion involves modulating the frequency of the probe and/or pump beam and then demodulating the photodetector signal. The laser's frequency modulation can be achieved by adjusting the current, piezo voltage, or externally using acousto-optic modulators (AOM). If an AOM is used for frequency modulation, it should be used in a double-pass configuration.

3.3.2 Polarization spectroscopy

There is another widely used technique, known as Polarization spectroscopy [119, 121], which offers an advantage by providing the error signal without the need for modulating the frequency of pump or probe beams. This method shares some common features with the Faraday rotation of light, a phenomenon observed when a laser beam traverses a Faraday-active medium. In the Faraday effect, a magnetic field is applied to induce circular birefringence. However, in polarization spectroscopy, the strong pump beam causes the birefringence. The magnetic field is applied only to provide a quantization axis. In this scenario, the two circularly polarized components of the light undergo different absorption within the medium. By detecting the differential absorption between these components, polarization spectroscopy effortlessly generates the error signal.

3.3.3 Double resonance spectroscopy

Double resonance spectroscopy (DRS) represents another powerful approach in atomic physics, distinguishing itself from traditional methods such as SAS [122, 123]. While SAS concentrates on the resonant interaction of a laser with a single atomic transition, DRS takes advantage of simultaneous resonance with two distinct atomic transitions. Unlike SAS, DRS avoids the appearance of crossover peaks within the real peaks, which may be helpful when energy levels are closely spaced. Additionally, DRS eliminates the need to heat the vapor cell for spectroscopy of narrow transitions. However, it is essential to note that DRS tends to offer a larger linewidth of absorption compared to SAS. Similar to SAS, DRS requires converting the spectrum to an error signal by modulating the frequency of the pump or probe, making it suitable for frequency stabilization of the ECDL.

3.3.4 Absolute frequency shift due to spectroscopy setup

When employing current modulation or piezo voltage modulation, the absolute frequency of the laser remains unchanged. However, these methods lead to undesired modulation of the MOT lasers, adversely affecting the quality of the MOT. In contrast, the use of an external AOM for frequency modulation of the probe and/ or pump beam of the spectroscopy setup ensures that the MOT lasers remain unmodulated. However, this introduces changes in the absolute frequency of the laser. Commonly, the AOMs are used in double-pass configurations to avoid misalignment due to the change in frequency. Three different possibilities exist:

AOM on the path of both pump and probe beam

A commonly employed technique involves placing an AOM with a frequency shift of Δ_{AOM} on the path of a beam before it is used to generate the pump and probe beams. Thus, the pump and probe beam undergoes a frequency shift of Δ_{AOM}. If the spectrum peak appears at ω_0, the relationship with the laser frequency ω_L is given by $\omega_L = \omega_0 - \Delta_{\mathrm{AOM}}$. Essentially, if the AOM is upshifted by Δ_{AOM}, the absolute frequency of the laser is at the frequency downshifted by the same amount. This method is employed for the frequency stabilization of the repumper laser in Chapter 7.

AOM on the path of only pump beam

While less common, placing an AOM solely on the path of the pump beam proves useful. Since the probe beam remains unmodulated, this setup enhances the signal-to-noise ratio compared to the previous case. We utilized this configuration for the frequency stabilization of the 420 nm laser in Chapters 4-8. If the pump beam is upshifted by $2 \times \Delta_{\mathrm{AOM}}$, then the absolute frequency of the laser is at frequency downshifted by Δ_{AOM}.

AOM on the path of only probe beam

Although not a widely adopted technique, placing an AOM solely on the path of the probe beam may find utility in specific experiments. If the probe beam is upshifted by $2 \times \Delta_{\mathrm{AOM}}$, then the absolute frequency of the laser is at frequency downshifted by Δ_{AOM}.

3.3.5 Addressing the correct transitions

In a MOT, ensuring that all laser beams accurately address the desired atomic transitions is essential. Additionally, the ability to switch these beams on/off during the experimental cycle requires the incorporation of an AOM on their path. Consider a laser frequency denoted as ω_L, and the required addressing frequency as ω_0. The AOM frequency should then be set to $\omega_0 - \omega_L$.

For instance, suppose the IR MOT laser is locked using polarization spectroscopy corresponding to the $5S_{1/2}$, F$=2 \rightarrow 5P_{3/2}$, F$=(2,3)$ crossover peak, with no AOM used on the spectroscopy path. If the IR MOT beam in the MOT chamber needs to be $-2\pi \times 10$ MHz red-detuned from the $5S_{1/2}$, F$=2 \rightarrow 5P_{3/2}$, F$=3$ transition, the correct AOM frequency on the IR MOT beam path would be $+(2\pi \times \frac{1}{2} \times 266.65 - 10) = +2\pi \times 123.325$ MHz, where $2\pi \times 266.65$ MHz is the separation between the F$=2$ and F$=3$ peaks.

As another example, consider the need for a blue MOT beam in the MOT chamber $-2\pi \times 3$ MHz detuned from the $5S_{1/2}$, F$=2 \rightarrow 6P_{3/2}$, F$=3$ transition. If the blue laser is locked corresponding to the $5S_{1/2}$, F$=2 \rightarrow 6P_{3/2}$, F$=3$ peak using the SAS technique, and an AOM in a double-pass configuration with a frequency of $-2\pi \times 2 \times 46.75$ MHz is used only on the path of the control beam of the spectroscopy

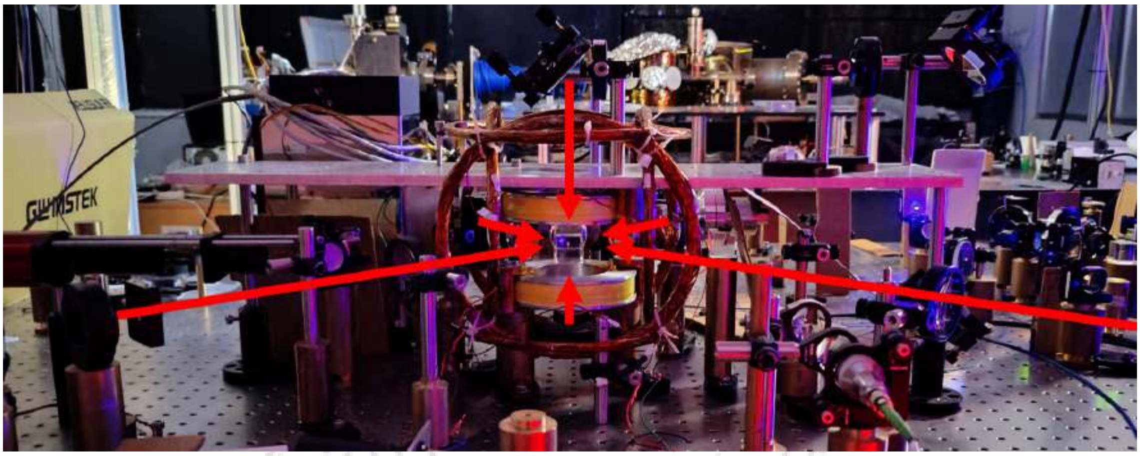

Figure 3.3: Image of the MOT setup

setup, the correct AOM frequency on the blue MOT beam path would be $-2\pi \times (46.75 + 3) = -2\pi \times 49.75$ MHz. The detuning of the blue MOT beam can then be calculated using $\Delta = \Delta_{\text{MOT}} - \frac{1}{2}\Delta_{\text{control}} = (-2\pi \times 49.75) - 2\pi \times \frac{1}{2}(-2 \times 46.75) = -2\pi \times 3$ MHz. Here, Δ_{MOT} and Δ_{control} are the frequencies of the AOMs on the MOT beam path and the control beam path, respectively. To change the detuning of the blue MOT beam, Δ_{control} can be adjusted as it does not alter the alignment, while Δ_{MOT} should remain constant as it affects the alignment of the blue MOT beam.

3.4 MOT setup

The magneto-optical trap (MOT) apparatus used in these experiments closely follows the design outlined in [124], comprising a rectangular glass chamber with dimensions 100 mm × 25 mm × 25 mm and is shown in Fig. 3.3.

The pressure inside the glass chamber is 10^{-10} mbar. To achieve and sustain the required vacuum, a sequence of pumps is employed: a rotary pump (Pfeiffer Vacuum), a turbo-molecular pump (Pfeiffer Vacuum, Hipace 300 H), and an ion pump (Agilent, VacIon Plus 75). Additionally, the vacuum setup undergoes an additional baking process at 200 ^{0}C for a week for degassing. The glass chamber is connected to the ion pump, operating with a pumping speed of 75 l/s, through a 4-way cross. Atomic rubidium vapor is introduced into the chamber by applying a 2.2 A current to a dispenser (AlfaSource Rubidium, model: AS-Rb-0090-2C-RbBi40) via an electric feedthrough at the opposite end of the 4-way cross.

The MOT setup incorporates an Anti-Helmholtz coil for the generation of a quadrupole magnetic field and three pairs of Helmholtz-configured shim coils to eliminate stray fields. The Anti-Helmholtz coil, capable of producing an 18 G/cm magnetic field gradient at a current of 1 A, comprises coils with specific dimensions: inner diameter (7 cm), outer diameter (13 cm), thickness (3 cm), and 500 turns. For rapid switching of the magnetic field, a high-current switch based on an insulated-gate bipolar transistor (IGBT) is employed, with a switching-off time of approximately 20 μs.

The optical part of the MOT setup consists of three laser beam arms. Prior to entering the MOT chamber, all beams are co-propagated with correct polarization. Galilean telescopes expand the beams tenfold, and proper circularization is achieved using dual quarter-wave plates. The beams are retro-reflected back using another combination of dual quarter-wave plate and mirror.

3.5 Characterization of MOT

Characterizing the MOT cloud involves determining the number of trapped atoms, their temperature, and the optical density (OD) of the cloud. This is achieved through absorption imaging, a technique utilizing a near-resonant probe beam, referred to as the imaging beam. The cold atoms selectively absorb this beam, generating a shadow image where darker regions correspond to higher atomic density. Captured by a camera, this image offers valuable insights into the spatial distribution of trapped atoms. Subsequent analysis of the absorption image enables us to precisely quantify parameters such as the number of atoms and temperature.

In our experiment, the imaging beam addresses the $5S_{1/2}$, F= 2 $\rightarrow$ $5P_{3/2}$, F= 3 transition. It is derived from the IR MOT laser. It is passed through an AOM in a double pass configuration for detuning adjustments and on/off control. The spatial mode is cleaned to Gaussian via a polarization-maintaining single-mode fiber. Afterward, the beam is expanded and collimated using a combination of lenses to adequately cover the entire atomic cloud. The imaging beam has a power of approximately 3 μW, with a diameter of 20 mm. Images are captured on a CMOS camera (Thorlabs, CS135MUN, pixel size: 4.8 μm $\times$ 4.8 μm) employing an imaging system with a demagnification of 0.3342. The camera's exposure time is set at 200 μs, during which the imaging beam is active for 100 μs.

The cloud is allowed to undergo free expansion by switching off all the beams and the magnetic field. Three images are captured for each time of flight: one with MOT (I_{MOT}), one reference beam (I_{Ref}), and one for the background (I_{BG}).

A MATLAB program is employed to analyze these images. From each set of 3 images, at first region of interest (ROI) is selected and the unnecessary part is cropped. Then a parameter b, known as Transmission, is calculated using the equation:

$$b = -ln\left[\frac{I_{MOT} - I_{BG}}{I_{Ref} - I_{BG}}\right] \tag{3.3}$$

3.5.1 Radii and optical density of the cloud

From the transmission profile, by summing the pixel values row-wise and column-wise, two Gaussian profiles can be obtained which can be used to determine the peak position of the transmission, background level and the size of the gaussian can be obtained by fitting the profiles with equation:

$$z = A + B \times \exp\left[-(x_i - x_0)^2/2\sigma_x^2\right] \tag{3.4}$$

where A is the background level, B is the amplitude of the Gaussian, x_i denotes the column (or row) number, x_0 is the position of maxima and σ_x is the $\frac{1}{\sqrt{e}}$ radius. Here, $\frac{1}{\sqrt{e}}$ radius is chosen purposefully in order to simplify the future calculation. σ_x in the gaussian function is also the standard deviation. The initial guess for the above equation is chosen as follows: x_0 = position corresponding to a maximum value of z which is max(z), A = $\frac{x_1+x_2}{2}$, B = $max(z) - A$ and σ_x = separation between the position corresponding to max(z) and $\frac{max(z)}{\sqrt{e}}$.

From the 2 Gaussian fits, position of maxima (x_0, y_0) and $\frac{1}{\sqrt{e}}$ radii σ_x and σ_y are extracted and used as initial guess for 2D Gausian fit of the Transmission dataset. The fit equation used is:

$$b = a_0 + b_0 \times \exp\left[\frac{-(x_i - x_0)^2}{2\sigma_x^2} + \frac{-(y_i - y_0)^2}{2\sigma_y^2}\right] \tag{3.5}$$

Here, a_0 and b_0 are chosen as A and B as initial guesses.

From this 2D Gaussian fit, finally, maximum OD, b_0 and radii of the cloud σ_x and σ_y are obtained and these values are used to calculate the number density, the number of atoms and the temperature of the cloud.

The obtained radii are in terms of the pixels and thus we need to multiply them by the size of one pixel in order to get it in μm unit. This is the radii of the image of the cloud in μm unit. To get the actual size of the MOT cloud, we have to multiply it with M, the magnification of the imaging system.

3.5.2 Number density

From Beer-Lambert's law, we can write that

$$\begin{aligned} \frac{dI}{I} &= -n(x,y,z) \times \sigma_{ph} \times dz && (3.6)\\ \implies I &= I_0 \times \exp\left[-\int_{-\infty}^{\infty} n(x,y,z) \times \sigma_{ph} \times dz\right] && (3.7)\\ &= I_0 \times \exp\left[-OD(x,y)\right] && (3.8)\\ \implies OD(x,y) &= -\int_{-\infty}^{\infty} n(x,y,z) \times \sigma_{ph} \times dz && (3.9) \end{aligned}$$

Assuming, $n(x,y,z) = n_0 \times \exp\left[\frac{-(x_i-x_0)^2}{2\sigma_x^2} + \frac{-(y_i-y_0)^2}{2\sigma_y^2} + \frac{-(z_i-z_0)^2}{2\sigma_z^2}\right]$,

we have:

$$OD(x,y) = n_0 \times \sigma_{ph} \times \sigma_z \times \exp\left[\frac{-(x_i-x_0)^2}{2\sigma_x^2} + \frac{-(y_i-y_0)^2}{2\sigma_y^2}\right] \tag{3.10}$$

Hence,

$$OD_0 = \sqrt{2\pi} n_0 \sigma_{ph} \sigma_z \tag{3.11}$$

where $\sigma_{ph} = \frac{3\times\lambda^2}{2\pi}$ is cross-section at resonance and λ is wavelength of laser.

As the captured image is a 2D image, we can not have exact information of σ_z. From the symmetry of the MOT beams, we can assume that $\sigma_z = \sigma_{min} = min(\sigma_x, \sigma_y)$ for maximum value of number density. Therefore, the maximum number density of the trapped atoms is:

$$n_{0,max} = \frac{OD_0}{\sqrt{2\pi}\sigma_{ph}\sigma_{min}} \tag{3.12}$$

3.5.3 Number of trapped atoms

The number of trapped atoms can therefore be calculated as:

$$N = \int_{-\infty}^{\infty} n(x,y,z) dxdydz$$

$$\implies N = n_0 \times \int_{-\infty}^{\infty} \exp\left[\frac{-(x_i-x_0)^2}{2\sigma_x^2} + \frac{-(y_i-y_0)^2}{2\sigma_y^2} + \frac{-(z_i-z_0)^2}{2\sigma_z^2}\right] dxdydz$$

Therefore,

$$N = 2\pi^{3/2} n_0 \sigma_x \sigma_y \sigma_z \tag{3.13}$$

3.5.4 Temperature of the cold atoms

Radius of classical gas with number density,

$$n(x,y,z) = n_0 \times \exp\left[\frac{-(x_i-x_0)^2}{2\sigma_x^2} + \frac{-(y_i-y_0)^2}{2\sigma_y^2} + \frac{-(z_i-z_0)^2}{2\sigma_z^2}\right]$$

under free expansion follows the equation [125]:

$$\sigma_x^2 = \sigma_{x,0}^2 + \left(\frac{k_B T}{m}\right) \times \text{TOF}^2 \tag{3.14}$$

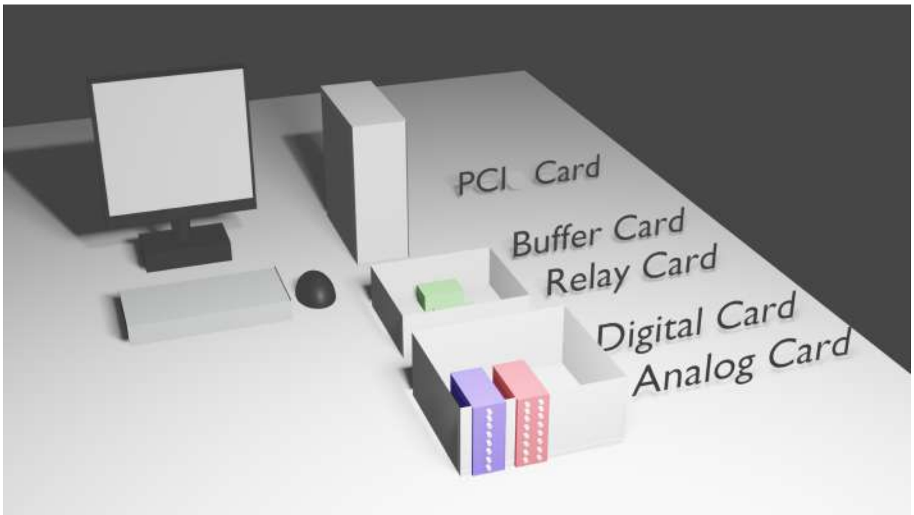

Figure 3.4: Schematics of the computer control system

Therefore, by analyzing the images for the two time of flights, the temperature of the cloud can be extracted by using the following equation:

$$T = \frac{m}{k_\mathrm{B}} \times \left[\frac{\sigma_2^2 - \sigma_1^2}{\mathrm{TOF}_2^2 - \mathrm{TOF}_1^2}\right] \tag{3.15}$$

3.6 Computer control system

In experiments with cold atoms, it is really important to use a computer control system. This ensures precision, repeatability, and real-time adaptability of experimental parameters. Dealing with laser cooling experiments requires careful control over things parameters like laser switching, power and detuning, magnetic fields, and capturing the image of the atomic cloud. The computer control system helps to smoothly manage and coordinate all the different parts of the experiment. It allows for running complicated experimental sequences and adapting quickly to any changes in the experiment. It also helps with collecting, processing, and storing the data, making the whole experiment more organized and ready for detailed analysis.

We have designed both the hardware and software of the computer control system. The schematic of our computer control system is shown in Fig. 3.4. The system is based on the PCI-DIO-32HS card from National Instruments. The time sequence is entered on the user interface. The software converts the sequence into 32-bit integers out of which 25 bits are actually in use for the system. The first 16 bits carry the data information, the next 8 bits carry the address information, and the 25th bit is used as a strobe which is responsible for the trigger at which various cards compare the address and accept the data.

The 32-bit signal is first sent to the buffer card from the PCI card via a 68-pin female-

female connector. The buffer card extracts 25 relevant data bits, organizes them, and sends them for further processing. Additionally, the buffer card is responsible for converting the strobe signal with a pulse width of around 150 ns. The 25 data bits are then transferred to the Relay card to enhance the weak signal and isolate the buffer and PCI cards from other instruments and other circuits. From the relay card, the digital, and analog cards are connected via a 50-pin ribbon connector. All the digital signals are connected to digital cards, and all the analog signals are connected to analog cards.

Each digital card has 16 channels and each channel can offer 0 and/ or 5 V. Each analog card has 8 channels and each channel can offer analog voltage ranging from -10 V to +10 V. The signals can be transmitted at a frequency of 250 kHz, meaning the difference between two signals is 4 μs. The digital card is mainly used for switching on/off the laser beams, magnetic fields, or trigger signals. The analog card is mainly used for changing the detuning and power of the lasers and changing the magnetic fields. All the cards used in our computer control system are shown in the appendix A. The software of the computer control system is briefly discussed in the appendix B.

3.7 Conclusion

In this chapter, we presented the relevant energy level diagram of Rubidium atoms at 5S → 5P (IR transition) and 5S → 6P (blue transition). Following this, we provided a concise insight into our laser system and explained the basic principle behind the spectroscopy techniques used for the frequency stabilization of the lasers. We discussed the shift in absolute frequency of the lasers due to the AOM in the path of the pump and/ or probe beam and how to choose the correct AOM frequency for addressing the correct transition of the Rb atom in the MOT chamber. Additionally, we also briefly discuss the MOT chamber. Furthermore, we presented the important formula and techniques associated with the absorption imaging technique to characterize the atomic cloud in MOT. Finally, we concluded this chapter with a brief overview of our computer control system.

* * *

Chapter 4

Direct Spectroscopy of Rubidium at 420 nm

Contents

[1] The 5S→6P transition in Rubidium (Rb) at 420 nm offers the advantage of a narrower linewidth and diverse applications in quantum technologies. However, the direct spectroscopy at this transition is challenging due to its weak transition strength. In this chapter, we have discussed the saturated absorption spectroscopy (SAS) of Rb using the narrow-line transition at 420 nm. We have studied the effect of the temperature of the Rb cell, control beam power, and beam size on the SAS dip heights and their linewidths. Additionally, our study offers a comprehensive examination, encompassing all eight error signals of Rb for the 5S→6P transition at 420 nm and 421 nm. These findings contribute valuable insights to the field of laser frequency stabilization of Rb at blue transition and can be useful in quantum technologies based on this transition.

4.1 Introduction

In the intricate landscape of precision measurements and laser technologies, spectroscopy holds a pivotal role, particularly in the domain of laser frequency stabiliza-

---

[1] This chapter is a slightly modified version of the journal article, titled "**Direct spectroscopy of Rubidium using a narrow-line transition at 420 nm**" by **Rajnandan Choudhury Das**, Samir Khan, Thilagaraj Ravi, and Kanhaiya Pandey, published in the journal **The European Physical Journal D** in 2024 [2].

tion [6, 119]. This precise control of laser frequencies is a key factor in a diverse array of applications, ranging from understanding fundamental physics to the development of cutting-edge technologies such as atomic sensors, quantum computers, quantum simulators, and atomic clocks. Among the various elements explored in this pursuit, Rubidium (Rb) has been a focal point of investigation. The well-established 5S→5P transitions at 780 nm and 795 nm have long dominated the spectroscopic landscape [126, 127].

The 5S→6P transition at the blue wavelength of 420 nm has received less attention, despite its manifold advantages (as discussed in Chapter 1), notably a narrower linewidth ($2\pi\times1.4$ MHz) compared to conventional infrared transitions ($2\pi\times6$ MHz). Despite its potential, a comprehensive understanding of the Rubidium spectrum at the blue transition has been surprisingly limited.

Traditionally, stabilizing the laser frequency at 420 nm involves double resonance spectroscopy [1] or saturated absorption spectroscopy (SAS) [82]. In double resonance spectroscopy, a V system is formed with a 780 nm probe and 420 nm control and electromagnetically induced transparency (EIT) and optical pumping methods are used [76]. However, this approach comes with complexities. The stability of the 420 nm signal depends on the stability of the 780 nm laser frequency, making it prone to noise and destabilization. Changes in the 780 nm laser frequency impact the 420 nm spectrum, adding complexities to experimental setups. Additionally, its absorption dip has large linewidth (typically $> 2\pi\times6$ MHz) due to the Doppler shift mismatch between the 780 nm and 420 nm lasers [76, 77]. Moreover, it is highly sensitive to the angle between the 780 nm and 420 nm laser beams [77].

On the other hand, SAS avoids the challenges linked with double resonance spectroscopy. While SAS is a widely employed technique [119, 128, 129, 130], applying it to narrow transitions poses challenges due to the weaker transition strengths compared to broader transitions. Elevating the vapor cell temperature to $50-100$ °C enhances the signal-to-noise ratio but introduces the possibility of coating on the vapor cell window, necessitating meticulous considerations in experimental design and execution. SAS on Cs at narrow transitions has been extensively studied [131, 132, 133, 134, 135]. For SAS on Rb at 420 nm, the use of blue color-sensitive photodetectors is essential and is now widely accessible. Glaser et al. have conducted precise measurements of absolute transition frequencies at 420 nm and 421 nm, reporting all the eight Rb spectra [136]. While various groups have made partial contributions to the study of the 5S→6P spectrum of Rb [137, 138, 139], a comprehensive investigation into the behavior of Rb spectra at the blue transition concerning experimental parameters is still lacking. This work addresses this gap by exploring the effects of temperature of the vapor cell, control beam power, and beam size on the SAS signal. Additionally, we present all eight error signals of Rb corresponding to the 5S→6P transition at 420 nm and 421 nm, providing a thorough analysis of this atomic transition.

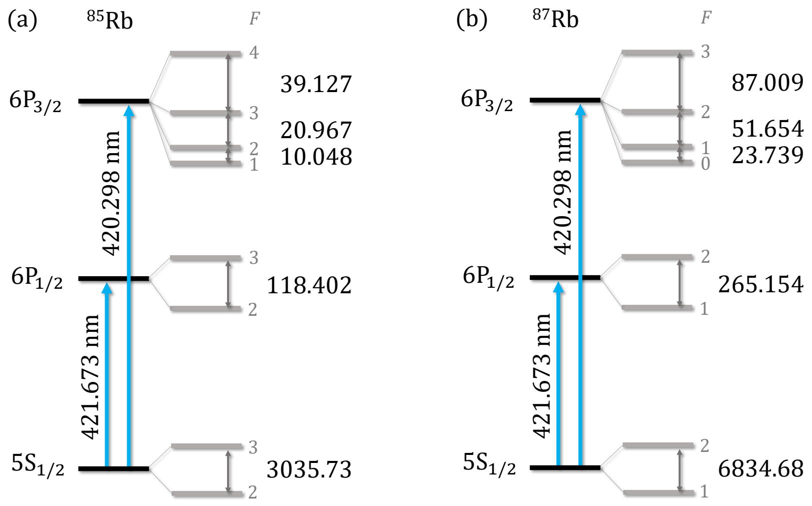

Figure 4.1: The relevant energy level diagram and hyperfine splitting (in MHz) for the $5S_{1/2}$ and 6P states of (a) ^{85}Rb and (b) ^{87}Rb.

4.2 Experimental Set-up

The experimental set-up comprises one commercially available external cavity diode laser (ECDL) from Toptica Photonics with model no. DL pro HP. It has a coarse tuning range of 420 - 423 nm and a typical linewidth of < 200 kHz. It has an integrated optical isolator to protect the laser diode from the back reflections from the other optical elements. The total available output power is 70 mW, and the output beam diameter is 3 mm × 4 mm. In the first half of the experiment, the wavelength is tuned to 420.298 nm to observe the D_2 line of the $5S_{1/2} \rightarrow 6P_{3/2}$ Rb spectrum and in the next half, it is tuned to 421.673 nm to observe the D_1 line of the $5S_{1/2} \rightarrow 6P_{1/2}$ spectrum. The relevant energy level diagram and hyperfine splitting (in MHz) for the $5S_{1/2}$ and 6P states of ^{85}Rb and ^{87}Rb are shown in Fig. 4.1. A leak beam from the blue laser is sent to a wavelength meter (make: Highfinesse GmbH, model: WS7-60) to monitor the single-mode operation and the wavelength of the blue laser.

Fig. 4.2(a) depicts the schematics of the experimental set-up for the saturated absorption spectroscopy (SAS) of the ^{87}Rb atom at blue transition. It consists of a rubidium vapor cell of length 100 mm and diameter 25 mm. The cell is wrapped with a thick layer of aluminum foil and placed inside a 150 mm long hollow cylindrical oven made of brass with an inner diameter of 27 mm and an outer diameter of 40 mm. Various dimensions and the cross-sectional views of the oven are shown in Fig. 4.3. Two hollow circular brass plates of the same inner and outer diameter are attached to both ends of the oven. Two quartz plates are attached on both ends of the oven to block the circular aperture and thermally isolate the vapor cell from the environment to avoid coating on the windows without limiting the optical access. The oven is wrapped with heating tape and another thick layer of aluminum foils. Current is passed through the heating tape using a variac to increase the oven's temperature. The temperature of the vapor cell is monitored using three thermocouples attached to its surface.

The blue laser is divided into two parts using the $\lambda/2$ wave-plate (H_1) and polarizing beam splitter (PBS_1), as shown in Fig. 4.2(b). The reflected beam from the PBS_1 is used for other experiments (not used in this work). The transmitted beam is used for the SAS and is divided into two beams using H_2 and PBS_2. The transmitted beam from PBS_2 is used as a probe beam. It is sent through the Rb vapor cell and is detected on a UV-enhanced Si Variable-Gain Avalanche photo-detector of bandwidth DC - 400 MHz (make: Thorlabs, model: APD430A2/M). The reflected beam from PBS_2 is sent through H_3 and PBS_3. The transmitted beam from PBS_3 is upshifted by $2\pi \times 2 \times 46.75$ MHz using an AOM in a double pass configuration. Polarization of the beam is rotated by 90^0 by the $\lambda/4$ wave-plate (Q) and thus gets reflected beam from PBS_3. It is used as a control beam. It is mixed with the probe beam on the PBS placed in front of the photo-detector and is sent to the vapor cell with counter-propagating to the probe beam. The polarization of the probe and control beam are orthogonal to each other. The power of the control beam is varied using H_3 and the PBS.

The laser frequency is tuned near the resonance and is scanned using piezo to find the SAS signal. It is observed and recorded on a digital storage oscilloscope of bandwidth 100 MHz. While the basic experimental schematics, as shown in Fig. 4.2(a), are sufficient for the detailed investigation of the behavior of the Rb spectra at the blue transition with experimental parameters, the additional AOM on the control laser beam path, as depicted in Fig. 4.2(b), is necessary to generate the error signal for frequency stabilization of the blue laser. To get the error signal, the rf frequency to the AOM is modulated at $2\pi \times 10$ kHz. The modulation is turned off while studying the SAS dip height and linewidth with different parameters.

Implementing an additional AOM exclusively on the control beam path distinguishes this technique from the conventional SAS method, where both the probe and control beams are equally up-shifted or down-shifted. This modification results in an improved signal-to-noise ratio for the error signal due to the absence of modulation in the probe beam. Additionally, careful attention is paid to the absolute laser frequencies. Let ν_0, ν_L, ν_c, and ν_p represent the resonant frequency, laser frequency, control beam frequency, and probe beam frequency, respectively. In our experimental setup, $\nu_p = \nu_L$ and $\nu_c = \nu_L + 2 \times 46.75$ MHz. Furthermore, considering the Doppler shift δ for moving atoms, we have $\nu_p = \nu_0 - \delta$ and $\nu_c = \nu_0 + \delta$. Solving these equations yields $\nu_L = \nu_0 - 46.75$ MHz. This implies that if only the control beam is upshifted by a frequency of $2\delta_0$, then the measured spectrum is down-shifted by δ_0. This consideration is crucial when employing this method in other experiments such as producing laser-cooled atoms [3, 4].

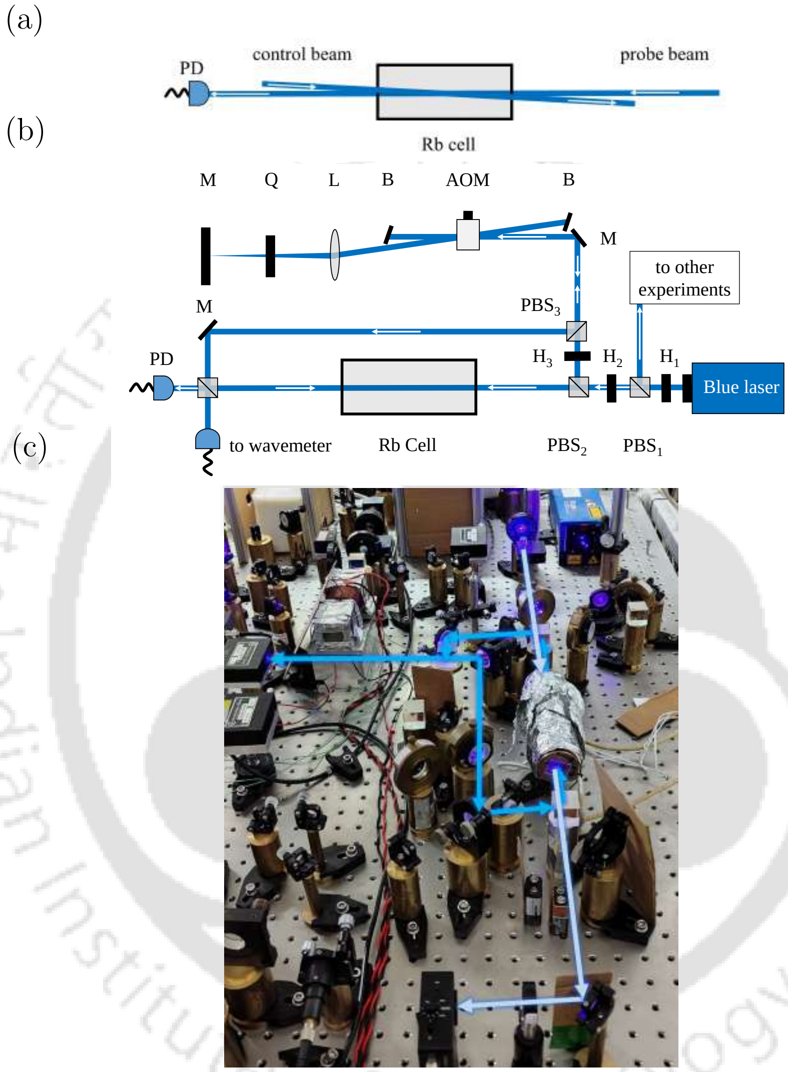

Figure 4.2: Saturated absorption spectroscopy set-up for the 420 nm laser. (a) Basic set-up, (b) Detailed. Figure abbreviations: AOM: acousto-optical modulator, B: beam blocker, H_1, H_2, H_3: $\lambda/2$ wave-plates, L: lens, M: mirrror, PBS_1, PBS_2, PBS_3: polarizing beam splitter, PD: photo-detector, Q: $\lambda/4$ wave-plate. (c) Image of the blue spectroscopy set-up

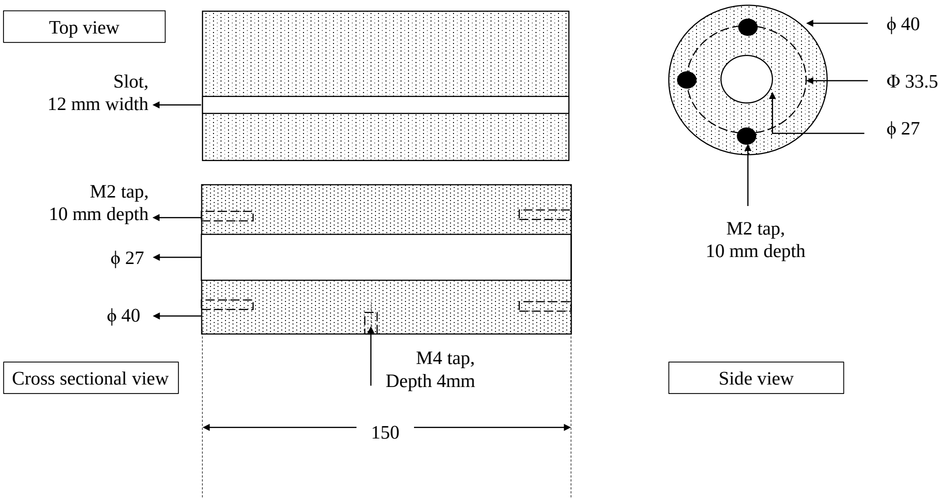

Figure 4.3: Dimensions of the the oven designed. All the dimensions are in mm unless it is specified.

4.3 Results and Discussion

In the absence of the control beam, atoms get excited by absorbing the probe beam, resulting in a Doppler-broadened Spectra. In the presence of the control beam, the atoms get excited, absorbing the control beam. Thus, there is a reduction in the probe absorption, resulting in several dips in Doppler-broadened spectra. These dips correspond to the hyperfine transitions of the Rb atoms and their cross-over peaks. Since the 5S→6P is an open transition, the hyperfine pumping is a factor in addition to the saturated absorption [120].

Initially, the blue laser is tuned to the $5S_{1/2}$, F$= 2 \rightarrow 6P_{3/2}$ transition of ^{87}Rb at 420 nm. It is scanned using a piezo to obtain all three real absorption peaks and three crossover peaks. A typical SAS signal at 80 ^{0}C is shown in Fig. 4.4(a). The 6 peaks corresponding to the transition from the lower ground state of ^{87}Rb i.e., $5S_{1/2}$ (F $= 2$) to the excited state, $6P_{3/2}$ (F $= X$) are identified within the Doppler envelope, where X = 1, (1,2), 2, (1,3), (2,3) and 3 from left to right. Here, the F $= (m, n)$ peak corresponds to the crossover resonance peak resulting from the F $= m$ and F $= n$ peaks. These crossover peaks occur when the laser frequency is equal to the sum of half of the two excited state frequencies. Both the control and probe beams interact with the same group of atoms, resulting in a dip halfway between two Lamb dips. The x-axis is scaled in such a way that the separation between the F$= (2, 3)$ and F$= 3$ peaks becomes 43.5 MHz [136].

Next, we focus on the two relatively larger peaks, i.e. F $= (2, 3)$ and F $= 3$. We

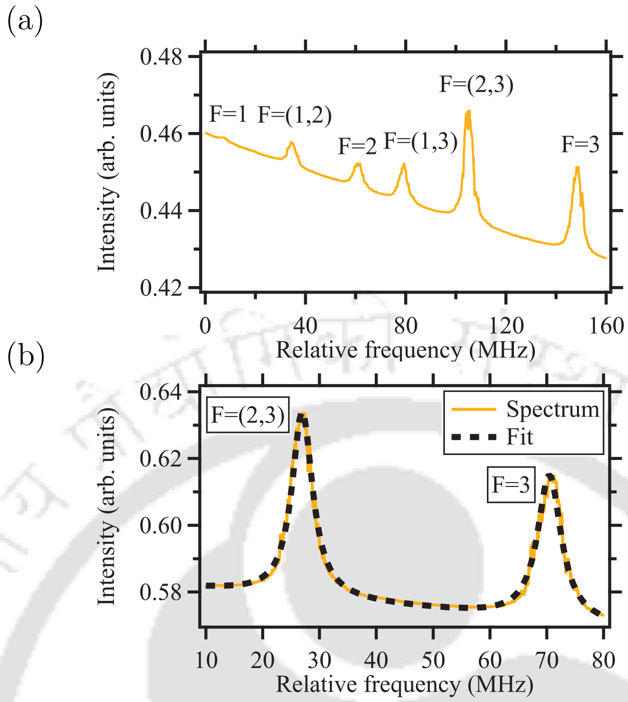

Figure 4.4: Saturated absorption spectroscopy spectrum for $5S_{1/2}$(F=2)→ $6P_{3/2}$ transition of ^{87}Rb at 420 nm. (a) Full spectrum. The peaks correspond to F=1, (1,2), (2), (1,3), (2,3) and 3, from left to right. (b) Spectrum with $F = (2,3)$ cross-over and $F = 3$ peaks. The orange line represents the spectrum and the black dotted line represents the fit.

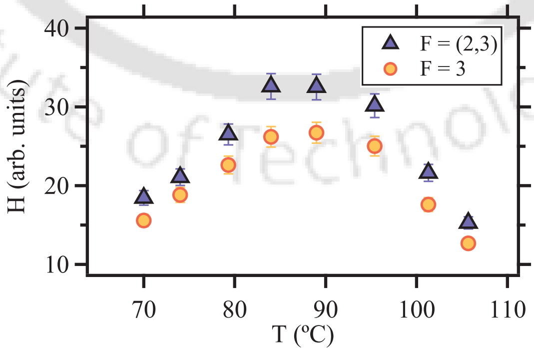

Figure 4.5: SAS dip height (H) vs the temperature of the Rb vapor cell (T). The purple triangle and orange circle correspond to the $F = (2,3)$ cross-over and $F = 3$ peaks, respectively.

decrease the scan amplitude to zoom into these two peaks. A typical SAS signal at 80 ^{0}C is shown in Fig. 4.4(b) (orange line). The x-axis is scaled as discussed above. To measure the SAS dip height and the linewidth of the F=(2,3) and F=3, the spectrum is fitted with the equation:

$$I = y_0 + m\nu + A_1/\left[1 + \left(\frac{2(\nu - \nu_0)}{\Gamma_1}\right)^2\right] + A_2/\left[1 + \left(\frac{2(\nu - \nu_0 - 43.5)}{\Gamma_2}\right)^2\right] \quad (4.1)$$

Here, I is the probe absorption, ν is the frequency of the 420 nm laser, ν_0 is the location of F=(2,3) peak, $y_0 + m\nu$ is the linear Doppler profile over which the F=(2,3) and the F= 3 peaks are appearing, $A_{1(2)}$ and $\Gamma_{1(2)}$ are the peak height and linewidth of the F=(2,3) (=3) peak respectively. The black dashed line in Fig.4.4(b) represents the fit. The linewidth of the F=(2,3) and the F= 3 peaks are $2\pi \times 4.57(3)$ MHz and $2\pi \times 4.46(4)$ MHz respectively.

We first study the effect of the temperature of the Rb vapor cell (T) on the SAS dip height (H) of the F=(2,3) and the F= 3 peaks (shown in Fig. 4.5). The power of the probe and control beams are 80 μW and 380 μW, respectively, and kept constant throughout the measurement. At room temperature, the spectrum could not be observed due to the weak transition strength of the blue transition. The temperature of the Rb vapor cell is slowly increased. We observe that the probe absorption increases as the temperature of the vapor cell is increased from 70 ^{0}C to 84 ^{0}C due to the increase in the number of atoms interacting with the beam inside the vapor cell [140]. It then reaches a maximum and decreases as the temperature is further increased from 84 ^{0}C to 106 ^{0}C due to increased collisions between the atoms [76, 141, 142]. Throughout the measurement, the height of the crossover peak, F $= (2, 3)$ is larger than that of the F $= 3$ peak. In the following portion of the experiment, the Rb vapor cell temperature is kept at 84 ^{0}C since this results in the best signal-to-noise ratio.

Next, we investigate the effect of the power of the control beam (P) on the SAS dip height (H) and linewidth (Γ) of the F=(2,3) and the F= 3 peaks (shown in Fig. 4.6 (a) and (b)). The probe power is kept constant at 80 μW. We observe that with an increase in the power of the control beam, SAS dip height and linewidth increase due to an increase in absorption and power broadening respectively. Due to the power broadening mechanism, the linewidth (Γ) increases with increasing power as per the equation: $\Gamma = \Gamma_0\sqrt{1 + I/I_s}$, where Γ_0 is a combination of natural broadening and the collisional broadening, I is the intensity of the control beam and I_s is the saturation intensity. We have done the least square fitting of the (linewidth)^2 vs power data as shown in Fig. 4.6 (b). By extrapolating to zero control power, we found that the minimum linewidth of F $= (2, 3)$ and F $= 3$ peaks are $2\pi \times 2.7$ MHz and $2\pi \times 2.8$ MHz respectively. This is around 2 times the natural linewidth of the 6P$_{3/2}$ state (natural linewidth $= 2\pi \times 1.4$ MHz). The difference in experimental measurement of the linewidth and the natural linewidth is due to residual broadening mechanisms.

Next, we study the effect of beam size on the peak height and its linewidth. We

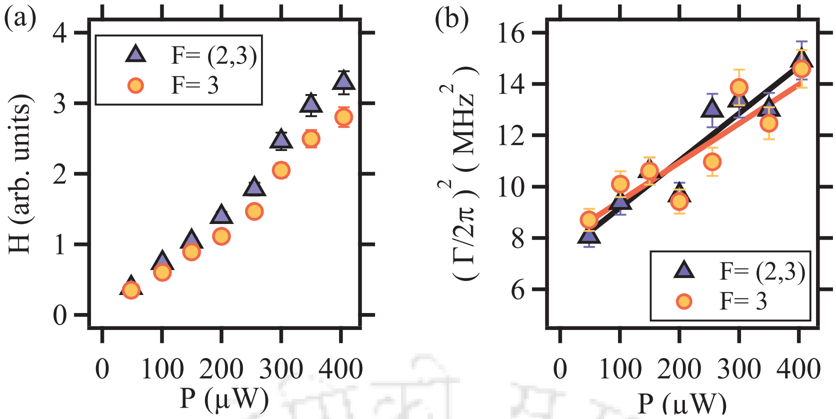

Figure 4.6: (a) SAS dip height (H), and (b) square of the linewidth ($[\Gamma/2\pi]^2$) of the corresponding peaks vs the power of the control laser (P). The purple triangle and orange circle correspond to the $F = (2,3)$ cross-over and $F = 3$ peaks, respectively.

increase the size of the beams by 2 times with the help of a combination of two plano-convex lenses of f=25 mm and f=50 mm. We increase the power of the control and probe beam by 4 times to keep the same ratio of the intensities of the control and probe beam. We observe similar behavior (as in Fig. 4.6). However for the same control to probe beam intensity ratio, the peak height increases by 2 times with the increased beam size. This is due to an increase in the number of atoms interacting with the blue beam. We also observe that the minimum linewidth of the F= (2,3) and F= 3 peaks are $2\pi \times 4.4$ MHz and $2\pi \times 4.2$ MHz, which is around 1.5 times more than the linewidth measured with 2x smaller beam size.

We extend this study to obtain the error signals by modulating the rf frequency of the AOM at 10 kHz. The error signals corresponding to the $5S_{1/2} \rightarrow 6P_{1/2}$ transition at 421 nm are shown in the first two rows of Fig. 4.7. Graphs (a) and (d) refer to the error signal of ^{87}Rb corresponding to the upper ground state (F = 2) and lower ground state (F = 1), respectively. Graphs (b) and (c) refer to the error signal of ^{85}Rb corresponding to the upper ground state (F = 3) and lower ground state (F = 2), respectively. The error signals corresponding to the $5S_{1/2} \rightarrow 6P_{3/2}$ transition at 420 nm are shown in the last two rows of Fig. 4.7. Graphs (e) and (h) refer to the error signal of ^{87}Rb corresponding to the upper ground state (F = 2) and lower ground state (F = 1), respectively. Graphs (f) and (g) refer to the error signal of ^{85}Rb corresponding to the upper ground state (F = 3) and lower ground state (F = 2), respectively. The error signals are well separated, except in (g), where they are slightly distorted due to closely spaced energy levels (31 MHz spread). All the error signals are shown in increasing order of frequency.

The power of the probe beam and control beam and the alignments are kept unchanged while recording all eight error signals. Thus, a rough comparison of the transition strength of the different peaks can be done. In contrast to the work by Glaser et. al [136], we observe that in Fig. 4.7(a), (b), and (d), the amplitude corresponding to the upper excited state is noticeably larger than that corresponding

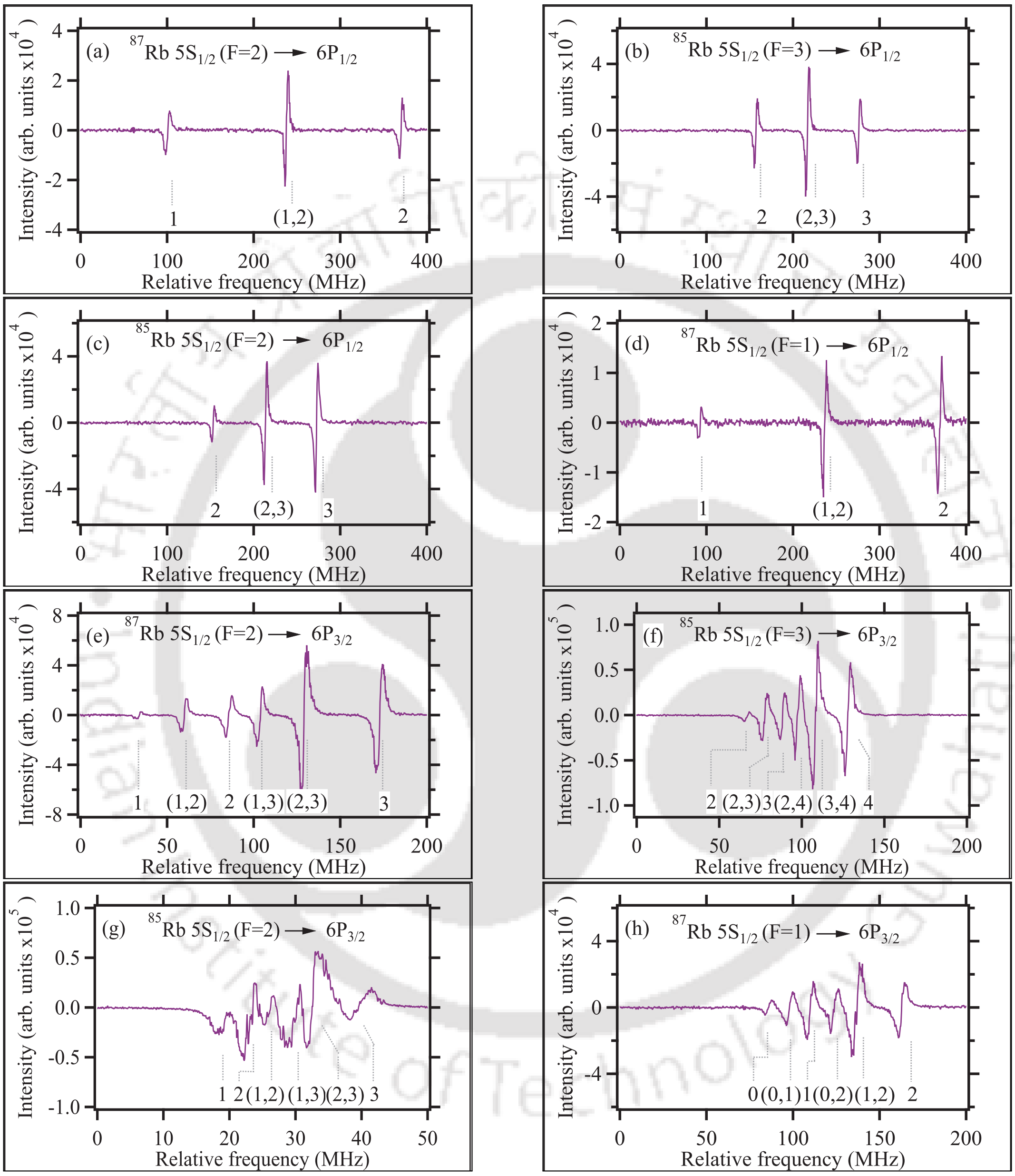

Figure 4.7: Recorded error signal corresponding to the 5S$_{1/2}$ → 6P$_{1/2(3/2)}$ transition at 421 (420) nm.

to the lower excited state. We find the ratios of the amplitude of the upper excited state to the lower excited state in (a)-(d), which are 1.4, 0.9, 3.8, and 4.4 respectively. These values are roughly equal to the theoretical values of the transition strength of the corresponding transitions (1, 0.8, 3.5, and 5 respectively) [6].

4.4 Conclusions

In summary, our study delves into saturated absorption spectroscopy (SAS) of Rubidium using a narrow-line transition at 420 nm. We systematically examined the effect of temperature of the Rb cell, control beam power, and beam size on SAS dip heights and linewidths. Achieving optimal signal-to-noise ratio at a Rb cell temperature of 84 ^{0}C, we obtained minimum linewidths of $2\pi \times 2.7$ MHz and $2\pi \times 2.8$ MHz for the $5S_{1/2}$, F = 2 → $6P_{3/2}$ transitions with F = (2,3) and F = 3, respectively. Notably, doubling the beam size could enhance the signal-to-noise ratio twofold, albeit with a 1.5 times increase in spectrum linewidth. Furthermore, we presented all eight error signals for ^{85}Rb and ^{87}Rb corresponding to the 5S → 6P transition at 420 nm and 421 nm. These findings significantly contribute to the foundational knowledge of SAS at the 420 nm transition in Rb, advancing laser frequency stabilization, and are used for producing laser-cooled Rb atoms at blue transition [3, 4]. The insights gained from this study hold practical implications for applications in quantum technologies, particularly those based on the blue atomic transition of Rb.

* * *

Chapter 5

The Blue Magneto-optical Trap

Contents

[1] Magneto-optical trap (MOT) at narrow transition offers lower temperature and hence is the key for producing high phase density atomic cloud and subsequently quantum degeneracy with a large number of atoms for many elements. In this chapter, we describe the loading of ^{87}Rb atoms in the MOT using a narrow open transition ($5S_{1/2} \rightarrow 6P_{3/2}$) at 420 nm (i.e. blue MOT) from the routinely implemented MOT using a broad cyclic transition ($5S_{1/2} \rightarrow 5P_{3/2}$) at 780 nm (i.e. IR MOT). Using the four times narrower transition, we have trapped around 10^8 atoms in the MOT with a typical temperature of around 54 μK. We have also studied the behavior of the blue MOT with various parameters such as hold time, detuning, and power of trapping and repumper beams.

5.1 Introduction

Realizing a lower temperature in a magneto-optical trap (MOT) using laser cooling technique [6, 8, 9, 10] is the key step for atomic-based quantum technologies. The theoretical limit to the lowest achievable temperature using the Doppler cooling

---

[1] This chapter is a slightly modified version of the journal article, titled "**Narrow-line cooling of ^{87}Rb using $5S_{1/2} \rightarrow 6P_{3/2}$ open transition at 420 nm**" by **Rajnandan Choudhury Das**, Dangka Shylla, Arkapravo Bera, and Kanhaiya Pandey published in the journal **Journal of Physics B: Atomic, Molecular and Optical Physics** in 2023 [1].

technique is the Doppler temperature. Thus to achieve lower temperature using this technique, it is always desirable to use a narrow-line cooling transition. However, the capture velocity in the MOT is proportional to the linewidth of the transition, which makes the broader linewidth transition favorable for capturing a higher number of atoms. Therefore, a two-stage MOT has been used for several elements to ensure efficient cooling in the MOT with a large number of atoms.

Alkali atoms are commonly loaded into the MOT using the D_2 transition ($\Gamma = 2\pi \times 6$ MHz), which corresponds to $T_D = 150$ μK. For Na, Rb, and Cs, the temperature can be lowered to a few tens of μK using polarization-gradient cooling (PGC). However, this sub-Doppler cooling mechanism demands switching off the magnetic field of the MOT for a few ms leading to the expansion of the cloud, which makes the cloud density smaller and inefficient for loading into the optical dipole trap (ODT) for evaporative cooling. Hence the MOT at narrow transition is quite useful for efficient transfer to the ODT. The levels with different principal quantum numbers can be utilized for narrow transition, as the electric dipole matrix element between them is small due to the lesser overlap of the wave functions, which causes the transition to be weak or narrow.

For Li and K, PGC is ineffective because of its closely spaced hyperfine levels, and to achieve sub-Doppler temperature, gray molasses (GM) on D_1 line [22, 25, 26, 27, 28] and D_2 line [29] have been used. But again, the GM cooling requires the MOT magnetic field to be turned off for a few milliseconds allowing the cloud to expand. The narrow line cooling has been implemented in Li [60, 61] and K [62]. Further, its advantage over gray molasses for loading the atoms into ODT has been demonstrated in Li [63]. Rb also possesses a similar level structure as that of Li and K. However, the demonstration of a reduction in the temperature of ^{87}Rb MOT using narrow-line transition is important because of its complex decay channels, especially when the repumper laser is at broad transition.

In this work, we characterize the loading of the blue MOT of ^{87}Rb atoms at 420 nm ($5S_{1/2}$, F= 2 $\rightarrow$ $6P_{3/2}$, F= 3) from the MOT at 780 nm ($5S_{1/2}$, F= 2 $\rightarrow$ $5P_{3/2}$, F= 3). For both the MOTs, we use only one repumper laser at 780 nm ($5S_{1/2}$, F= 1 $\rightarrow$ $5P_{3/2}$, F= 2) to pump the atoms back to the cooling cycle from the other ground-state hyperfine level ($5S_{1/2}$, F= 1).

5.2 Experimental Set-up

5.2.1 Laser system and spectroscopy

The relevant energy level diagram of ^{87}Rb, along with the hyperfine splittings and its complex decay paths of the $6P_{3/2}$ state, is shown in Fig. 5.1. Hyperfine splittings of $5S_{1/2}$, $5P_{3/2}$ and $6P_{3/2}$ are adopted from [143], and decay rates of various decay

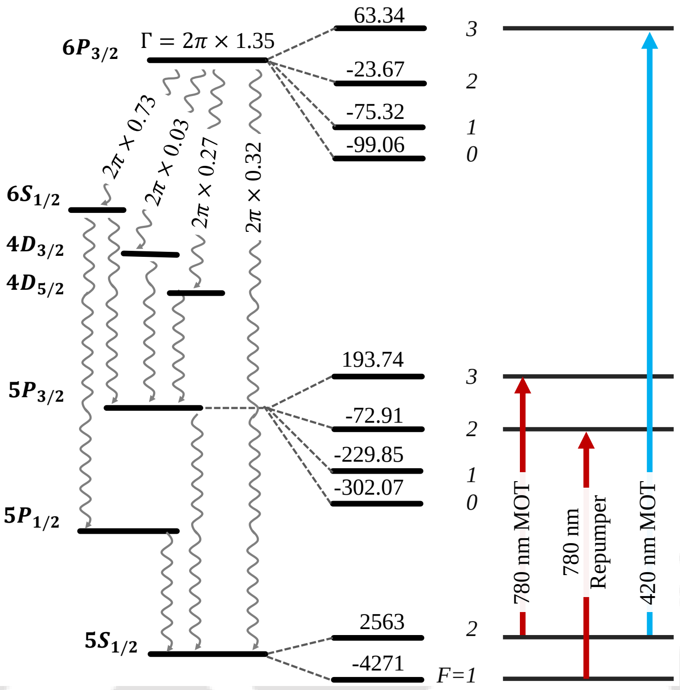

Figure 5.1: The relevant energy levels of ^{87}Rb with the hyperfine splittings and various decay paths of the $6P_{3/2}$ state. Decay rates, linewidth of the excited state, and the hyperfine splittings are shown in MHz units.

channels of the $6P_{3/2}$ state are calculated using the dipole matrix elements given in [144]. Calculated linewidth of $6P_{3/2}$ is $2\pi \times 1.35$ MHz and its corresponding lifetime is 118 ns [144] [2]. The $5S_{1/2}$, F=2 → $6P_{3/2}$, F=3 is an open transition with 4 decay channels (as shown in Fig. 5.1), unlike the commonly used $5S_{1/2}$, F=2 → $5P_{3/2}$, F=3 transition which is a closed (cyclic) transition.

The 780 nm (IR) lasers are generated from two separate home-assembled external cavity diode lasers (ECDL). Both the 780 nm trapping and repumper lasers use laser diodes (make: Thorlabs, model: L785H1 and L785P090 respectively). The output beam diameter is 2 mm ×3 mm for both the IR lasers and the output power available is 73 mW and 13 mW respectively. The 420 nm (blue) laser is generated from a commercially available ECDL (make: TOPTICA, model: DL PRO HP) with a typical linewidth < 200 kHz, output power 70 mW, and beam diameter 3 mm ×4 mm.

The 780 nm MOT laser is divided into three parts. The first part is utilized for frequency stabilization using polarization spectroscopy technique [121] as shown in Fig. 5.2 (a). The Rb vapor cell is heated up to 50 °C inside an oven using two Peltier coolers to improve the signal-to-noise ratio of the absorption spectrum. Peltier coolers are placed beneath the cell closer to its edge to avoid coating on the windows. The power of the control and probe beams are around 500 μW and 300 μW, respectively. The laser is locked to the $5S_{1/2}$, $F = 2 \rightarrow 5P_{3/2}$, $F = (2, 3)$

---

[2] The experimentally measured the lifetime is 120.7 ± 1.2 ns ($2\pi \times 1.318$ MHz) [145].

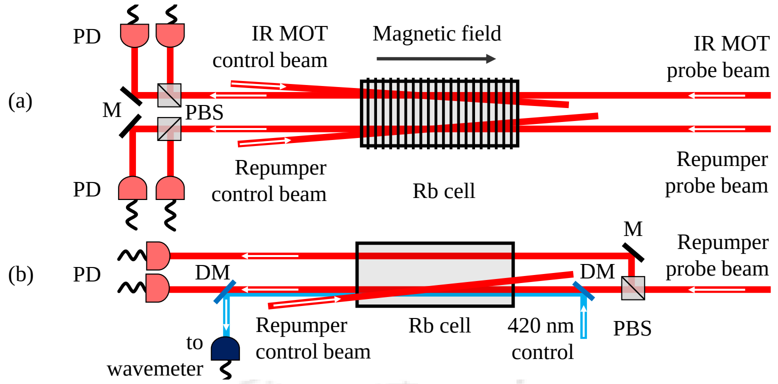

Figure 5.2: (a) Polarization spectroscopy scheme for 780 nm MOT and repumper lasers. (b) Double resonance spectroscopy scheme for 420 nm laser. Figure abbreviations: DM: dichroic mirror, M: mirror, PBS: polarizing beam splitter, PD: photo-detector. 780 nm and 420 nm beams are shown in red and blue color respectively.

crossover peak of the ^{87}Rb absorption spectrum. Its second part is sent through an acousto-optic modulator (AOM) at frequency $+2\pi \times 2 \times 66.5$ MHz in double-pass configuration and is used for imaging the MOT cloud after cleaning the spatial modes to a Gaussian. This AOM is used mainly for three purposes: firstly, for fast switching of the imaging beam; secondly, for scanning the imaging beam frequency to find the resonance of the MOT beam; and thirdly, to change the detuning of the imaging beam. The double-pass configuration is chosen as it prevents misalignment when the detuning of the imaging beam is changed. The third part is used as a trapping beam for the IR MOT after frequency shifting by $+2\pi \times 123.5$ MHz in single-pass configuration through AOM. This AOM is used for fast switching and power variation of the 780 nm trapping beam. Note that the terms control beam and probe beam are used only in the context of saturation absorption spectroscopy throughout this work, while for probing the MOT, we have used the term imaging beam.

The 780 nm repumper laser is also divided into three parts. The first part is sent to the same vapor cell where the spectroscopy of the 780 nm MOT laser is done. The separation between the IR MOT probe beam and repumper probe beam is around 7-8 mm. The repumper laser is frequency stabilized near the $5S_{1/2}$, $F = 1 \rightarrow 5P_{3/2}$, $F = 2$ transition again using polarization spectroscopy [121] as shown in Fig. 5.2 (a). The power of the control and probe beams are 2 mW and 25 μW, respectively. We play with the lock offset of the repumper laser, optimize the size of blue MOT cloud at the time of flight of 5 ms, and fix the lock point the same. At this stage, we were unaware of the fact that the repumper laser detuning plays a crucial role. However, in a later stage, we did a systematic study on the effect of the repumper laser on the temperature of the blue MOT which is discussed in chapter 7 of this thesis.

The second part of the repumper laser is sent to the MOT chamber after mixing it

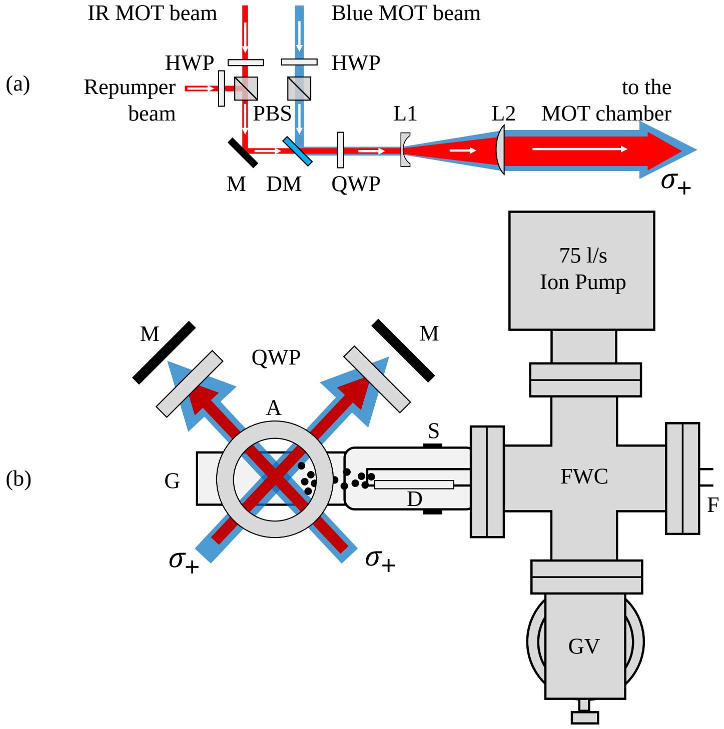

Figure 5.3: (a) Mixing scheme of the IR MOT, repumper, and blue MOT beams. (b) Top view of the MOT set-up. Figure abbreviations: A: anti-Helmholtz coil, D: Rb dispenser, DM: dichroic mirror, F: electric feedthrough, FWC: 4-way cross, G: glass chamber, GV: all metal gate valve, HWP: $\lambda/2$ wave-plate, L_1: plano-concave lens, L_2: plano-convex lens, M: mirror, PBS: polarizing beam splitter, S: Quartz to metal seal, QWP: dual $\lambda/4$ wave-plate, σ_+: co-propagating MOT beams in σ_+ configuration. 780 nm and 420 nm beams are shown in red and blue color respectively.

with the MOT beams. The third part is sent as a probe beam to another Rb vapor cell for double resonance spectroscopy of the 420 nm laser with a similar scheme as [122, 123].

The 420 nm laser is divided into two parts. The first part is sent to the second vapor cell through an AOM at frequency $-2\pi \times 2 \times 88.0$ MHz in double-pass configuration and is used as a control (with the power of around 800 μW) in the co-propagation configuration with 780 nm repumper laser which is stabilized at $5S_{1/2}$, F$= 1 \rightarrow 5P_{3/2}$, F$= 2$ transition. The IR repumper laser acts as a probe and is monitored at the photo-detector as shown in Fig. 5.2 (b). The power of this IR laser is around 100 μW. To remove the intensity noise of the laser and improve the signal-to-noise ratio of the double resonance spectrum; we use another reference IR beam that passes through the same cell and falls on another photo-detector. Both the photo-detectors are in A$-$B configuration. The error signal to lock the blue laser is generated by modulating the AOM at $2\pi \times 50$ kHz, and it is locked to the $5S_{1/2}$, $F = 2 \rightarrow 6P_{3/2}$, F = 2 transition. By changing the frequency of the AOM of blue laser spectroscopy, we change the detuning of the 420 nm trapping beam. Single-mode operation and the wavelength of the 420 nm laser are monitored using a wavelength meter (make: Highfinesse GmbH, model: WS7-60). The second part of the blue beam is frequency down-shifted by $2\pi \times 93.0$ MHz using an AOM in the single-pass configuration and is sent to the mixing scheme, where it is overlapped and co-propagated with the 780 nm MOT and repumper beams as shown in Fig. 5.3 (a) before sending it to the MOT chamber. This AOM is also used for fast switching and power variation of the 420 nm trapping beam.

5.2.2 MOT set-up

The 780 nm trapping, repumper, and 420 nm trapping beams are overlapped and co-propagated in the mixing scheme as shown in Fig. 5.3 (a). Three beams are derived in such a way that the polarizations of the trapping beams are identical in each of the three arms. Then the three beams are made circularly polarized using dual $\lambda/4$ wave-plates and are expanded individually by ten times using Galilean telescopes consisting of a pair of plano-concave and plano-convex lens of focal length, $f = -25$ mm and 250 mm respectively. The expanded beams are then sent to the MOT chamber and retro-reflected back with the combination of a mirror and a dual $\lambda/4$ wave-plate.

The schematics of the MOT set-up is shown in Fig. 5.3 (b). The MOT chamber used in this work is a rectangular glass chamber with the following dimensions: 7.5 cm $\times$ 2.5 cm $\times$ 2.5 cm. It is connected to an ion pump (pumping speed 75 l/s) through a 4-way cross. The pressure inside the vacuum chamber is around 10^{-10} mbar. Atomic rubidium vapor is dispensed into the chamber by passing 2.2 A current to a dispenser (AlfaSource Rubidium, model: AS-Rb-0090-2C-RbBi40) through the electric feedthrough at the other end of the 4-way cross. This dispenser current is kept fixed throughout the work except for the lifetime measurement, where the dispenser current is varied from 1.8 A to 2.4 A. The distance between the opening mouth of the dispenser to the MOT center is around 6 cm.

One pair of coils, each having an inner diameter of 7 cm, outer diameter of 13 cm, thickness of 3 cm, and 500 turns in an anti-Helmholtz configuration, is used to create a magnetic-field gradient of around 18 Gauss/cm at the center of the MOT chamber by passing 1 A electric current. Three pairs of shim coils surrounding the MOT chamber are also used (not shown in the schematics) to cancel the stray magnetic field. Fast switching of the magnetic field is done using an insulated-gate bipolar transistor (IGBT) based high current switch. The switching-off time of the coil is around 20 μs.

The time sequence along with the corresponding experimental parameters for loading the IR and blue MOT as well as the characterization of the MOT cloud is shown in

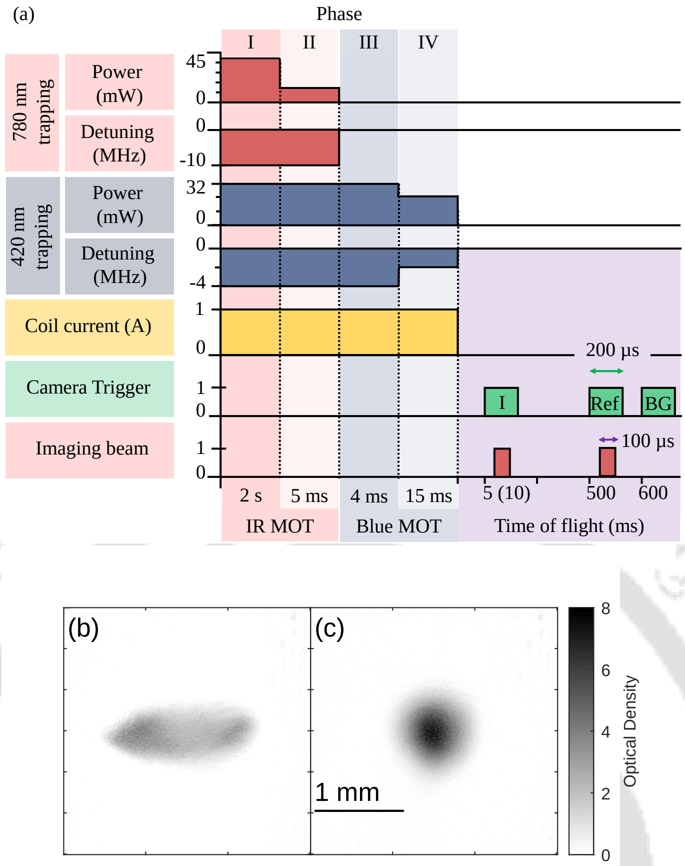

Figure 5.4: (a) Time sequence along with the corresponding experimental parameters for loading the IR and blue MOT and characterization of the MOT cloud. The coil current of 1 A corresponds to the magnetic field gradient of around 18 Gauss/cm. The ON (OFF) state of the camera trigger and 780 nm imaging beam is referred to as 1 (0). Three images captured at each cycle (i) image with MOT cloud, (ii) reference beam, and (iii) background are shown as I, Ref, and BG, respectively. The axes are not scaled. Absorption images of the (b) IR MOT and (c) blue MOT. The darkness denotes the optical density.

Fig. 5.4 (a). Various parameters of the MOT, such as the number of atoms, number density, temperature, and lifetime are determined by performing the absorption imaging of the MOT at $5S_{1/2}$, F$=$ 2 $\rightarrow$ $5P_{3/2}$, F$=$ 3 closed transition using the imaging beam derived from the 780 nm MOT laser as explained in the section 5.2.1. The power of the imaging beam is around 3 μW, and its diameter is 20 mm (peak intensity 0.002 mW/cm^2). The imaging beam is switched on only for 100 μs during imaging.

Images are captured on a CMOS camera (make: Thorlabs, model: CS135MUN) using an imaging system of de-magnification 0.3342. The exposure time of the camera is kept at 200 μs. Three images, (i) image with MOT cloud, (ii) Reference beam, and (iii) Background, are captured using the time sequence shown in Fig. 5.4

(a) to determine the size of the cloud and the number of atoms [11, 146]. Absorption images of the IR MOT and blue MOT at TOF 0.5 ms are shown in Fig. 5.4 (b) and (c) respectively. The same sequence is executed twice but with two different times of flight (TOF) at 5 ms and 10 ms to measure the temperature of the MOT. Various important phases of the time sequence are numbered as I, II, III, and IV in Fig. 5.4 (a). Note that the term hold time used in the thesis refers to the duration of phase IV during which the blue MOT is held at a lower power of the 420 nm laser.

5.3 Results

5.3.1 IR MOT

First, the atoms are loaded in an IR MOT using 780 nm trapping beams at 45 mW power and $-2\pi \times 10$ MHz detuning for 2 s indicated as phase I in Fig. 5.4 (a). To lower the temperature of the IR MOT, we lower the power of the 780 nm trapping beam to 10 mW for 5 ms in phase II. The parameters are set by conducting an experiment using a slightly different set-up of the 780 nm MOT laser in a master-slave configuration. In this setup, the master laser is locked to the atomic transition, and a part of the beam of this laser is up-shifted using an AOM in a double-pass configuration and used for seeding the slave laser. The slave laser remains seeded for the AOM frequency variation of around $2\pi \times 13$ MHz allowing us to vary the MOT laser detuning by $2\pi \times 26$ MHz. We observe that at the given parameters, $\sim 10^8$ atoms are trapped in the IR MOT at a typical temperature of around 400 μK. A typical absorption image of the IR MOT is shown in Fig. 5.4 (b). The loading time of the IR MOT is around 1.5 s. We have also measured the number of atoms in the IR MOT in the presence and the absence of the 420 nm laser beam and found that the 420 nm laser beam reduces the number of atoms in IR MOT (due to ionization) by only $\sim 10\%$.

5.3.2 Blue MOT

Atoms are then loaded into the blue MOT in phase III by turning off the IR MOT beam but keeping the blue MOT beam on for 4 ms at the maximum available power of the 420 nm trapping (32 mW), and repumper (10.2 mW) beams. The number of atoms transferred to the blue MOT is monitored for various detuning of the blue MOT laser in the loading phase at this fixed power and is shown in Fig. 5.5 (a). From the plot, it is found that the number of atoms transferred to the blue MOT increases as the detuning of the blue MOT laser is changed from $-2\pi \times 6$ MHz to $-2\pi \times 4$ MHz and then decreases as the detuning is changed towards the resonance. At $-2\pi \times 4$ MHz detuning of the 420 nm trapping beam, a maximum number of

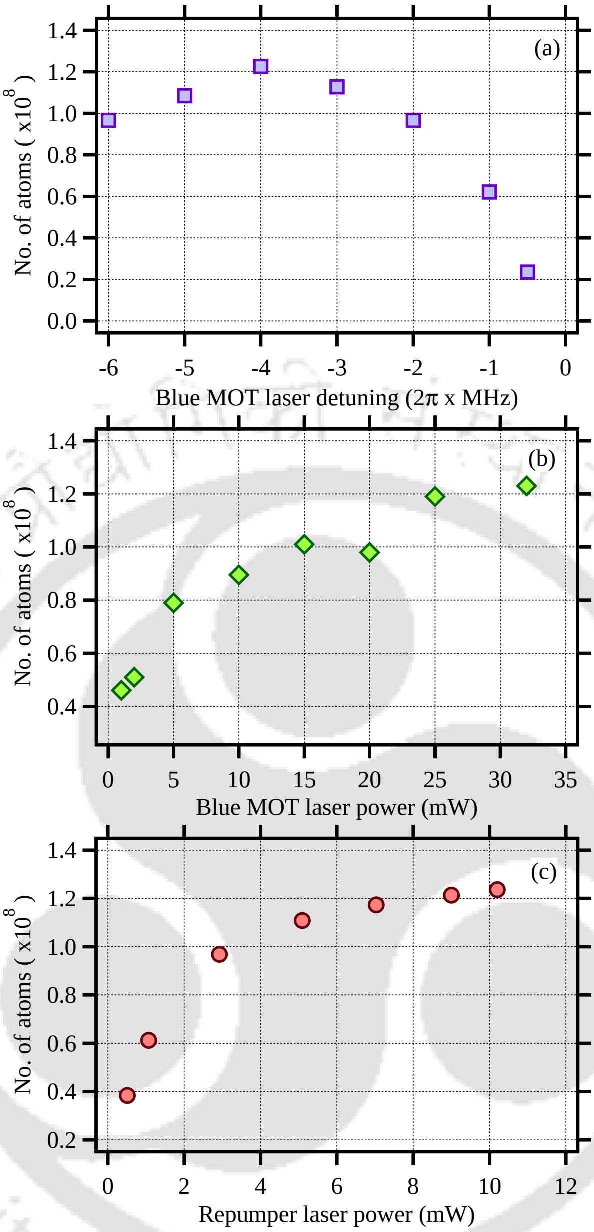

Figure 5.5: Number of atoms is shown as a function of (a) 420 nm MOT laser detuning in loading phase, (b) total 420 nm MOT laser power and (c) 780 nm repumper power. In (a) and (b) repumper laser is kept at its maximum available power, 10.2 mW. In (b) and (c) detuning of the 420 nm trapping beam in the loading phase is kept at $-2\pi \times 4$ MHz. In (a) and (c) power of the 420 nm MOT beam is kept at its maximum available power, 32 mW.

atoms (1.2×10^8) are transferred to the blue MOT. This detuning is hence used throughout the work for loading the blue MOT.

Next, to see the effect of the power of the blue MOT laser, we vary its power and monitor the number of atoms in the blue MOT. Detuning of the blue MOT laser is kept at $-2\pi \times 4$ MHz, and the power of the repumper beam is kept at its maximum.

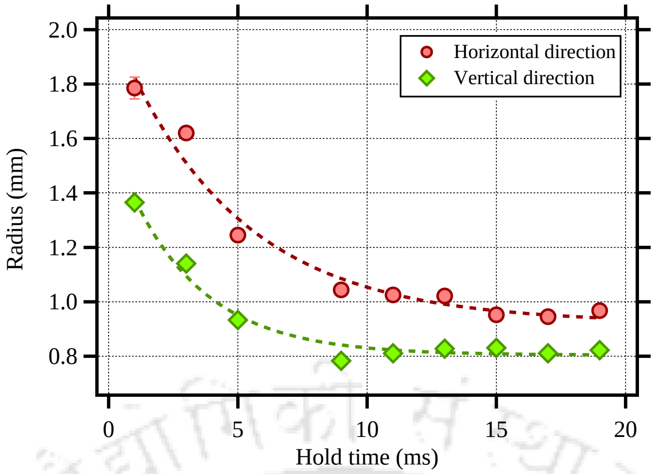

Figure 5.6: Radius of the cloud along horizontal (red circle) and vertical (green diamond) directions versus hold time in the blue MOT are shown for short hold times in the range [0:20 ms]. Exponential fits are shown as dashed lines, with 1/e time of 4.7 ms and 2.9 ms for horizontal and vertical direction respectively. Images were captured at 0.5 ms time of flight after release from the trap.

From Fig. 5.5 (b), it is clear that the number of atoms first increases with the increase in power of the blue MOT laser and then saturates at high power. It seems that the 32 mW power of the blue MOT laser is good enough for efficient transfer and is used throughout the work for loading the blue MOT.

To check the required power of the repumper laser, we again monitor the number of atoms in the blue MOT vs. the repumper laser power as shown in Fig. 5.5 (c). The power of the blue MOT laser is kept at its maximum, and its detuning is kept at $-2\pi \times 4$ MHz. We observe a similar pattern to that with the blue MOT laser power. The number of atoms first increases with an increase in repumper laser power and then saturates to a maximum at the high power of the repumper beam. We observe that 10.2 mW of repumper laser power is good enough to capture 1.2×10^8 atoms in the blue MOT.

After transferring the atoms from the IR MOT to the blue MOT, we lower the power of the blue MOT laser and vary the hold time and the detuning of the blue MOT laser in phase IV. A typical absorption image of the blue MOT is shown in Fig. 5.4 (c). For fixed power and detuning, we observe that the radius of the blue MOT decreases exponentially with the hold time (due to the overdamped harmonic motion of atoms in the MOT [6]), signifying the cooling of the MOT cloud. Fig. 5.6 shows its typical variation with the hold time at 10 mW power and $-2\pi \times 2$ MHz detuning. The radii data are fitted to the exponential decay function, and it is found that blue MOT size equilibrates with 1/e relaxation time of 4.7 ms and 2.9 ms for horizontal and vertical directions, respectively. It is also clear from the graph that the MOT cloud does not change its size typically after a 15 ms hold time; hence, the power of the blue laser is lowered for 15 ms in phase IV for further studying the effect of blue laser detuning on the number of atoms and temperature.

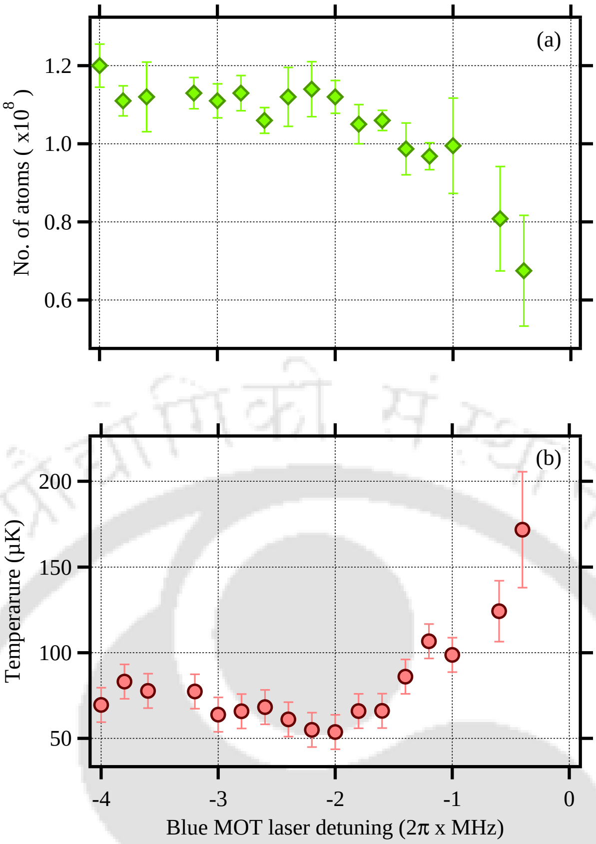

Figure 5.7: (a) No. of atoms, and (b) the Temperature of the blue MOT is shown as a function of the blue MOT laser detuning. The error bars in the measurement of the no. of atoms are $\sim 10\%$ and in the temperature measurement are $\sim 10\ \mu$K, for the blue laser detuning in the range $2\pi \times [-4 : -1\ \text{MHz}]$.

Next, we fix the hold time as 15 ms, vary the detuning of the blue MOT laser at 10 mW in phase IV, and study the behavior of the blue MOT by monitoring the number of atoms and temperature of the blue MOT. The number of atoms is measured by probing the MOT cloud using the time sequence shown in Fig. 5.4 at TOF 5 ms, and its variation with detuning is shown in Fig. 5.7 (a). We observe that the number of atoms remains almost constant ($\sim 1.1 \pm 0.1 \times 10^8$) in the range of -4 MHz to -2 MHz of the detuning of the blue MOT laser and then decreases as the detuning is changed towards zero.

The temperature of the cloud is determined by measuring the cloud size at two different TOFs using the same time sequence executed twice but with TOF 5 ms and 10 ms. Its variation with the detuning of the blue MOT laser is shown in Fig. 5.7 (b). We observe that at $-2\pi \times 2$ MHz, the temperature of the blue MOT is minimum, and it is around 54(10) μK. Temperature increases slowly to around 80 μK as the detuning is further increased towards $-2\pi \times 4$ MHz from the point of minimum, and it increases rapidly to around 170 μK as the detuning is changed towards resonance.

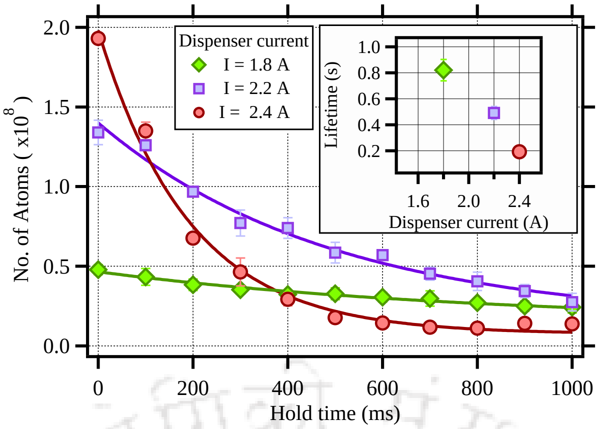

Figure 5.8: Lifetime of the blue MOT. No. of atoms is shown versus the hold time in the blue MOT at three dispenser currents: I = 1.8 A (green diamond), I = 2.2 A (violet square), and I = 2.4 A (red circle). The number of atoms vs hold time data are fit to exponential decays (solid lines) and the corresponding lifetimes are shown in the top inset. No. of atoms are probed at 0.5 ms TOF.

The number of atoms in the blue MOT at the minimum temperature of 54 μK is $\sim 1.1 \times 10^8$ and the corresponding number density is $\sim 1.0 \times 10^{10}$ cm^{-3}.

To determine the lifetime of the blue MOT, we monitor the number of atoms in the blue MOT at different hold times. We observe that the number of atoms decreases exponentially with hold time, as shown in Fig. 5.8. The lifetime of the blue MOT is determined by fitting the data (number of atoms vs hold time) with an exponential decay function. It is found that the lifetime of the blue MOT is around 0.5 s at a dispenser current of 2.2 A.

We have also studied the effect of the dispenser current on the number of atoms in the blue MOT and its lifetime. A trade-off between the maximum number of trapped atoms and the lifetime of the blue MOT is observed. It is found that with the increase in dispenser current, the lifetime of the MOT decreases as shown in Fig. 5.8 (inset), although the maximum number of atoms in the blue MOT increases. A maximum of 5×10^7 atoms can be trapped in the blue MOT with a maximum lifetime of 0.8 s at 1.8 A dispenser current. A four-fold increase in the number of trapped atoms to 2×10^8 is achieved by increasing the dispenser current to 2.4 A at the expense of a decrease in a lifetime by around 4 times to 0.2 s. With the increase in dispenser current, the number of background atoms increases increasing the collision between the trapped atoms and the background atoms and thus the lifetime of the MOT decreases.

5.4 Conclusions

In summary, we have demonstrated the narrow-line cooling of ^{87}Rb atoms in the MOT using the open transition, $5S_{1/2} \rightarrow 6P_{3/2}$ at 420 nm to trap around $1.1 \pm 0.1 \times 10^8$ atoms at typical temperature of 54(10) μK. As compared to the minimum temperature of the IR MOT (around 400 μK in our experimental setup), we have got around 8 times lower temperature in the blue MOT. Even though the $5S_{1/2} \rightarrow 6P_{3/2}$ is an open transition with a large branching ratio, we have achieved efficient cooling in the blue MOT using the repumper laser at 780 nm. Rb atoms loaded in MOT at blue transition will be quite useful for transferring the atoms in ODT and for evaporative cooling to achieve quantum degeneracy. The final temperature of the blue MOT may further be lowered by using a 420 nm repumper laser in place of the 780 nm repumper laser.

Chapter 6

Continuous Loading of Blue MOT

Contents

[1] In this chapter, we report continuous loading of ^{87}Rb atoms in a magneto-optical trap (MOT) at narrow linewidth, 420 nm $5S_{1/2}$, F= 2 → $6P_{3/2}$, F= 3 blue transition (blue MOT). Continuous loading of the blue MOT is achieved by superimposing the blue laser beam, inside a hollow core of infrared laser beam driving the broad $5S_{1/2}$, F= 2 → $5P_{3/2}$, F= 3 transition at 780 nm. We typically load $\sim 10^8$ atoms in the blue MOT in 2.5 s. We characterize the continuous loading of blue MOT with various parameters such as magnetic field gradient, detuning, power and diameter of blue MOT beam, and diameter of the hollow core (spot) inside the IR MOT beam. We observe that the blue laser beam should overfill the spot of the IR laser beam. This is because the blue laser cools the atoms to a lower temperature even in the presence of the broad IR laser i.e. in the overlapped region and hence helps in loading. To support the experimental result, we also present the theoretical framework for cooling atoms in the presence of two lasers driving two different transitions simultaneously. This method of continuous loading of the blue MOT can be useful to produce a continuous atomic beam of cold Rb atoms.

---

[1] This chapter is a slightly modified version of the preprint, titled "**Continuous loading of magneto-optical trap of Rb at narrow transition**" by **Rajnandan Choudhury Das**, Samir Khan, Thilagaraj R, and Kanhaiya Pandey, which is accepted for publication in the journal **Physical Review A** and is available in arXiv as [3].

6.1 Introduction

In the previous chapters, we have discussed that in order to achieve a higher number of atoms in MOT with low temperature, two-step MOTs are widely used for several elements such as Yb [51, 52], Sr [78, 147], Dy [53, 54, 148, 149], Er [55, 56, 57] and Cd [58] (where the ratio of the linewidth of broad to narrow transition is in orders of magnitude) and also in alkali elements [60, 61, 62] (where the ratio is $4-5$ times). In the previous chapter, we have demonstrated the two-step MOT of Rb at narrow transition. In the first step, atoms are loaded in MOT at a broad linewidth transition, and in the second step, atoms are transferred to the MOT at a narrow linewidth transition to achieve lower temperature, which means these two steps are separated in time. Instead of separating these two steps in time, one can also separate in space which results in the continuous loading of atoms in MOT and was the key process for producing continuous BEC of Sr [78]. Continuous loading of the atoms in MOT at narrow transition can enable us to generate a continuous beam of the cold atoms at lower temperatures which offers a great advantage for atomic-based quantum sensors as it eliminates dead time.

The continuous loading of the MOT at narrow transition pre-cooled by broad transition has been realized for certain elements Yb [51], Sr [78] and Dy [54]. In the case of Yb, continuous loading of MOT at narrow transition is superior in terms of the number of atoms and of course temperature [51, 79, 80]. Yb MOT at broader transition has less number of atoms (even in the presence of repumper lasers [81]) as compared to the narrow transition. The MOT for alkali atoms at narrow transitions in Li [60], K [62], Rb [1, 82] has been realized but continuous loading has not been reported yet.

We use core-shell MOT similar to the Yb [79] where a huge advantage was reported. In the scheme, a hole is created in the core of the laser beam driving the broad transition which is filled by the laser beam at a narrow transition. The relative dimension of the core and the filling beam is very important and depends upon the ratio of broad and narrow linewidth transition. In the case of Yb, the ratio of the linewidth of broad to narrow transition is around 150 and the core should be just filled as in the presence of the broad linewidth laser the weak transition laser (with intensity comparable to the saturation intensity) does not play a significant role in reducing the temperature. The case can be different in alkali atoms where the linewidths of the broad and narrow transitions are only $4-5$ times. In this case, the filling area should be bigger than the core area as in the overlapped region, the narrow transition linewidth plays a role in reducing the temperature even in the presence of the broad transition.

In this work, we present a method to load atoms continuously in the narrow-line MOT by superimposing the narrow-line beam inside the core of the broad transition beam. Using Rubidium atoms, we demonstrate the loading of 1.2×10^8 atoms continuously in the blue MOT at 420 nm using $5S_{1/2}$, F= $2 \rightarrow 6P_{3/2}$, F= 3 transition.

We study the behavior of the blue MOT with various parameters such as magnetic field gradient, detuning, power and diameter of blue MOT beam, and diameter of the spot inside the IR MOT beam.

The chapter is organized as follows. In section 6.2, we describe the experimental set-up. In section 6.3, we describe the theoretical model for the calculation of force, diffusion, and temperature in the presence of the two transitions at 780 nm and 420 nm. In section 6.4, we study the various effects due to magnetic-field gradient, detuning, power and diameter of the blue MOT laser, and diameter of the spot on the IR MOT laser. In section 6.5, we summarize our findings.

6.2 Experimental Set- up

The relevant energy level diagram and corresponding transitions utilized in this study are shown in Fig. 6.1. The laser system comprises one commercially (Toptica) available 420 nm (blue) external cavity diode laser (ECDL) and two home-assembled 780 nm (IR) ECDLs. The blue laser is divided into two parts: one for its frequency stabilization using saturation absorption spectroscopy (SAS) and the second for trapping the atoms in the blue MOT. Fig. 6.2 depicts the schematics of the SAS setup. The probe beam is passed through one Rb vapor cell and detected on a high-speed and blue color-sensitive photo-detector (make: Thorlabs, model: APD430A2/M). The vapor cell is kept inside an oven at 85 °C. The other part of the blue laser beam is sent through an AOM in a double-pass configuration. It is up-shifted by around $+2\pi \times 2 \times 49.75$ MHz and is sent through the cell as a control beam with counter-propagating to the probe beam. This central frequency is adjusted to vary the detuning (Δ_B) of the blue MOT beam. The AOM frequency is modulated at $2\pi \times 10$ kHz to generate the error signal. Note that the probe beam is not modulated and thus gives a better signal-to-noise ratio than when it is modulated. The laser is locked corresponding to the $5S_{1/2}$, F= 2 → $6P_{3/2}$, F= 3 peak. A portion of the leaked beam is used for monitoring the single-mode operation and the wavelength of the 420 nm laser using a wavelength meter (make: Highfinesse GmbH, model: WS7-60).

The second part of the blue beam is passed through another AOM at $+2\pi \times 46.75$ MHz, and its first-order beam is sent to the mixing scheme as shown in Fig. 6.3(a) after expanding it by ten times. This AOM is used for switching the blue beam on and off and varying its power. An iris is used for changing the diameter of the blue beam (ϕ_B).

Polarization spectroscopy is employed for the two IR laser's frequency stabilization, as described in [1]. The IR MOT laser is locked to $5S_{1/2}$, F= 2 → $5P_{3/2}$, F= $(2, 3)$ cross-over peak and IR repumper laser is locked to $5S_{1/2}$, F= 1 → $5P_{3/2}$, F= 1 peak. Other parts of the IR MOT and repumper lasers are sent through two different

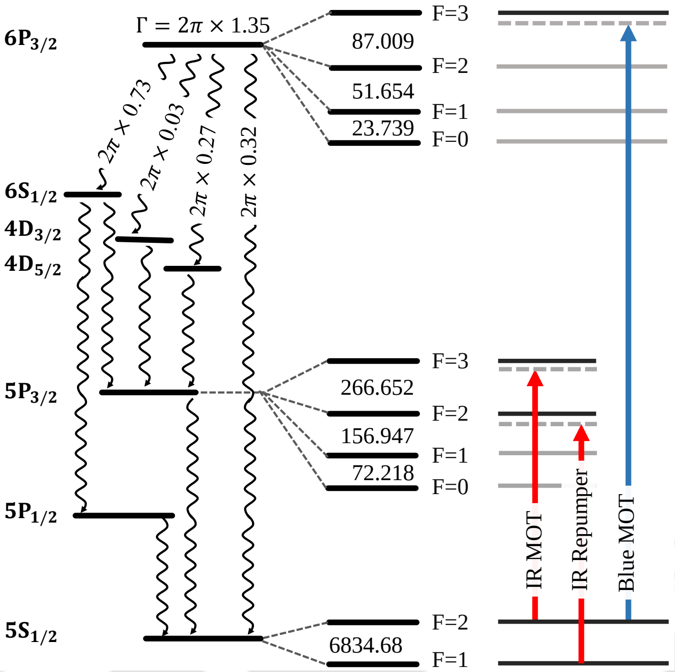

Figure 6.1: The relevant energy levels of ^{87}Rb with the hyperfine splitting and various decay paths of the $6P_{3/2}$ state. Decay rates, linewidth of the excited state, and the hyperfine splitting are shown in MHz unit [1].

AOMs at $+2\pi \times 123.5$ MHz and $+2\pi \times 150$ MHz, respectively to address the $5S_{1/2}$, F= 2 → $5P_{3/2}$, F= 3 and $5S_{1/2}$, F= 1 → $5P_{3/2}$, F= 2 transitions. The first-order diffracted beams are then expanded ten times individually and sent to the mixing scheme, as shown in Fig. 6.3(a).

On the path of the IR MOT beam, a circular mask (MA) is introduced so that a hollow core of diameter ϕ_{spot} can be created inside the IR MOT beam. IR beams are then mixed on a polarizing beam splitter (PBS) and made the same polarized using another PBS and a half-plate. The vertical polarized beam from the PBS is mixed with the vertical polarized blue MOT beam using a dichroic mirror and made co-propagated, as shown in Fig. 6.3(a). The other two arms of the MOT beams with the same polarization are generated from the horizontally polarized beams from the PBS using two half-wave plates, two PBS, and two dichroic mirrors (not shown in the schematics for simplification). All the beam's maximum diameter is limited to 16 mm due to the limitation set by the maximum diameter of the half wave-plates used in this experiment.

Three arms are then made circularly polarized using dual quarter wave-plates, sent to the rectangular glass MOT chamber, and retro-reflected back using a combination of dual quarter wave-plates and mirrors (as shown in Fig. 6.3(b)). The configuration of the MOT set-up is the same as in [1]. Atomic Rb vapors are introduced into the chamber by passing 2.15 A electric current to a dispenser (AlfaSource AS-Rb-0090-2C) inside the glass chamber.

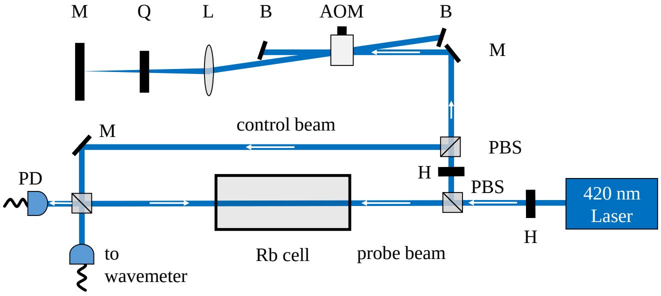

Figure 6.2: Saturated absorption spectroscopy (SAS) scheme for the 420 nm laser. Figure abbreviations: AOM: acousto-optical modulator, B: beam blocker, M: mirror, PBS: polarizing beam splitter, PD: photo-detector, H: $\lambda/2$ wave-plate, Q: $\lambda/4$ wave-plate, L: Lens.

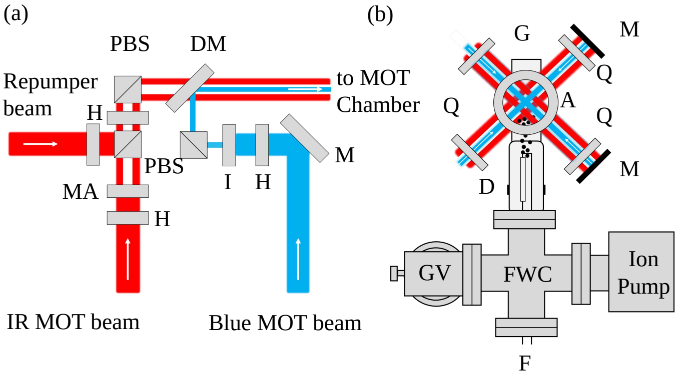

Figure 6.3: (a) Mixing scheme of the three lasers. (b) Top view of the MOT setup. Figure abbreviations: A: anti-Helmholtz coil, D: Rb dispenser, DM: dichroic mirror, F: electric feedthrough, FWC: 4-way cross, G: glass chamber, GV: all metal gate valve, H: $\lambda/2$ wave-plate, I: iris, M: mirror, MA: mask, PBS: polarizing beam splitter, Q: dual $\lambda/4$ wave-plate. 780 nm and 420 nm beams are shown in red and blue color respectively

The absorption imaging technique is used to capture the image of the atomic cloud on a CMOS camera (Thorlabs, CS135MUN) using an imaging beam. The imaging beam is $2\pi \times 5$ MHz red detuned from the $5S_{1/2}$, F= 2 $\rightarrow$ $5P_{3/2}$, F= 3 transition. It is generated using double-pass AOM and is coupled to a single-mode fiber. The camera's exposure time is 100 μs, and the imaging beam is turned on for 52 μs during the imaging cycle. The temperature of the cloud is determined from the time of flight method.

6.3 Theory

We have observed in the experiment (described in section 6.4) that the size of the blue MOT beam should be bigger than the size of the hollow core (spot) in the

IR MOT beam for loading a higher number of atoms. This implies that there is an overlapped region for the two lasers and hence both transitions are driven simultaneously in this region. In order to analyze the cooling mechanism in the presence of both transitions, we use the density matrix approach in one dimension. We consider that two (counter-propagating) laser beams are driving the transition $|1\rangle$ (5S$_{1/2}$, F=2) → $|2\rangle$ (5P$_{3/2}$, F=3) at 780 nm and two (counter-propagating) laser beams are driving the transition $|1\rangle$ (5S$_{1/2}$, F=2) → $|3\rangle$ (6P$_{3/2}$, F=3) at 420 nm.

The Hamiltonian (H) for the three-level system can be written as

$$\begin{aligned} H = & -\hbar\delta_{12}^{+}\,|2\rangle\langle 2| - \hbar\delta_{13}^{+}\,|3\rangle\langle 3| \\ & + \Bigg[\left\{\frac{\hbar\Omega_{12}^{+}}{2} + \frac{\hbar\Omega_{12}^{-}}{2} e^{i(\delta_{12}^{+}-\delta_{12}^{-})t}\right\}|1\rangle\langle 2| \\ & + \left\{\frac{\hbar\Omega_{13}^{+}}{2} + \frac{\hbar\Omega_{13}^{-}}{2} e^{i(\delta_{13}^{+}-\delta_{13}^{-})t}\right\}|1\rangle\langle 3| + h.c.\Bigg] \end{aligned} \tag{6.1}$$

Here $\delta_{12}^{+(-)}$ and $\delta_{13}^{+(-)}$ are the detuning of the 780 nm and 420 nm laser beams propagating in the positive (negative) direction, respectively. For the atoms moving in the positive direction with velocity v, the $\delta_{12}^{+} = \delta_{12} - k_{12}v$, $\delta_{13}^{+} = \delta_{13} - k_{13}v$, $\delta_{12}^{-} = \delta_{12} + k_{12}v$ and $\delta_{13}^{-} = \delta_{13} + k_{13}v$. Here, $k_{12} = 2\pi/780$ nm and $k_{13} = 2\pi/420$ nm and δ_{12} and δ_{13} are detuning of the 780 nm and 420 nm lasers for stationary atoms. $\Omega_{12}^{+} = \Omega_{12}^{-} = \Omega_{12}$ and $\Omega_{13}^{+} = \Omega_{13}^{-} = \Omega_{13}$ are the Rabi frequencies of the 780 nm and 420 nm lasers.

The atom-field interaction is described by writing the Liouville-von Neumann equation for the density matrix, [123]

$$\frac{d\rho}{dt} = -\frac{i}{\hbar}[H,\rho] + L(\rho) \tag{6.2}$$

where ρ is the density matrix and $L(\rho)$ accounts for the spontaneous decay. The equations of motion of the density matrix are obtained by solving the Eq. 6.1 and Eq. 6.2. Since the Hamiltonian has harmonically oscillating terms at two different frequencies, Floquet expansion for the density matrix elements is used as follows, (similar to [108, 123])

$$\rho_{ij}(t) = \sum_{m=-\infty}^{\infty}\sum_{n=-\infty}^{\infty} \rho_{ij}^{(m,n)}(t)e^{i(m\Delta_1+n\Delta_2)t} \tag{6.3}$$

where $\Delta_{1(2)} = -2k_{12(13)}v$. The Floquet expansion is truncated up to second order, substituted in the density matrix equations, coefficients of the same power in $(m\Delta_1, n\Delta_2)$ are compared to obtain the simultaneous differential equations and then numerically solved to find all the coefficients.

The absorption of 780 nm laser beam propagating in positive and negative directions are given by Im($\rho_{12}^{(0,0)}$) and Im($\rho_{12}^{(1,0)}$) respectively, similarly for the blue beams it is

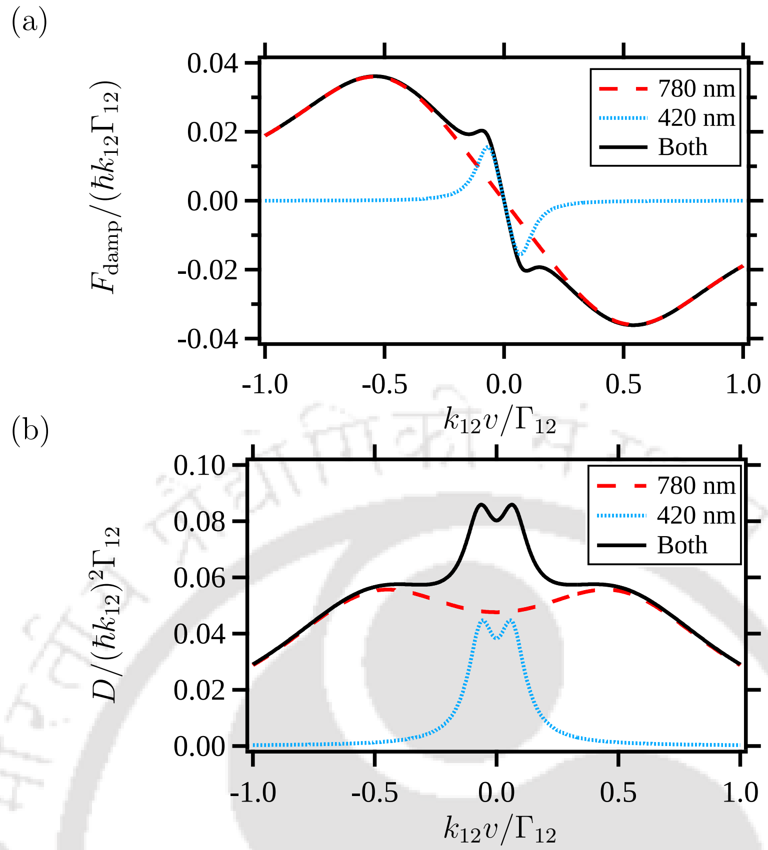

Figure 6.4: (a) Force and (b) Diffusion coefficient vs velocity plot. The Red dashed line, blue dashed line and black solid line correspond to the force (in (a)) and diffusion coefficient (in (b)) in the presence of only 780 nm laser, only 420 nm lasers, and both lasers respectively. k_{12} is the magnitude of the wave vector of the 780 nm laser and Γ_{12} is the linewidth of the IR transition. Parameters used: $\delta/\Gamma = -1/2$ and $I/I_s = 1/10$ for both the lasers.

given by $\mathrm{Im}(\rho_{13}^{(0,0)})$ and $\mathrm{Im}(\rho_{13}^{(0,1)})$. All other coefficients denote the wave mixing. Here $\mathrm{Im}\{.\}$ denotes the imaginary part. The damping force on the atoms in the presence of the two lasers can be given as

$$F_{\mathrm{damp}} = \hbar\big[k_{12}\Omega_{12}\ \mathrm{Im}(\rho_{12}^{(0,0)} - \rho_{12}^{(1,0)}) \\ + k_{13}\Omega_{13}\ \mathrm{Im}(\rho_{13}^{(0,0)} - \rho_{13}^{(0,1)})\big] \tag{6.4}$$

The force, $F_{\mathrm{damp}}/(\hbar k_{12}\Gamma_{12})$ vs velocity, $k_{12}v/\Gamma_{12}$ is plotted in Fig. 6.4(a). The parameters used for this plot are $\delta_{12}/\Gamma_{12} = \delta_{13}/\Gamma_{13} = -1/2$ and $I/I_s = 1/10$ for both the lasers. Here, $\Gamma_{12(13)}$ is the linewidth of the 780 (420) nm transition and I_s is the saturation intensity. The red dashed (blue dotted) line corresponds to the force in the presence of only 780 (420) nm laser. The black solid line represents the net force in the presence of both lasers. For very low velocity, $F_{\mathrm{damp}} = -\beta v$, where β is known as the damping coefficient. From Fig. 6.4(a), it is clear that $\beta_{420} > \beta_{780}$ and $\beta_{420} \approx \beta_{\mathrm{both}}$, where $\beta_{780(420)}$ is the β in presence of only 780 (420) nm laser and β_{both} is the β in presence of both the lasers. This implies that once the atoms are

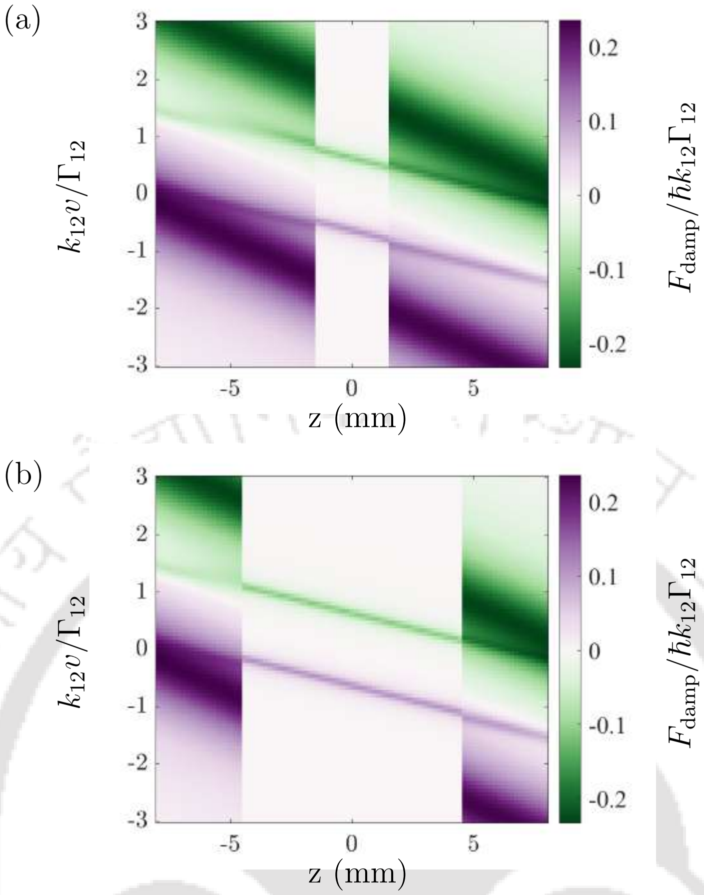

Figure 6.5: Two-dimensional color plot of force vs position and velocity for two spot sizes (a) 3 mm and (b) 9 mm at $\phi_B = 16$ mm, $\Omega_{12} = \Gamma_{12}/\sqrt{2}$, $\Omega_{13} = \Gamma_{13}/\sqrt{2}$, $\delta_{12} = -2\pi \times 10$ MHz, $\delta_{13} = -2\pi \times 7$ MHz. k_{12} is the magnitude of the wave vector of the 780 nm laser and Γ_{12} is the linewidth of the IR transition.

cooled by the IR laser in the outer region and enter into the overlapped region of the IR and blue laser, then the atoms are further cooled down dominantly by the blue laser.

The diffusion coefficient in the presence of both the driving lasers can be given as:

$$\begin{aligned} D = \hbar^2 \big[& k_{12}^2 \Omega_{12} \, \mathrm{Im}(\rho_{12}^{(0,0)} + \rho_{12}^{(1,0)}) \\ & + k_{13}^2 \Omega_{13} \, \mathrm{Im}(\rho_{13}^{(0,0)} + \rho_{13}^{(0,1)}) \big] \end{aligned} \tag{6.5}$$

The diffusion coefficient, $D/(\hbar k_{12})^2 \Gamma_{12}$ vs velocity, $k_{12}v/\Gamma_{12}$ plot is shown in Fig. 6.4(b) for the same parameters as in Fig. 6.4(a). Two-dimensional color plot of force vs position and velocity for two spot sizes 3 mm and 9 mm at $\phi_B = 16$ mm, $\Omega_{12} = \Gamma_{12}/\sqrt{2}$, $\Omega_{13} = \Gamma_{13}/\sqrt{2}$, $\delta_{12} = -2\pi \times 10$ MHz, $\delta_{13} = -2\pi \times 7$ MHz are shown in Fig. 6.5(a) and (b) respectively. The IR transition has a stronger damping force as compared to the blue transition. The larger spot size reduces the region/ area of the stronger damping force and hence reduces the number of atoms in the blue MOT.

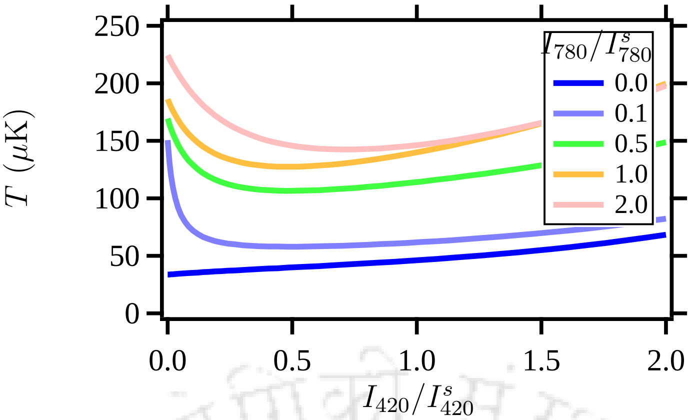

Figure 6.6: Temperature vs intensity of the 420 nm laser at various intensities of the 780 nm laser.

Then the effective temperature is found using the Einstein relation, $T = D(0)/\beta k_\mathrm{B}$, where $D(0)$ is the diffusion coefficient at zero velocity and k_B is Boltzmann constant [150]. The temperature vs intensity of the 420 nm laser (I_{420}) is plotted in Fig. 6.6 for various intensities of 780 nm laser (I_{780}) at $\delta_{12}/\Gamma_{12} = \delta_{13}/\Gamma_{13} = -1/2$. In the absence of the 780 nm laser (dark blue line at bottom), T decreases linearly with the decrease in I_{420} and reaches the Doppler temperature (T_D) corresponding to the blue transition, given by $\hbar\Gamma_{13}/2k_\mathrm{B} = 34$ μK. Note that T_D at 780 nm is ~ 150 μK. As the intensity of the IR laser increases in the absence of the blue laser, the T also increases. However, T decreases in the presence of the 420 nm laser, as shown by the light blue (dark grey) curve in Fig. 6.6. For fixed IR laser intensity, T initially decreases with an increase in I_{420}, reaches a minimum, and then increases with a further increase in I_{420}. We also observe experimentally that the temperature of the IR MOT decreases from ~ 1 mK (in the absence of the blue laser) to ~ 400 μK (in the presence of the blue laser at $\Delta_B = -2\pi \times 3$ MHz). Thus in the overlapped region, the laser driving the narrow linewidth transition further reduces the speed of the atoms (than the outer region) before it reaches the core region where only the laser driving the narrow linewidth transition is present. This suggests that the overlapped region in the broad and narrow linewidth transitions affects the continuous loading of the atoms in the narrow line MOT and eventually the number of atoms in the blue MOT.

Note that for low intensities (in comparison to saturation intensities) of 780 nm and 420 nm laser beams, the V-systems behave as two separate two levels systems ($|1\rangle \rightarrow |2\rangle$ and $|1\rangle \rightarrow |3\rangle$). The T for very low intensity of 780 nm and 420 nm is given as

$$T_\mathrm{D} = \frac{\hbar}{2k_\mathrm{B}} \frac{\Gamma_{12} s_{12} k_{12}^2 + \Gamma_{13} s_{13} k_{13}^2}{s_{12} k_{12}^2 + s_{13} k_{13}^2} \tag{6.6}$$

Here, $s_{12(13)}$ is the saturation parameter of the 780 (420) nm laser.

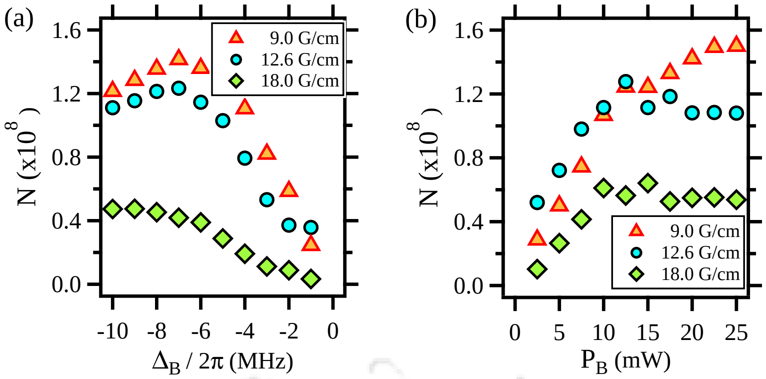

Figure 6.7: No. of atoms (N) vs (a) detuning (Δ_B) and (b) power (P_B) of the blue laser at three different magnetic field gradients: 9 G/cm (orange), 12.6 G/cm (blue) and 18 G/cm (green). In (a), $P_B = 25$ mW and in (b) $\Delta_B = -2\pi \times 7$ MHz. In (a) and (b): $\phi_B = 16$ mm and $\phi_{\text{spot}} = 6$ mm.

6.4 Results and Discussion

Initially, the diameter of all the beams is kept at a maximum, i.e. 16 mm. The diameter of the spot introduced in the core of the IR MOT beam is $\phi_{\text{spot}} = 6$ mm and superimposed with the blue beam. The total power of the IR MOT, repumper, and blue MOT beam are 50 mW, 13 mW, and 25 mW, respectively. Detuning of the respective lasers are $-2\pi \times 10$ MHz, $-2\pi \times 7$ MHz, and $-2\pi \times 7$ MHz, respectively. A magnetic field gradient (B') of 12.6 G/cm is produced using an anti-helmholtz coil. We observe that the no. of atoms in the blue MOT (N) saturates to 1.2×10^8, and its loading time is 2.5 s.

We study the effect of detuning of the blue laser (Δ_B) on the no. of atoms (N) at three different magnetic field gradients. The blue laser's power (P_B) is 25 mW. As shown in Fig. 6.7(a), N increases slightly to 1.2×10^8 at 12.6 G/cm when Δ_B is changed from $-2\pi \times 10$ MHz to $-2\pi \times 7$ MHz. When Δ_B is further varied towards resonance, N decreases, and the MOT disappears. When the magnetic field gradient is increased (decreased) to 18 G/cm (9 G/cm), N decreases (increases).

Next, we vary the power of the blue laser (P_B) at $\Delta_B = -2\pi \times 7$ MHz and study its effect on N at three different magnetic field gradients, as shown in Fig. 6.7(b). At 18 G/cm (green diamond), with the increase in P_B from 2.5 mW to 10 mW, N increases to 6×10^7 and saturates with further increase in P_B. Similar trends are observed for 12.6 G/cm (blue circle) and 9 G/cm (orange triangle). However, P_B for N to reach saturation increases with an increase in magnetic field gradients.

We then switch off the IR MOT beam and optimize the blue MOT to decrease its temperature by lowering its power to 5 mW and changing its detuning to $-2\pi \times 3$ MHz. After a hold time of 20 ms, the blue MOT beam and the magnetic field are switched off. We measure the temperature of the blue MOT to be around $\sim 90\ \mu$K.

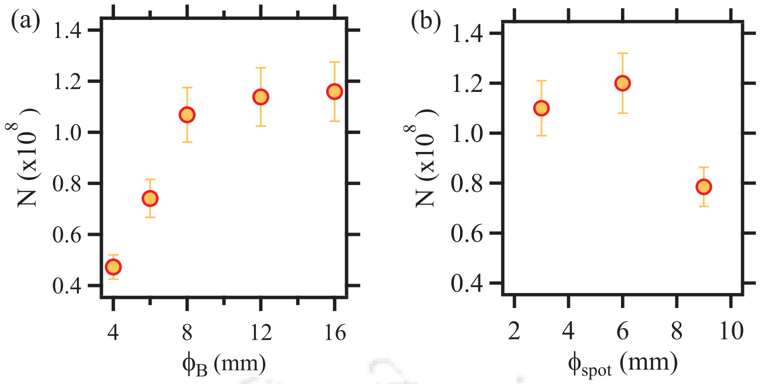

Figure 6.8: No. of atoms (N) in the blue MOT vs diameter of the (a) blue beam (ϕ_B) and (b) spot (ϕ_{spot}). In (a): $\phi_{\text{spot}} = 6$ mm and in (b) $\phi_B = 16$ mm.

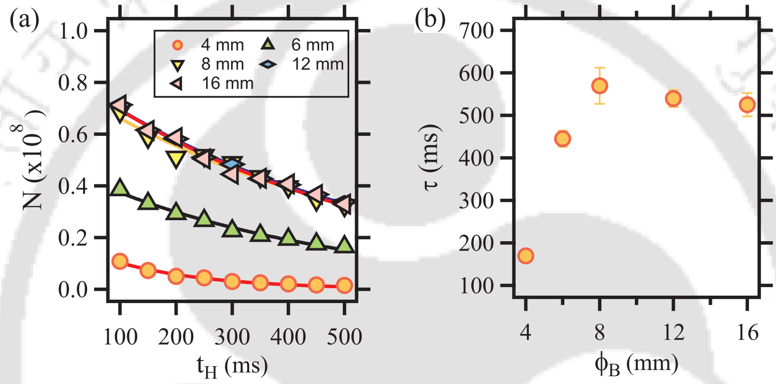

Figure 6.9: (a) No. of atoms (N) in the blue MOT vs hold time (t_H) for different diameter of the blue beam. (b) Lifetime (τ) of the blue MOT vs diameter of the blue beam (ϕ_B). In (a) and (b), $\phi_{\text{spot}} = 6$ mm and $B' = 12.6$ G/cm.

To study the effect of the diameter of the blue beam (ϕ_B), we measure N at different ϕ_B. Fig. 6.8(a) shows the N vs ϕ_B data for the 6 mm diameter of the spot (ϕ_{spot}). We observe that, with increase in ϕ_B from 4 mm to 8 mm, N increases from 4.5×10^7 to 1.1×10^8. With further increase in ϕ_B, there is no significant improvement in N. A similar trend is observed for the spot size of 3 mm. We observe that for better loading of the continuous blue MOT, the diameter of the blue beam should be bigger than the diameter of the spot.

Next, we study N at three different diameters of the spot. Fig. 6.8(b) shows the variation of N vs ϕ_{spot} data for the 16 mm diameter of the blue beam (ϕ_B). When ϕ_{spot} is increased from 3 mm to 6 mm, we observe a slight increase in the number of atoms in the blue MOT to $N = 1.2 \times 10^8$. With further increase in ϕ_{spot} to 9 mm, N significantly drops to 8×10^7. Although N corresponding to $\phi_{\text{spot}} = 3$ mm is slightly lower than that with $\phi_{\text{spot}} = 6$ mm, the lifetime of the blue MOT with $\phi_{\text{spot}} = 3$ mm is around three times lower than the lifetime with $\phi_{\text{spot}} = 6$ mm. The number of atoms in the MOT is decided by the loading rate and loss rate (lifetime). The IR transition has a stronger damping force as compared to the blue transition. The larger spot size reduces the region/ area of stronger damping force (as shown in Fig. 6.5(a) and (b)) and hence reduces the number of atoms in the blue MOT. Smaller spot size increases the stronger trapping region but reduces the lifetime of blue MOT and hence there is a slight decrease in the number of atoms in the blue MOT as shown in Fig. 6.8(b).

We further study the effect of the diameter of the blue beam (ϕ_B) on the lifetime (τ) of the blue MOT. First, we measure N at different hold times (t_H) of the blue MOT and fit the N vs t_H data with the equation: $N = N_0 \times \exp(-t_H/\tau)$. Fig. 6.9(a) shows the variation of N with t_H at different ϕ_B for the blue MOT with spot size 6 mm. The solid lines in Fig. 6.9(a) are exponential fit to the N vs t_H data. Fig. 6.9(b) shows the corresponding lifetime (τ) with ϕ_B. We observe that when ϕ_B is 4 mm, the lifetime of the blue MOT is around 180 ms. It increases to 550 ms when ϕ_B is increased to 8 mm and then remains the same even after increasing the ϕ_B to 16 mm.

6.5 Conclusions

In summary, we have demonstrated the continuous loading of ^{87}Rb atoms in the blue MOT with a typical number of 1.2×10^8 atoms in 2.5 s. The continuous loading of the blue MOT is achieved by superimposing the blue laser beam inside the hollow core (spot) of the IR laser beam driving the broad transition. In order to achieve maximum loading, the spot size should be 6 mm for the total diameter of 16 mm for the IR laser beam and the size of the blue laser beam should be more than 6 mm. This means that the blue laser beam should overfill the spot of the IR laser beam. We have also measured the lifetime of the blue MOT with various diameters of the blue laser beam and found around 500 ms for a beam diameter of more than 6 mm. This method of continuous loading of the blue MOT can be useful to produce continuous atomic beams of cold Rb atoms.

* * *

CHAPTER 7

Role of SGC in Laser cooling

Contents

[1] The well-known sub-Doppler polarization gradient cooling in type-I transition ($F_e = F_g + 1$) is caused by red-detuned lasers. On the other hand, in type-II transition ($F_e \leq F_g$), sub-Doppler cooling takes place through blue-detuned lasers. This opposite behavior for the two types of transitions is due to SGC. In the absence of SGC, both types of transitions show blue-detuned cooling. In this chapter, we experimentally and theoretically demonstrate blue-detuned cooling for both types of transitions in ^{87}Rb. For completeness, we compare the temperatures in various configurations.

7.1 Introduction

Spontaneously generated coherence (SGC) plays an important role in spectroscopy and has been extensively studied in multilevel systems [92, 93, 94, 95, 96, 97, 98, 99]. Since the behavior of laser cooling has a direct connection with the atomic spectrum profile, SGC also plays a crucial role.

---

[1] This chapter is a slightly modified version of the preprint, titled "**Role of spontaneously generated coherence (SGC) in laser cooling of atoms**" by **Rajnandan Choudhury Das**, Samir Khan, Thilagaraj R, and Kanhaiya Pandey, currently under review and is available in arXiv as [4].

In alkali atoms, laser cooling is generally realized using type-I transition, i.e., $F_\mathrm{g} \rightarrow F_\mathrm{e} = F_\mathrm{g}+1$ (where F_g and F_e are ground and excited state total angular momentum). In type-I transition, both Doppler and sub-Doppler cooling require red-detuned lasers. In contrast, for type-II transition ($F_\mathrm{g} \geq F_\mathrm{e}$), Doppler cooling requires red-detuned lasers, while sub-Doppler cooling requires blue-detuned lasers [44]. The opposite behavior of these two types of transitions is attributed to SGC. Red-detuned sub-Doppler cooling is due to SGC which is prominent if the magnetic sub-levels are degenerate and are therefore fragile to the magnetic field [40, 41, 42, 43, 44, 45]. Achieving low temperatures involves carefully nullifying the magnetic field, a task not feasible in the MOT phase.

It is known that blue-detuned cooling occurs in MOT at type-II transition and has been demonstrated in Rb with significant advantages [45, 83, 84]. Blue-detuned MOTs have also been demonstrated in molecules and are crucial for cold molecule experiments [85, 86, 87, 88]. In this work, we show that blue-detuned cooling in MOT is possible even in type-I transition.

In the experiment, we utilize a narrow open transition in ^{87}Rb for MOT [1, 3, 82], similar to Li [60, 61], K [62], Ca [47, 48], Sr [49, 50], Yb [51, 52], Dy [53, 54], Er [55, 56, 57], Cd [58], Eu [59], etc. The MOT for ^{87}Rb atoms is realized at a narrow open transition at 420 nm, which has a 4-5 times lower theoretical Doppler temperature (34 μK) than the regularly used broad transition at 780 nm. Since the blue transition is open, we observe that the repumper laser plays a crucial role in lowering the temperature of the narrow-line MOT. We observed that the blue-detuned repumper causes further cooling in both type-I ($F_\mathrm{g} = 1 \rightarrow F_\mathrm{e} = 2$) and type-II ($F_\mathrm{g} = 1 \rightarrow F_\mathrm{e} = 1$) transitions in the MOT. We have also explored various other configurations that produce both red-detuned and blue-detuned blue MOTs of Rb.

In this work, we undertake a comprehensive numerical investigation employing a density matrix analysis to explore the impact of SGC on the sub-Doppler force within an atomic system characterized by the $F_\mathrm{g} = 1 \rightarrow F_\mathrm{e} = 2$ transition. Our primary objective is to assess the feasibility of blue-detuned laser cooling in MOT. Subsequently, through experimental exploration, we investigate various configurations of blue-detuned MOTs for Rb at a narrow transition on the D$_1$ and D$_2$ lines. Our results, augmented by the density matrix analysis, demonstrate the efficacy of blue-detuned laser cooling even in type-I MOTs, achieving sub-Doppler temperatures as low as 24 μK in the D$_1$ MOT and 31 μK in the D$_2$ MOT.

7.2 Theory

First, we analyze the cooling by two counter-propagating lasers with σ^+ and σ^- polarizations for $F_\mathrm{g} = 1 \rightarrow F_\mathrm{e} = 2$ with all the magnetic sub-levels (as shown in Fig.

7.1 (a)) using density matrix calculations. The Hamiltonian, H of the 8 level system under the electric-dipole and rotating wave approximation and in the rotating frame is expressed as $H = H_A + H_I$, where

$$\begin{aligned} H_A = \hbar\{ & -2kv\,|3\rangle\langle 3| + (kv-\Delta)\,|4\rangle\langle 4| + (kv-\Delta)\,|5\rangle\langle 5| \\ & -(kv+\Delta)\,|6\rangle\langle 6| - (kv+\Delta)\,|7\rangle\langle 7| \\ & -(3kv+\Delta)\,|8\rangle\langle 8|\,\} \end{aligned} \tag{7.1}$$

and

$$\begin{aligned} H_I = \frac{1}{2}\hbar\Omega\{ & |1\rangle\langle 4| + \frac{1}{\sqrt{6}}|1\rangle\langle 6| + \frac{1}{\sqrt{2}}|2\rangle\langle 5| + \frac{1}{\sqrt{2}}|2\rangle\langle 7| \\ & + \frac{1}{\sqrt{6}}|3\rangle\langle 5| + |3\rangle\langle 8|\,\} + h.c. \end{aligned} \tag{7.2}$$

Here, Δ, Ω, and k denote the detuning, rabi frequency, and magnitude of the wave vector of the lasers respectively, and v is the velocity of the atoms. The atom-field interaction is described by writing the Liouville-von Neumann equation for the density matrix,

$$\dot{\rho} = -\frac{i}{\hbar}[H,\rho] + L(\rho) \tag{7.3}$$

Here, $L(\rho)$ accounts for the spontaneous decay of atoms via various channels. The formulation of the Hamiltonian and decay matrix for this system is discussed in detail in Sec. 2.8. 64 simultaneous differential equations are obtained. Only equations for $\dot{\rho}_{12}$, $\dot{\rho}_{13}$ and $\dot{\rho}_{23}$ have the effect of SGC, which are given below. The terms appearing due to SGC are underlined.

$$\begin{aligned} \dot{\rho}_{12} = & -\frac{i}{2}\Omega(\rho_{42} + \frac{1}{\sqrt{6}}\rho_{62}) + \frac{i}{2\sqrt{2}}\Omega^*(\rho_{15} + \rho_{17}) \\ & \underline{+\Gamma(\frac{1}{\sqrt{2}}\rho_{45} + \frac{1}{\sqrt{3}}\rho_{56} + \frac{1}{2\sqrt{3}}\rho_{67})} \end{aligned} \tag{7.4}$$

$$\begin{aligned} \dot{\rho}_{13} = & -\frac{i}{2}\Omega(\rho_{43} + \frac{1}{\sqrt{6}}\rho_{63}) + \frac{i}{2}\Omega^*(\frac{1}{\sqrt{6}}\rho_{16} + \rho_{18}) \\ & + 2ikv\rho_{13} \underline{+\Gamma(\frac{1}{\sqrt{6}}\rho_{46} + \frac{1}{2}\rho_{57} + \frac{1}{\sqrt{6}}\rho_{68})} \end{aligned} \tag{7.5}$$

$$\begin{aligned} \dot{\rho}_{23} = & -\frac{i}{2\sqrt{2}}\Omega(\rho_{53} + \rho_{73}) + \frac{i}{2}\Omega^*(\frac{1}{\sqrt{6}}\rho_{26} + \rho_{28}) \\ & + ikv\rho_{23} \underline{+\Gamma(\frac{1}{2\sqrt{3}}\rho_{56} + \frac{1}{\sqrt{3}}\rho_{67} + \frac{1}{\sqrt{2}}\rho_{78})} \end{aligned} \tag{7.6}$$

The remaining equations are presented below.

$\dot{\rho}_{11} = -\frac{i}{2}\Omega(\rho_{41} + \frac{1}{\sqrt{6}}\rho_{61}) + c.c. + \Gamma(\rho_{44} + \frac{1}{2}\rho_{55} + \frac{1}{6}\rho_{66})$,

$$
\begin{aligned}
&\dot{\rho}_{22} = -\tfrac{i}{2\sqrt{2}}\Omega(\rho_{52} + \rho_{72}) + c.c. + \Gamma(\tfrac{1}{2}\rho_{55} + \tfrac{2}{3}\rho_{66} + \tfrac{1}{2}\rho_{77}),\\
&\dot{\rho}_{33} = -\tfrac{i}{2}\Omega(\tfrac{1}{\sqrt{6}}\rho_{63} + \rho_{83}) + c.c. + \Gamma(\tfrac{1}{6}\rho_{66} + \tfrac{1}{2}\rho_{77} + \rho_{88}),\\
&\dot{\rho}_{44} = \tfrac{i}{2}\Omega\rho_{41} + c.c. - \Gamma\rho_{44},\\
&\dot{\rho}_{55} = \tfrac{i}{2\sqrt{2}}\Omega\rho_{52} + c.c. - \Gamma\rho_{55},\\
&\dot{\rho}_{66} = \tfrac{i}{2\sqrt{6}}\Omega(\rho_{61} + \rho_{63}) + c.c. - \Gamma\rho_{66},\\
&\dot{\rho}_{77} = \tfrac{i}{2\sqrt{2}}\Omega\rho_{72} + c.c. - \Gamma\rho_{77},\\
&\dot{\rho}_{88} = \tfrac{i}{2\sqrt{2}}\Omega\rho_{83} + c.c. - \Gamma\rho_{88},\\
&\dot{\rho}_{14} = \tfrac{i}{2}\Omega(\rho_{11} - \rho_{44} - \tfrac{1}{\sqrt{6}}\rho_{64}) - i\;(\Delta - kv)\,\rho_{14} - \tfrac{1}{2}\Gamma\rho_{14},\\
&\dot{\rho}_{15} = \tfrac{i}{2}\Omega(\tfrac{1}{\sqrt{2}}\rho_{12} - \rho_{45} - \tfrac{1}{\sqrt{6}}\rho_{65}) - i\;(\Delta - kv)\,\rho_{15} - \tfrac{1}{2}\Gamma\rho_{15},\\
&\dot{\rho}_{16} = \tfrac{i}{2}\Omega(\tfrac{1}{\sqrt{6}}\rho_{11} + \tfrac{1}{\sqrt{6}}\rho_{13} - \rho_{46} - \tfrac{1}{\sqrt{6}}\rho_{66}) - i\;(\Delta + kv)\,\rho_{16} - \tfrac{1}{2}\Gamma\rho_{16},\\
&\dot{\rho}_{17} = \tfrac{i}{2}\Omega(\tfrac{1}{\sqrt{2}}\rho_{12} - \rho_{47} - \tfrac{1}{\sqrt{6}}\rho_{67}) - i\;(\Delta + kv)\,\rho_{17} - \tfrac{1}{2}\Gamma\rho_{17},\\
&\dot{\rho}_{18} = \tfrac{i}{2}\Omega(\rho_{13} - \rho_{48} - \tfrac{1}{\sqrt{6}}\rho_{68}) - i\;(\Delta + 3kv)\,\rho_{18} - \tfrac{1}{2}\Gamma\rho_{18},\\
&\dot{\rho}_{24} = \tfrac{i}{2}\Omega(\rho_{21} - \tfrac{1}{\sqrt{2}}\rho_{54} - \tfrac{1}{\sqrt{2}}\rho_{74}) - i\;(\Delta - kv)\,\rho_{24} - \tfrac{1}{2}\Gamma\rho_{24},\\
&\dot{\rho}_{25} = \tfrac{i}{2\sqrt{2}}\Omega(\rho_{22} - \rho_{55} - \rho_{75}) - i\,(\Delta - kv)\,\rho_{25} - \tfrac{1}{2}\Gamma\rho_{25},\\
&\dot{\rho}_{26} = \tfrac{i}{2}\Omega(\tfrac{1}{\sqrt{6}}\rho_{21} + \tfrac{1}{\sqrt{6}}\rho_{23} - \tfrac{1}{\sqrt{2}}\rho_{56} - \tfrac{1}{\sqrt{2}}\rho_{76}) - i(\Delta + kv)\rho_{26} - \tfrac{1}{2}\Gamma\rho_{26},\\
&\dot{\rho}_{27} = \tfrac{i}{2\sqrt{2}}\Omega(\rho_{22} - \rho_{57} - \rho_{77}) - i(\Delta + kv)\rho_{27} - \tfrac{1}{2}\Gamma\rho_{27},\\
&\dot{\rho}_{28} = \tfrac{i}{2}\Omega(\rho_{23} - \tfrac{1}{\sqrt{2}}\rho_{58} - \tfrac{1}{\sqrt{2}}\rho_{78}) - i(\Delta + 3kv)\rho_{28} - \tfrac{1}{2}\Gamma\rho_{28},\\
&\dot{\rho}_{34} = \tfrac{i}{2}\Omega(\rho_{31} - \tfrac{1}{\sqrt{6}}\rho_{64} - \rho_{84}) - i(\Delta + kv)\rho_{34} - \tfrac{1}{2}\Gamma\rho_{34},\\
&\dot{\rho}_{35} = \tfrac{i}{2}\Omega(\tfrac{1}{\sqrt{2}}\rho_{32} - \tfrac{1}{\sqrt{6}}\rho_{65} + \rho_{85}) - i(\Delta + kv)\rho_{35} - \tfrac{1}{2}\Gamma\rho_{35},\\
&\dot{\rho}_{36} = \tfrac{i}{2}\Omega(\tfrac{1}{\sqrt{6}}\rho_{31} + \tfrac{1}{\sqrt{2}}\rho_{33} - \tfrac{1}{\sqrt{6}}\rho_{66} - \rho_{86}) - i(\Delta + 3kv)\rho_{36} - \tfrac{1}{2}\Gamma\rho_{36},\\
&\dot{\rho}_{37} = \tfrac{i}{2}\Omega(\tfrac{1}{\sqrt{2}}\rho_{32} - \tfrac{1}{\sqrt{6}}\rho_{67} - \rho_{87}) - i(\Delta + 3kv)\rho_{37} - \tfrac{1}{2}\Gamma\rho_{37},\\
&\dot{\rho}_{38} = \tfrac{i}{2}\Omega(\rho_{33} - \tfrac{1}{\sqrt{6}}\rho_{68} - \rho_{88}) - i(\Delta + 5kv)\rho_{38} - \tfrac{1}{2}\Gamma\rho_{38},\\
&\dot{\rho}_{45} = \tfrac{i}{2\sqrt{2}}\Omega\rho_{42} - \tfrac{i}{2}\Omega^{*}\rho_{15} - \Gamma\rho_{45},\\
&\dot{\rho}_{46} = \tfrac{i}{2\sqrt{6}}\Omega(\rho_{41} + \rho_{43}) - \tfrac{i}{2}\Omega^{*}\rho_{16} - 2ikv\rho_{46} - \Gamma\rho_{46},\\
&\dot{\rho}_{47} = \tfrac{i}{2\sqrt{2}}\Omega\rho_{42} - \tfrac{i}{2}\Omega^{*}\rho_{17} - 2ikv\rho_{47} - \Gamma\rho_{47},\\
&\dot{\rho}_{48} = \tfrac{i}{2}\Omega\rho_{43} - \tfrac{i}{2}\Omega^{*}\rho_{18} - 4ikv\rho_{48} - \Gamma\rho_{48},\\
&\dot{\rho}_{56} = \tfrac{i}{2\sqrt{6}}\Omega(\rho_{51} + \rho_{53}) - \tfrac{i}{2\sqrt{2}}\Omega^{*}\rho_{26} - 2ikv\rho_{56} - \Gamma\rho_{56},\\
&\dot{\rho}_{57} = \tfrac{i}{2\sqrt{2}}\Omega(\rho_{52} - \rho_{27}) - 2ikv\rho_{57} - \Gamma\rho_{57},\\
&\dot{\rho}_{58} = \tfrac{i}{2}\Omega(\rho_{53} - \tfrac{1}{\sqrt{2}}\rho_{28}) - 4ikv\rho_{58} - \Gamma\rho_{58},\\
&\dot{\rho}_{67} = \tfrac{i}{2\sqrt{2}}\Omega\rho_{62} - \tfrac{i}{2\sqrt{6}}\Omega^{*}(\rho_{37} + \rho_{17}) - \Gamma\rho_{67},\\
&\dot{\rho}_{68} = \tfrac{i}{2}\Omega\rho_{63} - \tfrac{i}{2\sqrt{6}}\Omega^{*}(\rho_{38} + \rho_{18}) - 2ikv\rho_{68} - \Gamma\rho_{68},\\
&\dot{\rho}_{78} = \tfrac{i}{2}\Omega\rho_{73} - \tfrac{i}{2\sqrt{2}}\Omega^{*}\rho_{28} - 2ikv\rho_{78} - \Gamma\rho_{78}
\end{aligned}
$$

They are numerically solved and the force experienced by the atom is evaluated from the absorption of the σ^+ and σ^- light, following a similar approach as in [3, 89, 90]. The force on the atom can be given by the following expression,

$$F_{\text{damp}} = \hbar k\Omega\ \mathrm{Im}\big[(\rho_{14} - \rho_{38}) + \frac{1}{\sqrt{2}}(\rho_{25} - \rho_{27}) + \frac{1}{\sqrt{6}}(\rho_{36} - \rho_{16})\big] \tag{7.7}$$

In Fig. 7.1 (b), we present the force vs velocity plot for a large velocity range under

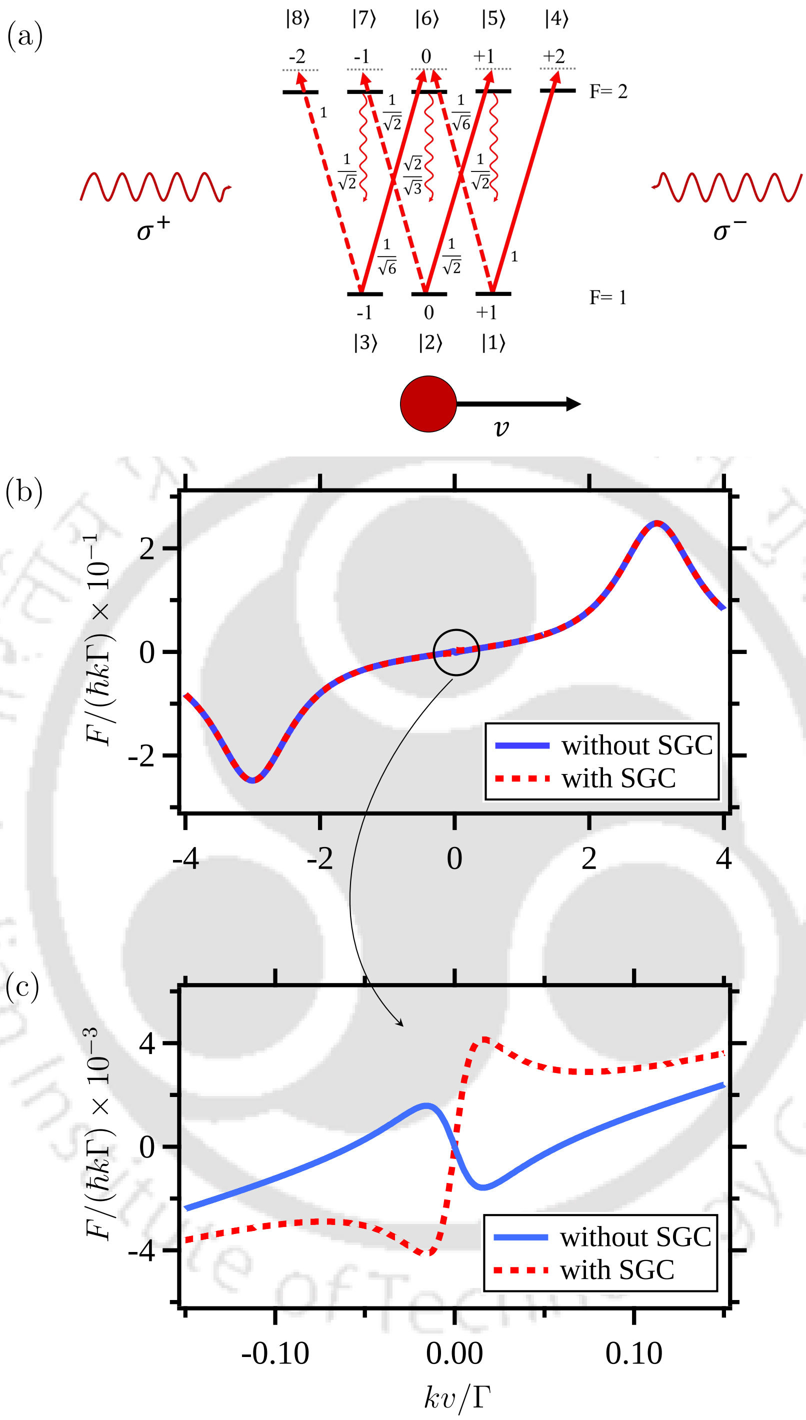

Figure 7.1: (a) Energy level diagram of the $F_g = 1 \rightarrow F_e = 2$ atomic system. All the Zeeman energy levels are labeled using $|i\rangle$ notation. Clebsch-Gordan coefficients are shown near the transitions. Velocity-dependent force curve for the $F_g = 1 \rightarrow F_e = 2$ system is presented for (b) a large velocity range and (c) a small velocity range. The dashed red (solid blue) curve corresponds to the presence (absence) of SGC. The black-circled portion in (b) is magnified and illustrated in (c). Parameters: $\Delta_{1\rightarrow 2} = +3\Gamma$ and $\Omega = \Gamma/\sqrt{2}$.

the influence of blue detuned lasers. The red dashed (blue solid) curve corresponds to the force in the presence (absence) of SGC. Both the curves reveal indistinguishable Doppler force profiles for large velocity ranges. The analysis indicates that atoms with positive (negative) velocities encounter positive (negative) forces, leading to heating in the presence of blue-detuned lasers. These force vs velocity curves undergo sign reversal for negative detuning, indicative of the well-known Doppler cooling.

Zooming into the black-circled region in Fig. 7.1 (b), Fig. 7.1 (c) provides a closer examination of the small velocity range. SGC exerts a substantial influence on the force vs velocity behavior, particularly for lower velocities. In the presence of SGC, atoms with positive (negative) velocities experience a more pronounced positive (negative) force compared to the Doppler force alone, contributing to enhanced heating. Conversely, diminishing the impact of SGC results in a sign reversal in the slope of the force vs velocity curve, indicating the onset of blue-detuned cooling in a type-I system. These curves for force vs velocity flip signs for negative detuning, leading to polarization gradient cooling (heating) in the presence (absence) of SGC.

7.3 Experimental setup

The experimental set-up comprises one commercially available (Toptica) 420 nm (blue) external cavity diode laser (ECDL) and two home-assembled 780 nm (IR) ECDLs. Polarization spectroscopy is employed for the IR MOT laser's frequency stabilization [1], while saturation absorption spectroscopy is used for the IR repumper laser and the blue laser (similar to our previous experiments [2, 3]). Four sets of beams L_1, L_2, L_3 and L_4 are derived which are IR MOT (5S$_{1/2}$, F $= 2 \rightarrow$ 5P$_{3/2}$, F $= 3$), IR repumper (5S$_{1/2}$, F $= 1 \rightarrow$ 5P$_{3/2}$, F $= 1$ or 2), red detuned blue MOT (5S$_{1/2}$, F $= 2 \rightarrow$ 6P$_{3/2}$, F $= 3$) and blue detuned blue MOT (at D$_1$ or D$_2$ line depending on the configuration) beams respectively. All these beams are switched on/off using AOMs. Each beam is further divided into 3 beams, overlapped, co-propagated, made circularly polarized using dual $\lambda/4$ wave plates, expanded to a diameter of 25 mm, sent to the MOT chamber, and retro-reflected back using dual $\lambda/4$ wave plate and mirror. In each arm, the polarization of L_1 and L_3 are the same, and L_2 and L_4 are the same but orthogonal to L_1 and L_3.

Atomic vapor is introduced into the MOT chamber by passing 2.15 A current to the dispenser (AlfaSource AS-Rb-0090-2C). First, the IR MOT is loaded for 2 s at quadruple magnetic field (B') of 12.5 G/cm by switching on L_1 (power, 50 mW and detuning $-2\pi\times 10$ MHz from 5S$_{1/2}$, F $= 2 \rightarrow$ 5P$_{3/2}$, F $= 3$ transition) and L_2 (power, $P_{1\rightarrow 2} = 33$ mW and detuning, $\Delta_{1\rightarrow 2}/2\pi = +40$ MHz from 5S$_{1/2}$, F $= 1 \rightarrow$ 5P$_{3/2}$, F $= 2$) transition. The power of the L_1 is lowered by 5 times and is waited for 4 ms to lower the temperature. Number of atoms, N in the IR MOT is $\sim 1.3 \times 10^8$ and the temperature, T is ~ 2 mK. Then it is transferred to the red detuned blue MOT by switching off the L_1 beam and switching on the L_3 beam (power 26 mW and

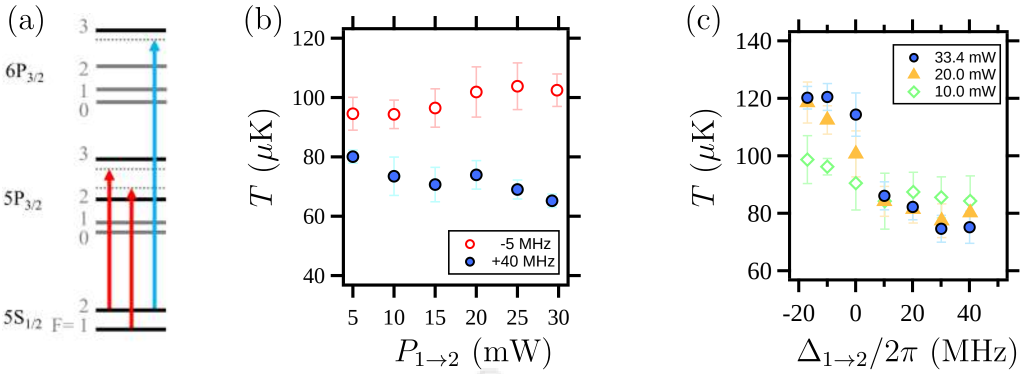

Figure 7.2: (a) Relevant energy levels for studying the effect of repumper laser addressing $F = 1 \to 2$ transition. (b) Temperature vs power of the repumper laser when $\Delta_{1\to2}/2\pi = +40$ MHz (filled blue circle) and -5 MHz (unfilled red circle). (c) Temperature vs detuning of the repumper laser when $P_{1\to2} = 10$ mW (unfilled green diamond), 20 mW (filled yellow triangle), and 33.4 mW (filled blue circle).

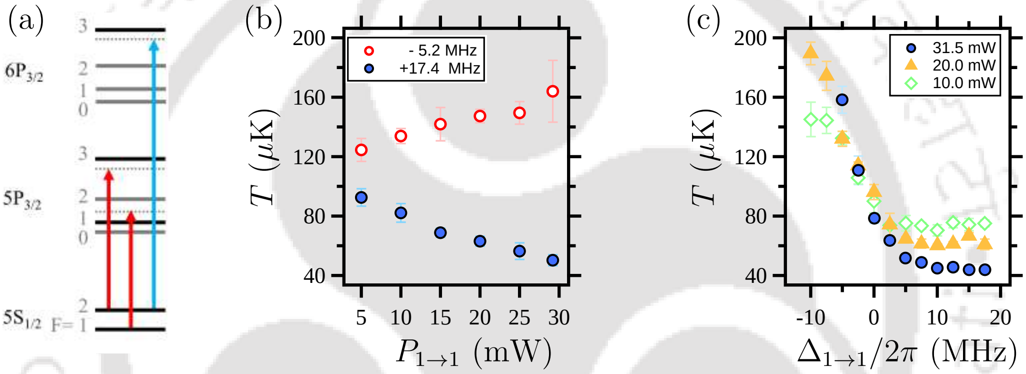

Figure 7.3: (a) Relevant energy levels for studying the effect of repumper laser addressing $F = 1 \to 1$ transition. (b) Temperature vs power of the repumper laser when $\Delta_{1\to1}/2\pi = +17.4$ MHz (filled blue circle) and -5.2 MHz (unfilled red circle). (c) Temperature vs detuning of the repumper laser when $P_{1\to1} = 10$ mW (unfilled green diamond), 20 mW (filled yellow triangle), and 31.5 mW (filled blue circle).

detuning $-2\pi \times 7$ MHz from $5S_{1/2}$, F = 2 → $6P_{3/2}$, F = 3 transition). After 4 ms, the power of L_3 beam is reduced to 10 mW and detuning is ramped to $\Delta_{2\to3}/2\pi = -3$ MHz in 5 ms. After 20 ms of hold time, L_2, L_3, and B' are switched off. N and T are measured from the time of flight (TOF) method using absorption imaging at $5S_{1/2}$, F = 2 → $5P_{3/2}$, F = 3 transition on CMOS camera with an exposure time of 100 μs.

7.4 Results and discussion

We first study the effect of the orthogonally polarized IR repumper laser ($F_g = 1 \to F_e = 2$) on the IR MOT by changing the power ($P_{1\to2}$) at $\Delta_{1\to2}/2\pi = +40$ MHz.

We observe that with an increase in $P_{1\to2}$ from 0.5 mW to 33 mW, T of the IR MOT increases from 1 mK to 2 mK. N also increases and saturates to 1.3×10^8. We then vary $\Delta_{1\to2}/2\pi$ from -20 MHz to $+40$ MHz at $P_{1\to2}=33$ mW. We observe no significant change in N and T. This is because the IR MOT laser is driving a close transition and only a small fraction of atoms are lost due to off-resonant excitation.

Now, we study the effect of IR repumper on the red-detuned blue MOT. As the blue transition is open with a large branching ratio, atoms decay continuously to the lower ground state, $F_g=1$. Fig. 7.2 (b) and (c) show the variation of the T with $P_{1\to2}$ and $\Delta_{1\to2}/2\pi$ respectively for the configuration shown in 7.2 (a). Here, the L_3 is at $-2\pi\times3$ MHz detuned to the $5S_{1/2}$, $F=2\to6P_{3/2}$, $F=3$ transition. First, the repumper laser is kept at $+2\pi\times40$ MHz detuned to the F= 1 → F= 2 transition (which is also a type-I transition), and the power of the repumper laser is varied. We observe that with an increase in $P_{1\to2}$ from 5 mW to 30 mW, T decreases from 80 μK to 65 μK as shown in Fig. 7.2 (b) by filled blue circle points. This is opposite to the case when the repumper laser is red-detuned. When $\Delta_{1\to2}/2\pi=-5$ MHz, T increases from 90 μK to 105 μK as shown by unfilled red circle points (a). In both the cases, N increases with the increase in $P_{1\to2}$ and then saturates to 1.1×10^8.

Next, we study the behavior of the red detuned blue MOT with the detuning of the repumper laser, $\Delta_{1\to2}/2\pi$ at three different power: 10 mW, 20 mW, and 33 mW, as shown in Fig. 7.2 (c) by unfilled green diamond, filled yellow triangle and filled blue circle points respectively. When $\Delta_{1\to2}/2\pi$ is varied from -20 MHz to $+40$ MHz at $P_{1\to2}=33$ mW, T decreases from 120 μK to 75 μK and then saturates. A similar pattern is observed at $P_{1\to2}=10$ mW and 20 mW. We observe that blue-detuned laser cooling works even at type-I transition and the blue-detuned repumper laser helps the narrow line MOT at the blue transition to reach a lower temperature than the red-detuned repumper laser.

The same study is done for the configuration shown in Fig. 7.3 (a), where the repumper laser is $-2\pi\times5.2$ MHz red detuned to the F= 1 → F= 1 transition, which is a type-II transition. Similar to the previous case, T increases from 120 μK to 150 μK when the power of the repumper laser ($P_{1\to1}$) is increased from 5 mW to 30 mW (as shown in red in Fig. 7.3 (b)). In the blue detuned repumper laser configuration i.e. when $\Delta_{1\to1}/2\pi=+17.4$ MHz, T shows a decreasing trend from 90 μK to 44 μK with an increase in $P_{1\to1}$ from 5 mW to 30 mW. In both the cases, N increases with $P_{1\to1}$ and then saturates to 1.1×10^8.

We study the effect of repumper laser detuning ($\Delta_{1\to1}/2\pi$) on the blue MOT at three different powers: 10 mW, 20 mW, and 31.5 mW (as shown in Fig. 7.3 (b) by unifilled green diamond, filled yellow triangle and filled blue circle points respectively). At $P_{1\to1}=31.5$ mW, T decreases from >200 μK to 44 μ K and reaches saturation as the $\Delta_{1\to1}/2\pi$ is changed from -10 MHz to $+17$ MHz. A similar trend is observed when $P_{1\to1}=10$ mW and 20 mW, but T saturates to a higher value.

Next, we demonstrate the red detuned blue MOT using $5S_{1/2}$, F= 2 → $6P_{3/2}$, F= 2

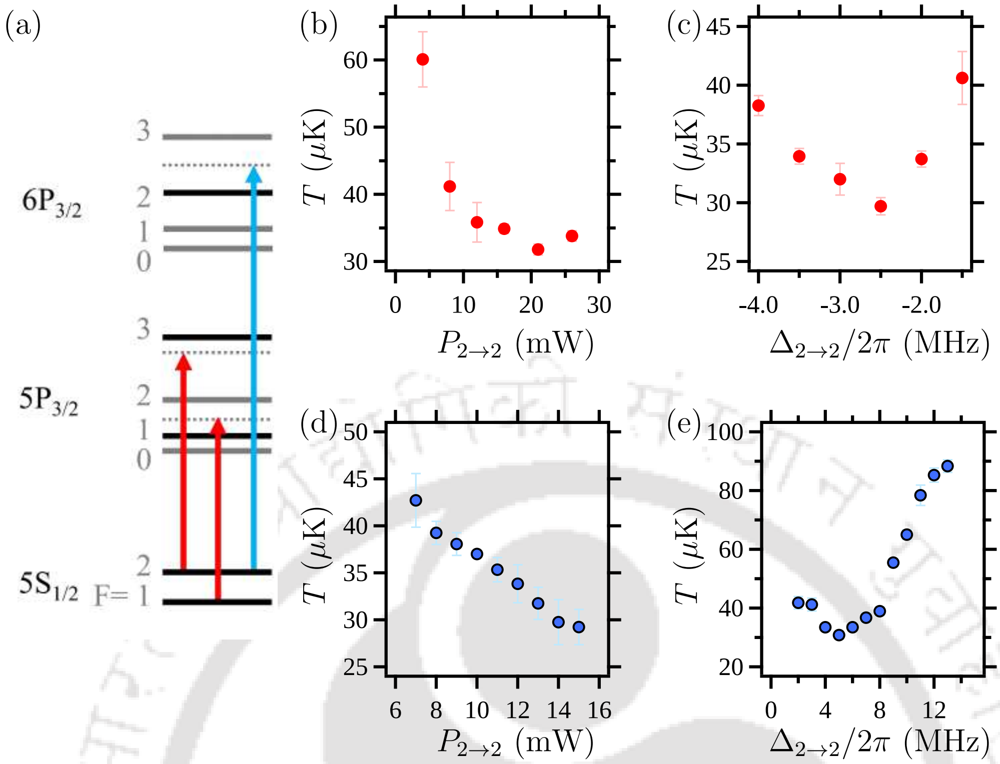

Figure 7.4: (a) Relevant energy levels for studying the effect of the blue laser addressing $F = 2 \to 2$ transition. (b) Temperature vs power of the 420 nm laser (L_3) when $\Delta_{2\to2}/2\pi = -2$ MHz. (c) Temperature vs detuning of the 420 nm laser (L_3) when P$_{2\to2} = 26$ mW. (d) Temperature vs power of the 420 nm blue detuned laser (L_4) when $\Delta_{2\to2}/2\pi = +5$ MHz. (e) Temperature vs detuning of the 420 nm blue detuned laser (L_4) when P$_{2\to2}$ = 15 mW. In (b)-(e), $\Delta_{1\to1}/2\pi = +14$ MHz and P$_{1\to1} = 30$ mW.

transition (type-II MOT) with repumper laser at 30 mW and $+2\pi \times 14$ MHz blue detuned from the 5S$_{1/2}$, F= 1 $\to$ 5P$_{3/2}$, F= 1 transition. We study the effect of the power (P$_{2\to2}$) of the red detuned blue MOT beam at $\Delta_{2\to2}/2\pi = -2.5$ MHz and observe that with an increase in P$_{2\to2}$ from 5 mW to 20 mW, T decreases from 60 μK to 32 μK and then increases after 20 mW, as show in Fig. 7.4 (b). Then we study the effect of $\Delta_{2\to2}$ on the blue MOT at P$_{2\to2}$ = 26 mW and observe that T initially decreases from 38 μK to 32 μK as the $\Delta_{2\to2}/2\pi$ is changed from -4 MHz to -2.5 MHz and then increases to > 40 μK as the detuning is changed towards zero (as shown in Fig. 7.4 (c)). As compared to the minimum temperature of the red detuned blue MOT at 5S$_{1/2}$, F= 2 $\to$ 6P$_{3/2}$, F= 3 transition (44 μK), T of the red detuned blue MOT at 5S$_{1/2}$, F= 2 $\to$ 6P$_{3/2}$, F= 2 transition (32 μK) is lower.

We fix the parameters to load the red detuned blue MOT at 26 mW power and $-2\pi \times 2.5$ MHz detuned from the 5S$_{1/2}$, F= 2 $\to$ 6P$_{3/2}$, F= 2 transition. We then demonstrate the blue-detuned blue MOT using the same transition by transferring the atoms from the red-detuned blue MOT. This is done by switching off the L_3 beams and switching on the L_4 beams. The quadruple magnetic field is also increased

Table 7.1: Temperature of the different MOTs. Detuning (Δ) of each laser from its corresponding transition is shown. IR repumper laser is driving the $5S_{1/2}$, F$= 1 \rightarrow 5P_{3/2}$, F$= X$ transition, where $X = 1$ or 2. Blue MOT laser is driving the $5S_{1/2}$, F$= 2 \rightarrow 6P_{3/2(1/2)}$, F$= X$ transition for the $D_{2(1)}$ MOT, where $X = 1, 2$ or 3.

IR Repumper		**Blue MOT**		**T (μK)**
Transition	$\Delta/2\pi$ (MHz)	Transition	$\Delta/2\pi$ (MHz)	
$1 \rightarrow 2$	+40	D_2, $2 \rightarrow 3$	-3	65 ± 2
$1 \rightarrow 1$	+17	D_2, $2 \rightarrow 3$	-3	44 ± 2
$1 \rightarrow 1$	+17	D_2, $2 \rightarrow 3$	+2	53 ± 2
$1 \rightarrow 1$	+14	D_2, $2 \rightarrow 2$	-2.5	32 ± 1
$1 \rightarrow 1$	+14	D_2, $2 \rightarrow 2$	+5	31 ± 1
$1 \rightarrow 1$	+14	D_1, $2 \rightarrow 2$	-2	40 ± 1
$1 \rightarrow 1$	+14	D_1, $2 \rightarrow 2$	+5	24 ± 1
$1 \rightarrow 1$	+14	D_1, $2 \rightarrow 1$	-2	61 ± 2

to 45 G/cm. We wait for 20 ms for the atoms to settle in the blue-detuned blue MOT. First, we vary the power of the blue detuned blue beam ($P_{2\rightarrow 2}$) from 7 mW to 15 mW at $\Delta_{2\rightarrow 2}/2\pi = +4$ MHz and observe that T decreases from 43 μK to 31 μK and saturates, as shown in Fig. 7.4 (c). We also reduced the blue-detuned blue beam size by 4 times to confirm if we are limited by its power and observe no change in temperature at maximum available power.

Next, we study the effect of the detuning of the blue detuned blue beam ($\Delta_{2\rightarrow 2}$) at fixed power, $P_{2\rightarrow 2} = 15$ mW. As the $\Delta_{2\rightarrow 2}/2\pi$ is changed from +13 MHz to +5 MHz, T decreases from 90 μK to 31 μK and then further increases to > 40 μK as the frequency is changed towards resonance. We do not see any significant difference in temperature between the red detuned blue MOT and the blue detuned blue MOT with $5S_{1/2}$, F$= 2 \rightarrow 6P_{3/2}$, F$= 2$ transition.

We then carry out the same study for the blue MOT in the D_1 line at $5S_{1/2}$, F$= 2 \rightarrow 6P_{1/2}$, F$= 2$ transition, which is also a type-II open transition but of weaker transition strength as compared to the D_2 line. We observe that the minimum temperature of the red detuned blue MOT at D_1 line is 40 μK. We then transfer the atoms to the blue-detuned blue MOT at the same line and observe that T is lowered to 24 μK. No. of atoms in the blue detuned blue MOT at D_1 transition also decreases to 5×10^7.

We also study other configurations of the blue MOT and the minimum temperature achieved at different configurations are summarized in Table 7.1. Unlike in [83], we have observed an almost spherical shape of the atomic cloud with Gaussian distribution of atoms in all different configurations of the MOTs.

7.5 Conclusions

In summary, we observe that SGC plays a crucial role in laser cooling in the sub-Doppler regime. Prior to this work, it was known that there is no sub-Doppler cooling with blue-detuned lasers in type-I transition. In this work, we show that it is possible to achieve cooling with blue-detuned lasers but in the absence of SGC. As SGC is fragile to stray magnetic fields, we observe blue-detuned cooling even in type-I transition in MOT. For completeness, we also explore various combinations for the effectiveness of blue-detuned laser cooling in both type-I and type-II MOT configurations, achieving temperatures as low as 24 μK in the D_1 MOT and 31 μK in the D_2 MOT.

Chapter 8

Conclusions and Future work

In conclusion, we have presented a detailed study on the laser cooling and trapping of Rubidium atoms in the blue magento-optical trap using the $5S_{1/2} \rightarrow 6P_{3/2}$ narrow-line transition at 420 nm. We have also discussed the direct spectroscopy of Rb at the blue transition. This blue transition has a linewidth of $2\pi \times 1.4$ MHz, which is around 4 times narrower than the widely used $5S_{1/2} \rightarrow 5P_{3/2}$ transition of Rb at 780 nm. The Doppler temperature of the blue MOT is 34 μK which is around 4 times lower than the IR MOT (146 μK). Although narrow-line cooling has been demonstrated for the lighter alkali atoms such as Li and K, it was not certain that it would work for Rb, due to its large branching ratio. Experimental demonstration of the temperature reduction in the narrow-line MOT of Rb was important.

We have demonstrated the narrow-line cooling of ^{87}Rb atoms in the MOT using the open transition, $5S_{1/2} \rightarrow 6P_{3/2}$ at 420 nm to trap around 10^8 atoms at typical temperature of 54(10) μK. We have used the two-stage MOT. First, we load the IR MOT of Rb using the $5S_{1/2}$, F = 2 $\rightarrow$ $5P_{3/2}$, F = 3 transition at 780 nm and then, transferred the atoms to the blue MOT using the $5S_{1/2}$, F = 2 $\rightarrow$ $6P_{3/2}$, F = 3 at 420 nm. As compared to the temperature of the IR MOT, we have got around 8 times lower temperature in the blue MOT. Even though the $5S_{1/2}$, F = 2 $\rightarrow$ $6P_{3/2}$, F = 3 transition is an open transition with a large branching ratio, we have achieved efficient cooling in the blue MOT using the repumper laser at 780 nm.

This method uses the two steps separated in time. Instead, the steps can also be made separated in space. Using this idea, we have presented a method for continuous loading of alkali atoms in the narrow-line MOT. We have demonstrated the continuous loading of around 10^8 Rb atoms in the blue MOT by superimposing the blue laser beam inside the hollow core (spot) of the IR laser beam driving the broad transition. We observe that for maximum loading, the filling beam diameter should be more than the core diameter. For a 16 mm (in diameter) IR beam with a 6 mm (in diameter) hollow core, we have found that the diameter of the blue beam should 8 mm or more. This is because, in the overlapped region, the beam addressing narrow-linewidth transition decreases the temperature, even in the presence of the broad transition. We also gave a theoretical framework for cooling atoms with two simultaneous transitions. We have also measured the lifetime of the blue MOT with various diameters of the blue laser beam and found around 500 ms for a beam diameter of 8 mm or more.

We have also presented a detailed study on the effect of spontaneously generated coherence (SGC) in laser cooling. We have observed that SGC plays a significant role in the sub-Doppler regime. It modifies the sub-Doppler force and results in polarization gradient cooling with red-detuned lasers in the presence of the SGC and blue-detuned cooling in the absence of SGC. As SGC is fragile to the magnetic fields, we have observed blue-detuned cooling even in type-I MOT. For completeness, we have also explored various combinations for the effectiveness of blue-detuned cooling in both type-I and type-II MOT configurations, achieving temperatures as low as 24 μK in the D_1 MOT and 31 μK in the D_2 MOT.

Furthermore, we have also performed the direct spectroscopy of Rb at 420 nm transition. We have systematically examined the effect of temperature of the Rb cell, control beam power, and beam size on SAS dip heights and linewidths. We have achieved the optimal signal-to-noise ratio at a Rb cell temperature of 84 ^{0}C. We have found that the minimum linewidths of the $5S_{1/2}$, F $= 2 \rightarrow 5P_{3/2}$ transitions with F= (2,3) and F= 3 are $2\pi \times 2.7$ MHz and $2\pi \times 2.8$ MHz, respectively. Additionally, we have presented all eight error signals for ^{85}Rb and ^{87}Rb corresponding to 5S $\rightarrow$ 6P transition at 420 nm and 421 nm. This study has helped us in the frequency stabilization of the blue laser and consequently in producing laser-cooled Rb atoms at the blue transition.

The insights gained from this study hold practical implications for applications in quantum technologies, particularly those based on the blue atomic transition of Rb. The study can be used for blue transition-based Rydberg excitation of cold Rb atoms such as using 420 nm and 1015 nm as well as 421 nm and 1004 nm. The narrow-line cooling of atoms in MOT may be useful for loading atoms into the ODT and magnetic quadrupole trap as well as for atom interferometry. The work may also be helpful for field deployable quantum sensors.

* * *

CHAPTER A

Computer Control System: Hardware

The computer control system hardware comprises a computer system with a PCI slot, PCI-DIO-32-HS card, Buffer Card, Relay Card, Digital Card, DAC (Digital to Analog Converter) card, LED board, 68-pin female-female connector, 50-pin Ribbon Connector, and Power Supply. The computer itself featured an AMD Phenom (tm) II X3 710 processor with a clock speed of 2.60 GHz and 3.25 GB usable RAM, operating on Windows 7 Professional. The data flow within the system, from the PCI card to all the other cards, is discussed in Sec. 3.6. All these cards are tested using the steps mentioned in [151]. Fig. A.2, A.3, A.4, A.5, A.6, and A.1 shows the images of all the cards used in our computer control system. These images provide a visual insight into the key components that constitute our hardware setup.

If the computer control system does not work, first double-check the time sequence. Next, check whether the power supply is switched on or off. If the error persists, check the strobe signal on an oscilloscope from the buffer card following the steps in [151]. If the strobe signal is not correct while the time sequence is running, in that case, rotate the potentiometers R13, R14, and R15 of the buffer card (shown in A.3) following the steps in [151].

Figure A.1: Image of the LED Board, 68-pin female-female connector, and 50-pin ribbon connector (from left to right).

Figure A.2: Image of the PCI-DIO-32HS card

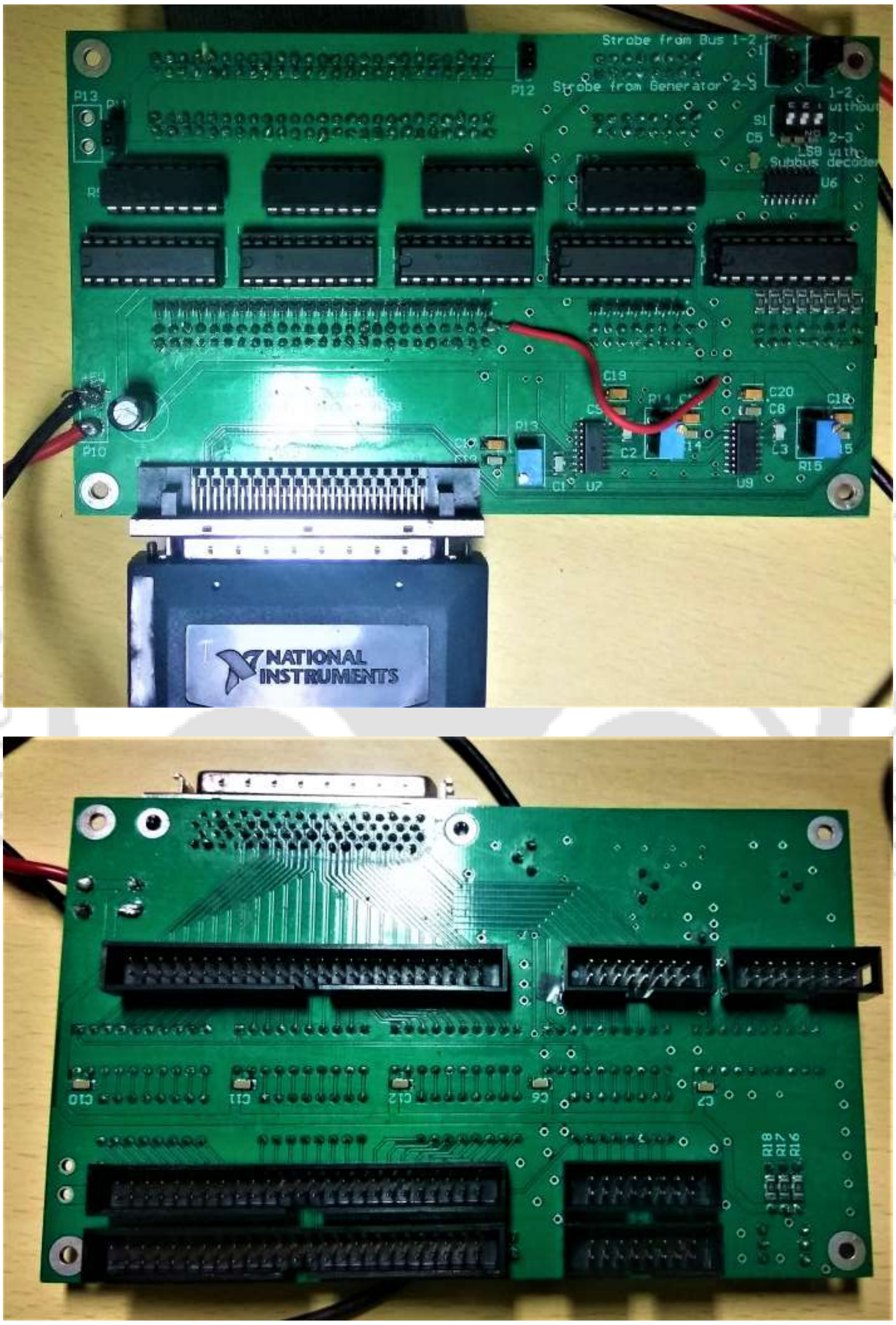

Figure A.3: Image of the buffer card

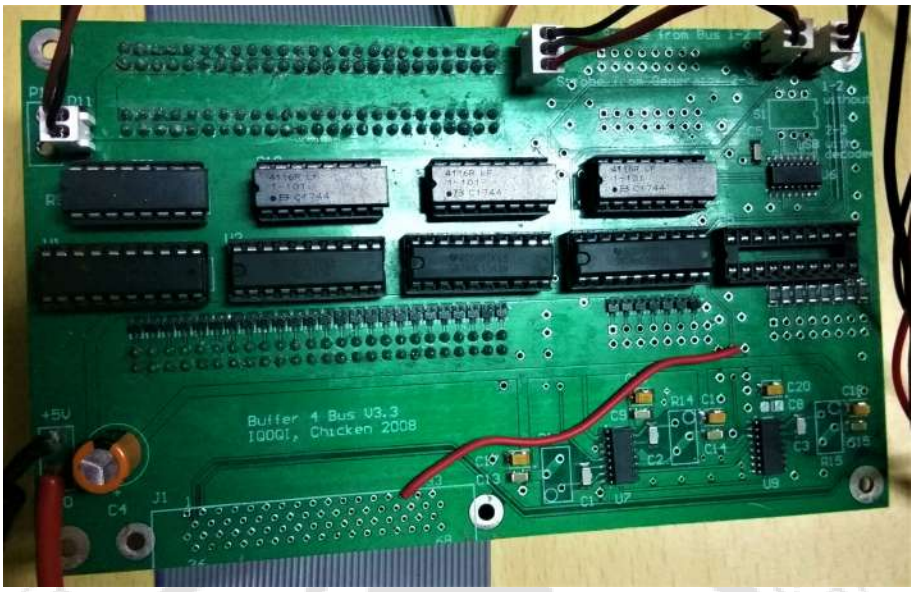

Figure A.4: Image of the relay card

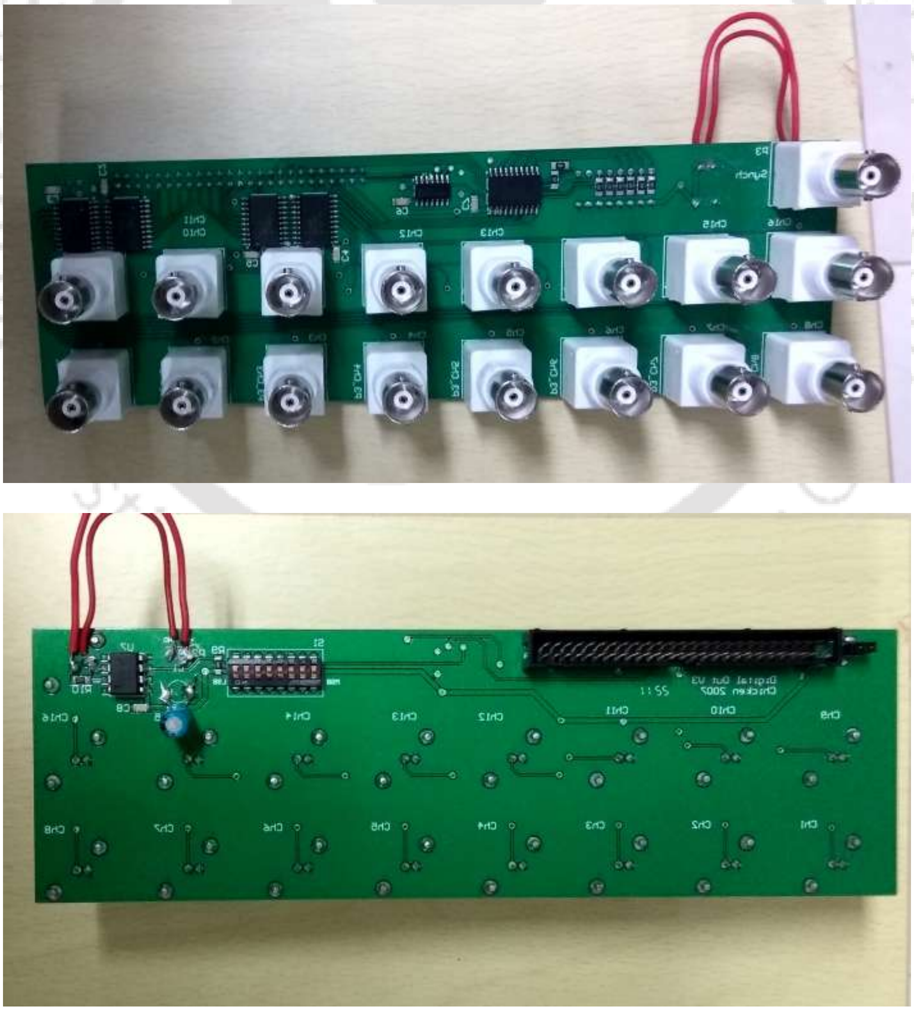

Figure A.5: Image of the digital card

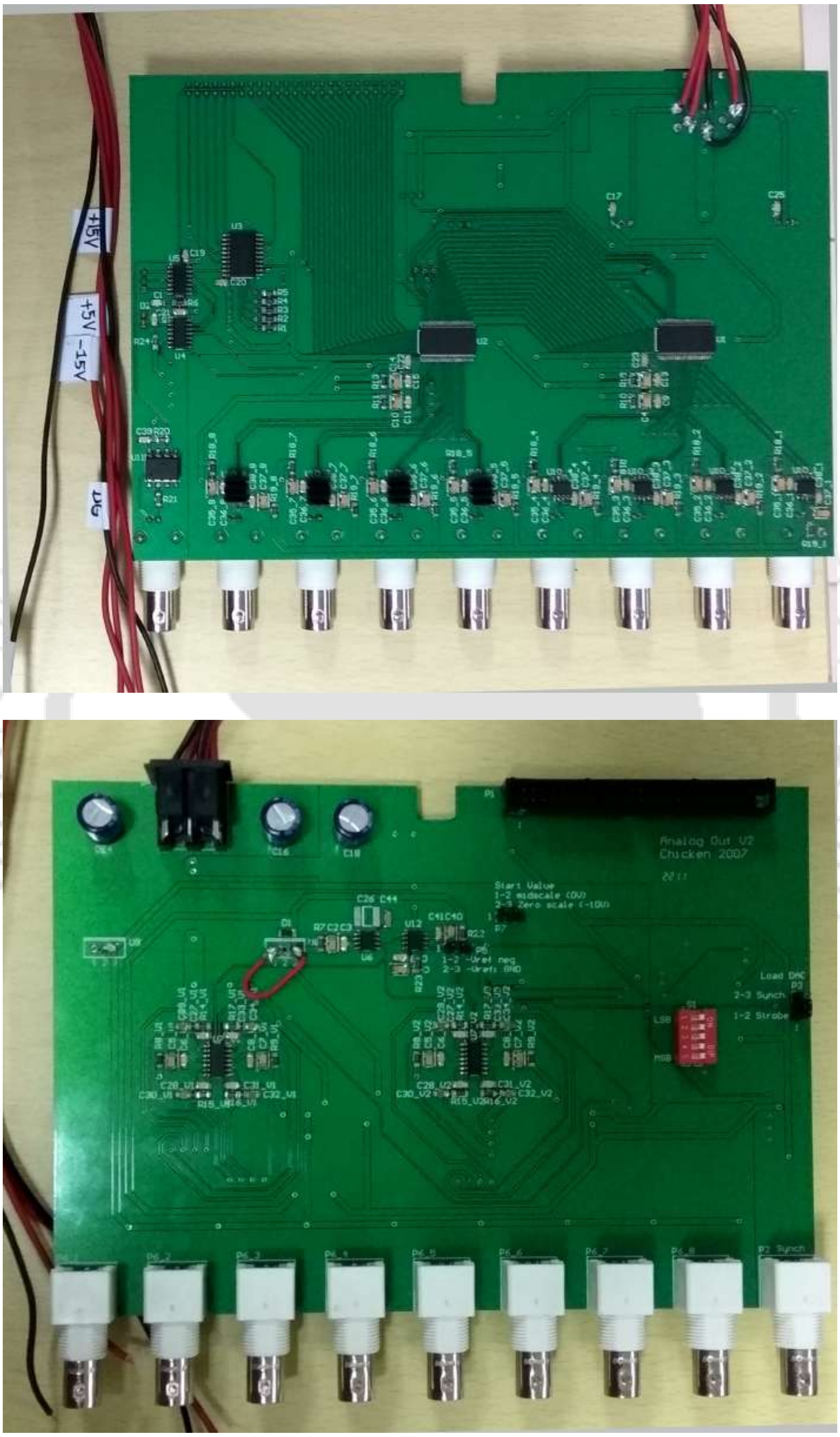

Figure A.6: Image of the analog card

Chapter B

Computer control system: Software

The computer control system's user interface (UI), depicted in Fig. B.1, has been developed using Visual Basic within the vb.net framework. While the current UI is functional for typical cold atom experiments, there is room for enhancement.

B.1 Identifying the various buttons and text boxes

The UI features buttons and text boxes organized into 90 rows (45 on each side) for accommodating various signals in a single experimental run. Each row corresponds to parameters for a specific time coordinate. Columns include *Device Name*, *Address*, *Type*, *Time us*, *Time step*, *End time*, *Data*, *Final Data*, and *Pretrigger*.

B.2 Setting the address of the devices

For every device, the user can give a unique name and unique address. The devices are controlled by the different channels of the digital cards and analog cards. Each card must have a unique address, which can be set using DIP switches on the cards. Each channel of the Analog card by default has a unique address. However, all 16 channels of a digital card have the same address as that of the card. To differentiate each channel, we give each channel an additional number. The following convention is used. Suppose a digital card has address 3, then its 1st channel will have the address 3.01, its second channel will have address 3.02, its 15th channel will have an address 3.15, and so on. With this convention, when the software detects the address as 7.06, the signal will by default go only to the 6th channel of the digital card with address 7. If a signal needs to be transferred to all the 16 digital channels of the same card, then the user needs to put the address as 7.

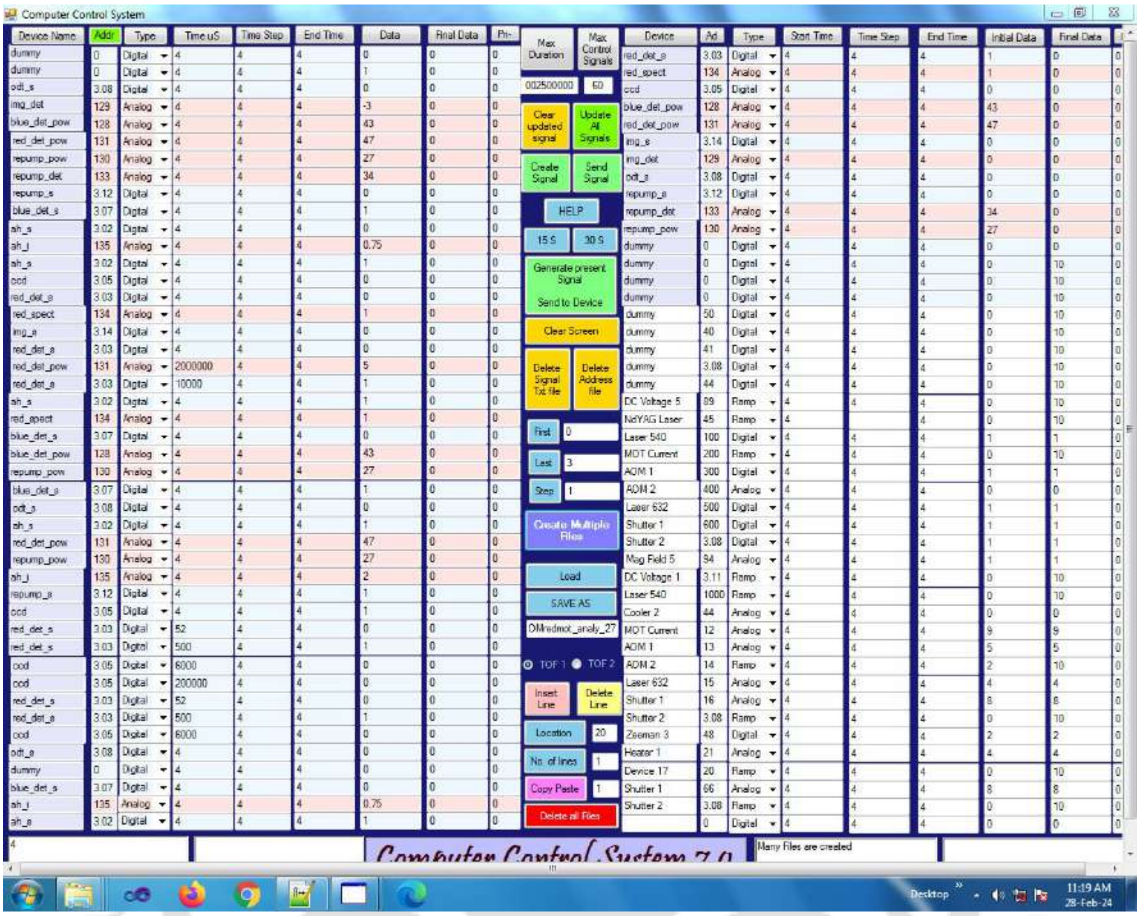

Max Duration: 002500000
Max Control Signals: 60
First: 0
Last: 3
Step: 1
OMredmot_analy_27
Location: 20
No. of lines: 1
Copy Paste: 1
4
Many Files are created

Device Name	Addr	Type	Time uS	Time Step	End Time	Data	Final Data	Pri-
dummy	0	Digital	4	4	4	0	0	0
dummy	0	Digital	4	4	4	1	0	0
odt_s	3.08	Digital	4	4	4	0	0	0
img_det	129	Analog	4	4	4	-3	0	0
blue_det_pow	128	Analog	4	4	4	43	0	0
red_det_pow	131	Analog	4	4	4	47	0	0
repump_pow	130	Analog	4	4	4	27	0	0
repump_det	133	Analog	4	4	4	34	0	0
repump_s	3.12	Digital	4	4	4	0	0	0
blue_det_s	3.07	Digital	4	4	4	1	0	0
ah_s	3.02	Digital	4	4	4	0	0	0
ah_i	135	Analog	4	4	4	0.75	0	0
ah_s	3.02	Digital	4	4	4	1	0	0
ccd	3.05	Digital	4	4	4	0	0	0
red_det_s	3.03	Digital	4	4	4	0	0	0
red_spect	134	Analog	4	4	4	1	0	0
img_s	3.14	Digital	4	4	4	0	0	0
red_det_s	3.03	Digital	4	4	4	0	0	0
red_det_pow	131	Analog	2000000	4	4	5	0	0
red_det_s	3.03	Digital	10000	4	4	1	0	0
ah_s	3.02	Digital	4	4	4	1	0	0
red_spect	134	Analog	4	4	4	1	0	0
blue_det_s	3.07	Digital	4	4	4	0	0	0
blue_det_pow	128	Analog	4	4	4	43	0	0
repump_pow	130	Analog	4	4	4	27	0	0
blue_det_s	3.07	Digital	4	4	4	1	0	0
odt_s	3.08	Digital	4	4	4	0	0	0
ah_s	3.02	Digital	4	4	4	1	0	0
red_det_pow	131	Analog	4	4	4	47	0	0
repump_pow	130	Analog	4	4	4	27	0	0
ah_i	135	Analog	4	4	4	2	0	0
repump_s	3.12	Digital	4	4	4	1	0	0
ccd	3.05	Digital	4	4	4	1	0	0
red_det_s	3.03	Digital	52	4	4	0	0	0
red_det_s	3.03	Digital	500	4	4	1	0	0
ccd	3.05	Digital	6000	4	4	0	0	0
ccd	3.05	Digital	200000	4	4	0	0	0
red_det_s	3.03	Digital	52	4	4	0	0	0
red_det_s	3.03	Digital	500	4	4	1	0	0
ccd	3.05	Digital	6000	4	4	0	0	0
odt_s	3.08	Digital	4	4	4	0	0	0
dummy	0	Digital	4	4	4	0	0	0
blue_det_s	3.07	Digital	4	4	4	0	0	0
ah_i	135	Analog	4	4	4	0.75	0	0
ah_s	3.02	Digital	4	4	4	1	0	0

Device	Ad	Type	Start Time	Time Step	End Time	Initial Data	Final Data	
red_det_s	3.03	Digital	4	4	4	1	0	0
red_spect	134	Analog	4	4	4	1	0	0
ccd	3.05	Digital	4	4	4	0	0	0
blue_det_pow	128	Analog	4	4	4	43	0	0
red_det_pow	131	Analog	4	4	4	47	0	0
img_s	3.14	Digital	4	4	4	0	0	0
img_det	129	Analog	4	4	4	0	0	0
odt_s	3.08	Digital	4	4	4	0	0	0
repump_s	3.12	Digital	4	4	4	0	0	0
repump_det	133	Analog	4	4	4	34	0	0
repump_pow	130	Analog	4	4	4	27	0	0
dummy	0	Digital	4	4	4	0	0	0
dummy	0	Digital	4	4	4	0	10	0
dummy	0	Digital	4	4	4	0	10	0
dummy	0	Digital	4	4	4	0	10	0
dummy	50	Digital	4	4	4	0	10	0
dummy	40	Digital	4	4	4	0	10	0
dummy	41	Digital	4	4	4	0	10	0
dummy	3.08	Digital	4	4	4	0	10	0
dummy	44	Digital	4	4	4	0	10	0
DC Voltage 5	89	Ramp	4	4	4	0	10	0
NdYAG Laser	45	Ramp	4		4	0	10	0
Laser 540	100	Digital	4	4	4	1	1	0
MOT Current	200	Ramp	4	4	4	0	10	0
AOM 1	300	Digital	4	4	4	1	1	0
AOM 2	400	Analog	4	4	4	0	0	0
Laser 632	500	Digital	4	4	4	1	1	0
Shutter 1	600	Digital	4	4	4	1	1	0
Shutter 2	3.08	Digital	4	4	4	1	1	0
Mag Field 5	94	Analog	4	4	4	1	1	0
DC Voltage 1	3.11	Ramp	4	4	4	0	10	0
Laser 540	1000	Ramp	4	4	4	0	10	0
Cooler 2	44	Analog	4	4	4	0	0	0
MOT Current	12	Analog	4	4	4	9	9	0
AOM 1	13	Analog	4	4	4	5	5	0
AOM 2	14	Ramp	4	4	4	2	10	0
Laser 632	15	Analog	4	4	4	4	4	0
Shutter 1	16	Analog	4	4	4	8	8	0
Shutter 2	3.08	Ramp	4	4	4	0	10	0
Zeeman 3	48	Digital	4	4	4	2	2	0
Heater 1	21	Analog	4	4	4	4	4	0
Device 17	20	Ramp	4	4	4	0	10	0
Shutter 1	66	Analog	4	4	4	8	8	0
Shutter 2	3.08	Ramp	4	4	4	0	10	0
	0	Digital	4	4	4	0	0	0

Figure B.1: User interface of the computer control system

B.3 Saving the device name and its address

It is difficult to remember the address of the devices. Thus the user can store the device names and their corresponding address. By clicking on the *Device Name* button (at the top left of the UI), a new UI named Form2 can be opened. Write the device names in the first column and their corresponding address in the decimal system. Click the *Device Name* button of Form2 to the list of devices and their addresses. They are saved as *NewDeviceAddress.txt* file in the same directory as the main UI. Once the device name and address are saved, the Form2 UI needs to be closed. To modify any particular device name and address, the text file can be edited manually. To delete the address file, click on the *Delete Address File* button in the main UI.

While entering any time sequence, the user needs to give the device names and click on the *Addr* button on the top left as shown in green. If the device addresses are already stored, then it will automatically update the addresses in the main UI.

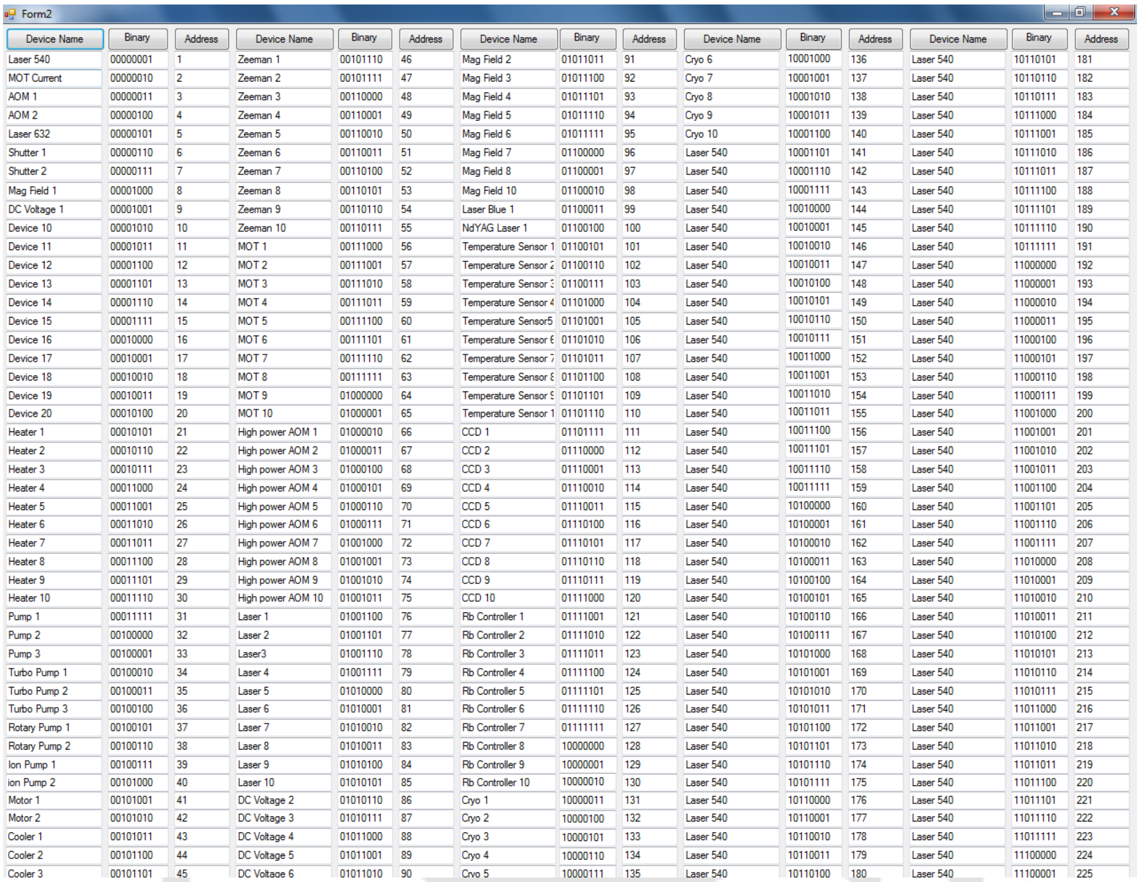

Device Name	Binary	Address	Device Name	Binary	Address	Device Name	Binary	Address	Device Name	Binary	Address	Device Name	Binary	Address
Laser 540	00000001	1	Zeeman 1	00101110	46	Mag Field 2	01011011	91	Cryo 6	10001000	136	Laser 540	10110101	181
MOT Current	00000010	2	Zeeman 2	00101111	47	Mag Field 3	01011100	92	Cryo 7	10001001	137	Laser 540	10110110	182
AOM 1	00000011	3	Zeeman 3	00110000	48	Mag Field 4	01011101	93	Cryo 8	10001010	138	Laser 540	10110111	183
AOM 2	00000100	4	Zeeman 4	00110001	49	Mag Field 5	01011110	94	Cryo 9	10001011	139	Laser 540	10111000	184
Laser 632	00000101	5	Zeeman 5	00110010	50	Mag Field 6	01011111	95	Cryo 10	10001100	140	Laser 540	10111001	185
Shutter 1	00000110	6	Zeeman 6	00110011	51	Mag Field 7	01100000	96	Laser 540	10001101	141	Laser 540	10111010	186
Shutter 2	00000111	7	Zeeman 7	00110100	52	Mag Field 8	01100001	97	Laser 540	10001110	142	Laser 540	10111011	187
Mag Field 1	00001000	8	Zeeman 8	00110101	53	Mag Field 10	01100010	98	Laser 540	10001111	143	Laser 540	10111100	188
DC Voltage 1	00001001	9	Zeeman 9	00110110	54	Laser Blue 1	01100011	99	Laser 540	10010000	144	Laser 540	10111101	189
Device 10	00001010	10	Zeeman 10	00110111	55	NdYAG Laser 1	01100100	100	Laser 540	10010001	145	Laser 540	10111110	190
Device 11	00001011	11	MOT 1	00111000	56	Temperature Sensor 1	01100101	101	Laser 540	10010010	146	Laser 540	10111111	191
Device 12	00001100	12	MOT 2	00111001	57	Temperature Sensor 2	01100110	102	Laser 540	10010011	147	Laser 540	11000000	192
Device 13	00001101	13	MOT 3	00111010	58	Temperature Sensor 3	01100111	103	Laser 540	10010100	148	Laser 540	11000001	193
Device 14	00001110	14	MOT 4	00111011	59	Temperature Sensor 4	01101000	104	Laser 540	10010101	149	Laser 540	11000010	194
Device 15	00001111	15	MOT 5	00111100	60	Temperature Sensor5	01101001	105	Laser 540	10010110	150	Laser 540	11000011	195
Device 16	00010000	16	MOT 6	00111101	61	Temperature Sensor 6	01101010	106	Laser 540	10010111	151	Laser 540	11000100	196
Device 17	00010001	17	MOT 7	00111110	62	Temperature Sensor 7	01101011	107	Laser 540	10011000	152	Laser 540	11000101	197
Device 18	00010010	18	MOT 8	00111111	63	Temperature Sensor 8	01101100	108	Laser 540	10011001	153	Laser 540	11000110	198
Device 19	00010011	19	MOT 9	01000000	64	Temperature Sensor 9	01101101	109	Laser 540	10011010	154	Laser 540	11000111	199
Device 20	00010100	20	MOT 10	01000001	65	Temperature Sensor 1	01101110	110	Laser 540	10011011	155	Laser 540	11001000	200
Heater 1	00010101	21	High power AOM 1	01000010	66	CCD 1	01101111	111	Laser 540	10011100	156	Laser 540	11001001	201
Heater 2	00010110	22	High power AOM 2	01000011	67	CCD 2	01110000	112	Laser 540	10011101	157	Laser 540	11001010	202
Heater 3	00010111	23	High power AOM 3	01000100	68	CCD 3	01110001	113	Laser 540	10011110	158	Laser 540	11001011	203
Heater 4	00011000	24	High power AOM 4	01000101	69	CCD 4	01110010	114	Laser 540	10011111	159	Laser 540	11001100	204
Heater 5	00011001	25	High power AOM 5	01000110	70	CCD 5	01110011	115	Laser 540	10100000	160	Laser 540	11001101	205
Heater 6	00011010	26	High power AOM 6	01000111	71	CCD 6	01110100	116	Laser 540	10100001	161	Laser 540	11001110	206
Heater 7	00011011	27	High power AOM 7	01001000	72	CCD 7	01110101	117	Laser 540	10100010	162	Laser 540	11001111	207
Heater 8	00011100	28	High power AOM 8	01001001	73	CCD 8	01110110	118	Laser 540	10100011	163	Laser 540	11010000	208
Heater 9	00011101	29	High power AOM 9	01001010	74	CCD 9	01110111	119	Laser 540	10100100	164	Laser 540	11010001	209
Heater 10	00011110	30	High power AOM 10	01001011	75	CCD 10	01111000	120	Laser 540	10100101	165	Laser 540	11010010	210
Pump 1	00011111	31	Laser 1	01001100	76	Rb Controller 1	01111001	121	Laser 540	10100110	166	Laser 540	11010011	211
Pump 2	00100000	32	Laser 2	01001101	77	Rb Controller 2	01111010	122	Laser 540	10100111	167	Laser 540	11010100	212
Pump 3	00100001	33	Laser3	01001110	78	Rb Controller 3	01111011	123	Laser 540	10101000	168	Laser 540	11010101	213
Turbo Pump 1	00100010	34	Laser 4	01001111	79	Rb Controller 4	01111100	124	Laser 540	10101001	169	Laser 540	11010110	214
Turbo Pump 2	00100011	35	Laser 5	01010000	80	Rb Controller 5	01111101	125	Laser 540	10101010	170	Laser 540	11010111	215
Turbo Pump 3	00100100	36	Laser 6	01010001	81	Rb Controller 6	01111110	126	Laser 540	10101011	171	Laser 540	11011000	216
Rotary Pump 1	00100101	37	Laser 7	01010010	82	Rb Controller 7	01111111	127	Laser 540	10101100	172	Laser 540	11011001	217
Rotary Pump 2	00100110	38	Laser 8	01010011	83	Rb Controller 8	10000000	128	Laser 540	10101101	173	Laser 540	11011010	218
Ion Pump 1	00100111	39	Laser 9	01010100	84	Rb Controller 9	10000001	129	Laser 540	10101110	174	Laser 540	11011011	219
ion Pump 2	00101000	40	Laser 10	01010101	85	Rb Controller 10	10000010	130	Laser 540	10101111	175	Laser 540	11011100	220
Motor 1	00101001	41	DC Voltage 2	01010110	86	Cryo 1	10000011	131	Laser 540	10110000	176	Laser 540	11011101	221
Motor 2	00101010	42	DC Voltage 3	01010111	87	Cryo 2	10000100	132	Laser 540	10110001	177	Laser 540	11011110	222
Cooler 1	00101011	43	DC Voltage 4	01011000	88	Cryo 3	10000101	133	Laser 540	10110010	178	Laser 540	11011111	223
Cooler 2	00101100	44	DC Voltage 5	01011001	89	Cryo 4	10000110	134	Laser 540	10110011	179	Laser 540	11100000	224
Cooler 3	00101101	45	DC Voltage 6	01011010	90	Cryo 5	10000111	135	Laser 540	10110100	180	Laser 540	11100001	225

Figure B.2: User interface for saving device name and address

B.4 Types of signals

Next to the address column is the Type column. The Users can choose in general 18 different types of signals. They are broadly classified into three categories: Digital, Analog, and Ramp. The digital signal can give an output of either 0 or 5 V. For output voltage 0 (5), the user needs to enter 0 (1) in the *Data* column of the same row. For a digital signal, values in the *Time Step*, *End Times*, and *Final Data* column have no effect. The other 17 types of signals will be discussed later in Sec. B.12.

B.5 Time co-ordinate of each sequence

The next column is the *Time us*. This keeps track of the time coordinate of the particular row. All the time-related text boxes should be in μs and it should be multiple of 4. This is due to the limitation of the frequency of operation of our PCI card. The *Time us* corresponds to the time after the previous signal. For example, if the user puts 52 in the 6th line. Then the signal will transmit 52 μs after the start of the signal at the 5th line. It is a relative coordinate, not an absolute time coordinate.

B.6 Incorporating the delay

The column *Pretrigger* accounts for the delay between the transmitted signal and the actual response by the device. When a device has a delay of x ms, then the sequence automatically sends the signal x ms before the exact time coordinate at which the signal was supposed to be sent, so that due to the delay device responds at the exact time coordinate.

B.7 Controlling the maximum signals and duration of a signal

This computer control system can send a maximum of 90 signals in a cycle. It can transmit up to 60 s in a cycle. If the number of maximum control signals needs to be reduced, it can be set in the text box below the *Max Control Signals* button. Similarly, if the sequence per cycle is of lesser duration, it can be set in the text box below the *Max Duration* button. It is always better to use less number of control signals and for less duration to avoid unnecessary waste of time.

B.8 Sending the signal

Once the user writes the complete time sequence in the UI, for transmitting the signal, the following sequence should be executed: *Delete Signal Text File* → *Clear updated signal* → *Update all Signals* → *Create Signal* → *Send Signal.*

B.9 Insert, delete, copy and paste

If any particular line/lines need to be deleted, copied, or pasted, they can be done using the *Insert Line*, *Delete Line*, and *Copy Paste* buttons.

Figure B.3: User interface of the computer control system: Extended

B.10 Saving and loading a time sequence

The time sequence can also be saved for later use. For that the user needs to give the name of the file in the text box just below the *SAVE AS* button and click the *SAVE AS* button. To load the previously stored file, just click on the *Load* button and open the stored file.

B.11 Repeating a time sequence for multiple iteractions

Every sequence is stored in the PC in the form of a text file. If the same sequence needs to be repeated multiple times, then the user needs to write the 1 in the *First* text box, 2 in the *Last* text box, and 1 in the *Step* text box and click *Create Multiple File* button. This will create 2 text files with names 1, and 2. These text boxes give rise to a variable p whose value changes from *First* to *Last* with a step size of *Step*. For example, if the user chooses 3, 6, and 2.5, then there will be two values of p: 3 for file 1 and 5.5 for file 2.

It is always important to first delete all existing sequences before creating a signal for multiple iterations. This can be done by clicking the *Delete all Files* button

Now if the user clicks the *Help* button, it opens another UI (*Form*4) as shown in Fig. B.3. If the user now enters the No. of repetition as 3, and click the run Expt. button, then the files will run as per the following: 1-2-1-2-1-2. On the other hand, if the user clicks the *Average* button, then the files will run as 1-1-1-2-2-2. This function comes in handy while analyzing the data when an average over the no. of repetitions is required.

Until now, files have been generated by keeping the TOF 1 radio button checked. All the files are saved in one folder. When the TOF 2 radio button is checked, the files will be saved in another folder. let the folder be A and B. So now, when the button $NEWAVERAGE$ is clicked the following files will be executed: A1-B1-A1-B1-A1-B1-A2-B2-A2-B2-A2-B2. Further, the Max repetition sets the cut-off on the allowed number of repetitions.

B.12 More on the Types of signals

So far, we have discussed only the *Digital* type signal. There are two different analog signals from a single analog channel possible. One is *Analog* and the other is $uCAnalog$. The uC terms refer to the uncalibrated. Thus, when $uCAnalog$ type is chosen and in the *Data* column 5 is written, the analog channel gives 5 V. If the type is chosen as *Analog*, it gives the output according to the calibration, which we will discuss later.

The next type of signals are *Ramp* and $uCRamp$. $uCRamp$ represents the uncalibrated values. In ramp signals, the $Time, timestep$, and $EndTime$ as well as *Data* and $FinalData$ all columns are used. The signal starts at a time coordinate that corresponds to the start time $Time$ at value *Data*. It lasts for a duration of $EndTime$ and reaches the value $FinalData$. The values change linearly but only at discrete time steps of $timestep$.

We have discussed the variable p above. Using this signals with variable parameters can be created. Following are the different types of signals that are useful in experiments, *tAnalog*: fixed output value but at different time coordinates, *tRamp*: fixed Ramp signal but at different start time of the ramp signal, *dRamp*: fixed Ramp signal and fixed start time but the duration of the ramp is varied, *pRamp*: fixed initial value and time, but end value of the ramp is variable, *piRamp*: fixed end value and time but the starting value of the ramp is variable, and their unclibrated counterparts.

B.13 Calibration of an Analog channel

Next, we discuss an example to understand the procedure of doing the calibration of the analog channels. Suppose we need to calibrate the channel corresponding to address 128 of the analog card, which is used to control the power of the first-order diffracted beam. Steps to be followed:

1. Put Power-meter on the 1st-order beam.

2. Enter 001000000 as max Duration, 4 as Max Control Signal.
3. Open a new CCS7.0 software and enter the following: ArbitaryName, 128, uCAnalog, 1000, 4,4, variableVoltage, 0, 0 in the 3rd line (any line preferably not in the 1st line).
4. Click: Delete Signal Txt File → Clear Updated Signal → Update All Signals → Create Signal Txt File → Send Signal
5. Enter a different voltage in place of variable voltage, V, and measure the power, P.
6. Plot V vs P, (not P vs V) and fit the data with a polynomial in the range Pmin to Pmax, i.e. the range where it is fitting well (not necessarily the entire range) and note down the fitting coefficients.
7. Open the 128.txt file located in Desktop/Rajnandan/ComputerControl_Upgrade_001/FinalSoftware/SetOfSignals/Calibration/128.txt.
8. Enter Pmin, Pmax, k0, k1, k2, etc one value in each line till the 11th line. The fitting equation is: $k0 + k1 \times P + k2 \times P^2 + \ldots + k8 \times P^8$ (i.e. upto 8th order). Put 0 in the rest of the lines if you have only 2 coefficients (for ex.)
9. Calibration is done and now to see if the calibration is working fine or not, follow the next steps.
10. Change the combo box type from uCAnalog to Analog and enter the power value (for ex. 4) in place of the variable voltage as mentioned in step 3.
11. Follow step 4 and you should get the same output power (4 mW) if the fitting equation is correct.

B.14 Suggestions and warnings

It is advised to use the PC with the time sequence exclusively for running the time sequence. When a sequence starts, it pops up a black CMD prompt, and shows the various status of the sequence. It is recommended not to close the CMD prompt forcefully after the status shows that the signal transmission has started. The CMD prompt can be closed before this status appears. If by mistake, the user runs multiple unnecessary repetitions, to stop the sequence the user needs to delete the text files manually. Care must be taken while deleting any file. Only files users are very sure can be deleted manually. No folder must be deleted from the computer control signal software and the directory of the software should not be changed.

* * *

Bibliography

[1] R. C. Das, D. Shylla, A. Bera, and K. Pandey, Journal of Physics B: Atomic, Molecular and Optical Physics **56**, 025301 (2023).

[2] R. C. Das, S. Khan, T. Ravi, and K. Pandey, The European Physical Journal D **78**, 40 (2024).

[3] R. C. Das, S. Khan, T. R, and K. Pandey, Continuous loading of magneto-optical trap of rb at narrow transition (2024), arXiv:2401.08286 [physics.atom-ph] .

[4] R. C. Das, S. Khan, T. R, and K. Pandey, Role of spontaneously generated coherence (sgc) in laser cooling of atoms (2024), arXiv:2402.04234 [physics.atom-ph] .

[5] D. Shylla, E. O. Nyakang'o, R. C. Das, and K. Pandey, The European Physical Journal D **76**, 125 (2022).

[6] H. J. Metcalf and P. van der Straten, *Laser Cooling and Trapping* (Springer New York, NY, New York, 1999).

[7] W. D. Phillips, Rev. Mod. Phys. **70**, 721 (1998).

[8] F. Schreck and K. v. Druten, Nature Physics **17**, 1296 (2021).

[9] E. L. Raab, M. Prentiss, A. Cable, S. Chu, and D. E. Pritchard, Phys. Rev. Lett. **59**, 2631 (1987).

[10] E. A. Cornell and C. E. Wieman, Rev. Mod. Phys. **74**, 875 (2002).

[11] R. Maruyama, *Optical Trapping of Ytterbium Atoms*, Ph.D. thesis, University of Washington (2003).

[12] A. Browaeys, D. Barredo, and T. Lahaye, Journal of Physics B: Atomic, Molecular and Optical Physics **49**, 152001 (2016).

[13] L. Bassman, M. Urbanek, M. Metcalf, J. Carter, A. F. Kemper, and W. A. de Jong, Quantum Science and Technology **6**, 043002 (2021).

[14] X. Wu, X. Liang, Y. Tian, F. Yang, C. Chen, Y.-C. Liu, M. K. Tey, and L. You, Chinese Physics B **30**, 020305 (2021).

[15] M. Saffman, Journal of Physics B: Atomic, Molecular and Optical Physics **49**, 202001 (2016).

[16] X.-F. Shi, Quantum Science and Technology **7**, 023002 (2022).

[17] A. D. Ludlow, M. M. Boyd, J. Ye, E. Peik, and P. O. Schmidt, Rev. Mod. Phys. **87**, 637 (2015).

[18] T. Bothwell, D. Kedar, E. Oelker, J. M. Robinson, S. L. Bromley, W. L. Tew, J. Ye, and C. J. Kennedy, Metrologia **56**, 065004 (2019).

[19] W. D. Phillips and H. J. Metcalf, Scientific American **256**, 50 (1987).

[20] C. cohen tannoudji and W. D. Phillips, Physics Today **43**, 33 (1990).

[21] S. Chu, Scientific American **266**, 70 (1992).

[22] A. T. Grier, I. Ferrier-Barbut, B. S. Rem, M. Delehaye, L. Khaykovich, F. Chevy, and C. Salomon, Phys. Rev. A **87**, 063411 (2013).

[23] K. N. Blodgett, D. Peana, S. S. Phatak, L. M. Terry, M. P. Montes, and J. D. Hood, Phys. Rev. Lett. **131**, 083001 (2023).

[24] K. Kim, S. Huh, K. Kwon, and J.-y. Choi, Phys. Rev. A **99**, 053604 (2019).

[25] D. R. Fernandes, F. Sievers, N. Kretzschmar, S. Wu, C. Salomon, and F. Chevy, EPL (Europhysics Letters) **100**, 63001 (2012).

[26] D. Nath, R. K. Easwaran, G. Rajalakshmi, and C. S. Unnikrishnan, Phys. Rev. A **88**, 053407 (2013).

[27] G. Salomon, L. Fouché, P. Wang, A. Aspect, P. Bouyer, and T. Bourdel, EPL (Europhysics Letters) **104**, 63002 (2013).

[28] H.-Z. Chen, X.-C. Yao, Y.-P. Wu, X.-P. Liu, X.-Q. Wang, Y.-X. Wang, Y.-A. Chen, and J.-W. Pan, Phys. Rev. A **94**, 033408 (2016).

[29] G. D. Bruce, E. Haller, B. Peaudecerf, D. A. Cotta, M. Andia, S. Wu, M. Y. H. Johnson, B. W. Lovett, and S. Kuhr, Journal of Physics B: Atomic, Molecular and Optical Physics **50**, 095002 (2017).

[30] J. Ang'ong'a, C. Huang, J. P. Covey, and B. Gadway, Phys. Rev. Res. **4**, 013240 (2022).

[31] G. Colzi, G. Durastante, E. Fava, S. Serafini, G. Lamporesi, and G. Ferrari, Phys. Rev. A **93**, 023421 (2016).

[32] Z. Shi, Z. Li, P. Wang, Z. Meng, L. Huang, and J. Zhang, Chinese Physics Letters **35**, 123701 (2018).

[33] S. Rosi, A. Burchianti, S. Conclave, D. S. Naik, G. Roati, C. Fort, and F. Minardi, Scientific Reports **8**, 1301 (2018).

[34] M. O. Brown, T. Thiele, C. Kiehl, T.-W. Hsu, and C. A. Regal, Phys. Rev. X **9**, 011057 (2019).

[35] D. Boiron, A. Michaud, P. Lemonde, Y. Castin, C. Salomon, S. Weyers, K. Szymaniec, L. Cognet, and A. Clairon, Phys. Rev. A **53**, R3734 (1996).

[36] Y.-F. Hsiao, Y.-J. Lin, and Y.-C. Chen, Phys. Rev. A **98**, 033419 (2018).

[37] Q. Bouton, R. Chang, A. L. Hoendervanger, F. Nogrette, A. Aspect, C. I. Westbrook, and D. Clément, Phys. Rev. A **91**, 061402 (2015).

[38] L. Gabardos, S. Lepoutre, O. Gorceix, L. Vernac, and B. Laburthe-Tolra, Phys. Rev. A **99**, 023607 (2019).

[39] M. Taglieber, *Quantum degeneracy in an atomic Fermi-Fermi-Bose mixture*, Ph.D. thesis, lmu (2008).

[40] J. P. McGilligan, P. F. Griffin, R. Elvin, S. J. Ingleby, E. Riis, and A. S. Arnold, Scientific Reports **7**, 384 (2017).

[41] Y.-S. Chin, M. Steiner, and C. Kurtsiefer, Phys. Rev. A **96**, 033406 (2017).

[42] M. Walhout, U. Sterr, and S. L. Rolston, Phys. Rev. A **54**, 2275 (1996).

[43] M. Walhout, J. Dalibard, S. L. Rolston, and W. D. Phillips, J. Opt. Soc. Am. B **9**, 1997 (1992).

[44] J. A. Devlin and M. R. Tarbutt, New Journal of Physics **18**, 123017 (2016).

[45] K. N. Jarvis, J. A. Devlin, T. E. Wall, B. E. Sauer, and M. R. Tarbutt, Phys. Rev. Lett. **120**, 083201 (2018).

[46] A. V. Rakholia, H. J. McGuinness, and G. W. Biedermann, Phys. Rev. Appl. **2**, 054012 (2014).

[47] E. A. Curtis, C. W. Oates, and L. Hollberg, Phys. Rev. A **64**, 031403 (2001).

[48] E. A. Curtis, C. W. Oates, and L. Hollberg, J. Opt. Soc. Am. B **20**, 977 (2003).

[49] H. Katori, T. Ido, Y. Isoya, and M. Kuwata-Gonokami, Phys. Rev. Lett. **82**, 1116 (1999).

[50] T. Yang, K. Pandey, M. S. Pramod, F. Leroux, C. C. Kwong, E. Hajiyev, Z. Y. Chia, B. Fang, and D. Wilkowski, The European Physical Journal D **69**, 226 (2015).

[51] T. Kuwamoto, K. Honda, Y. Takahashi, and T. Yabuzaki, Phys. Rev. A **60**, R745 (1999).

[52] K. Pandey, K. D. Rathod, A. K. Singh, and V. Natarajan, Phys. Rev. A **82**, 043429 (2010).

[53] M. Lu, S. H. Youn, and B. L. Lev, Phys. Rev. A **83**, 012510 (2011).

[54] T. Maier, H. Kadau, M. Schmitt, A. Griesmaier, and T. Pfau, Opt. Lett. **39**, 3138 (2014).

[55] A. J. Berglund, J. L. Hanssen, and J. J. McClelland, Phys. Rev. Lett. **100**, 113002 (2008).

[56] A. Frisch, K. Aikawa, M. Mark, A. Rietzler, J. Schindler, E. Zupanič, R. Grimm, and F. Ferlaino, Phys. Rev. A **85**, 051401 (2012).

[57] B. Seo, P. Chen, Z. Chen, W. Yuan, M. Huang, S. Du, and G.-B. Jo, Phys. Rev. A **102**, 013319 (2020).

[58] A. Yamaguchi, M. S. Safronova, K. Gibble, and H. Katori, Phys. Rev. Lett. **123**, 113201 (2019).

[59] Y. Miyazawa, R. Inoue, H. Matsui, K. Takanashi, and M. Kozuma, Phys. Rev. A **103**, 053122 (2021).

[60] P. M. Duarte, R. A. Hart, J. M. Hitchcock, T. A. Corcovilos, T.-L. Yang, A. Reed, and R. G. Hulet, Phys. Rev. A **84**, 061406 (2011).

[61] J. Sebastian, C. Gross, K. Li, H. C. J. Gan, W. Li, and K. Dieckmann, Phys. Rev. A **90**, 033417 (2014).

[62] D. C. McKay, D. Jervis, D. J. Fine, J. W. Simpson-Porco, G. J. A. Edge, and J. H. Thywissen, Phys. Rev. A **84**, 063420 (2011).

[63] C. L. Satter, S. Tan, and K. Dieckmann, Phys. Rev. A **98**, 023422 (2018).

[64] O. Morsch and I. Lesanovsky, La Rivista del Nuovo Cimento **41**, 383 (2018).

[65] R. Faoro, C. Simonelli, M. Archimi, G. Masella, M. M. Valado, E. Arimondo, R. Mannella, D. Ciampini, and O. Morsch, Phys. Rev. A **93**, 030701 (2016).

[66] M. M. Valado, C. Simonelli, M. D. Hoogerland, I. Lesanovsky, J. P. Garrahan, E. Arimondo, D. Ciampini, and O. Morsch, Phys. Rev. A **93**, 040701 (2016).

[67] H. Levine, A. Keesling, A. Omran, H. Bernien, S. Schwartz, A. S. Zibrov, M. Endres, M. Greiner, V. Vuletić, and M. D. Lukin, Phys. Rev. Lett. **121**, 123603 (2018).

[68] S. Ebadi, T. T. Wang, H. Levine, A. Keesling, G. Semeghini, A. Omran, D. Bluvstein, R. Samajdar, H. Pichler, W. W. Ho, S. Choi, S. Sachdev, M. Greiner, V. Vuletić, and M. D. Lukin, Nature **595**, 227 (2021).

[69] D. Bluvstein, H. Levine, G. Semeghini, T. T. Wang, S. Ebadi, M. Kalinowski, A. Keesling, N. Maskara, H. Pichler, M. Greiner, V. Vuletić, and M. D. Lukin, Nature **604**, 451 (2022).

[70] L. Salvi, L. Cacciapuoti, G. M. Tino, and G. Rosi, Phys. Rev. Lett. **131**, 103401 (2023).

[71] S. Zhang, X. Zhang, J. Cui, Z. Jiang, H. Shang, C. Zhu, P. Chang, L. Zhang, J. Tu, and J. Chen, Review of Scientific Instruments **88**, 103106 (2017).

[72] L. Ling and G. Bi, Opt. Lett. **39**, 3324 (2014).

[73] X. Guan, W. Zhuang, T. Shi, J. Miao, J. Zhang, J. Chen, and B. Luo, IEEE Photonics Technology Letters **35**, 672 (2023).

[74] S. Pustelny, L. Busaite, M. Auzinsh, A. Akulshin, N. Leefer, and D. Budker, Phys. Rev. A **92**, 053410 (2015).

[75] J. R. Boon, E. Zekou, D. J. Fulton, and M. H. Dunn, Phys. Rev. A **57**, 1323 (1998).

[76] E. O. Nyakang'o, D. Shylla, V. Natarajan, and K. Pandey, Journal of Physics B: Atomic, Molecular and Optical Physics **53**, 095001 (2020).

[77] E. O. Nyakang'o and K. Pandey, Phys. Rev. A **103**, 013107 (2021).

[78] C.-C. Chen, R. González Escudero, J. Minář, B. Pasquiou, S. Bennetts, and F. Schreck, Nature **606**, 683 (2022).

[79] J. Lee, J. H. Lee, J. Noh, and J. Mun, Phys. Rev. A **91**, 053405 (2015).

[80] B. Plotkin-Swing, A. Wirth, D. Gochnauer, T. Rahman, K. E. McAlpine, and S. Gupta, Review of Scientific Instruments **91**, 093201 (2020), https://pubs.aip.org/aip/rsi/article-pdf/doi/10.1063/5.0011361/14798714/093201_1_online.pdf .

[81] J. W. Cho, H.-g. Lee, S. Lee, J. Ahn, W.-K. Lee, D.-H. Yu, S. K. Lee, and C. Y. Park, Phys. Rev. A **85**, 035401 (2012).

[82] R. Ding, A. Orozco, J. Lee, and N. Claussen, *Narrow-linewidth laser cooling for rapid production of low-temperature atoms for high data-rate quantum sensing.*, Tech. Rep. (Sandia National Lab.(SNL-NM), Albuquerque, NM (United States), 2022).

[83] K. N. Jarvis, B. E. Sauer, and M. R. Tarbutt, Phys. Rev. A **98**, 043432 (2018).

[84] B. Piest, V. Vollenkemper, J. Böhm, A. Herbst, and E. M. Rasel, Review of Scientific Instruments **93**, 023202 (2022).

[85] J. J. Burau, P. Aggarwal, K. Mehling, and J. Ye, Phys. Rev. Lett. **130**, 193401 (2023).

[86] S. Xu, R. Li, Y. Xia, M. Siercke, and S. Ospelkaus, Phys. Rev. A **108**, 033102 (2023).

[87] V. Jorapur, T. K. Langin, Q. Wang, G. Zheng, and D. DeMille, High density loading and collisional loss of laser cooled molecules in an optical trap (2023), arXiv:2307.05347 [physics.atom-ph] .

[88] S. J. Li, C. M. Holland, Y. Lu, and L. W. Cheuk, A blue-detuned magneto-optical trap of caf molecules (2023), arXiv:2311.05447 [physics.atom-ph] .

[89] J. Dalibard and C. Cohen-Tannoudji, J. Opt. Soc. Am. B **6**, 2023 (1989).

[90] S. Chang and V. Minogin, Physics Reports **365**, 65 (2002).

[91] G. S. Agarwal, Quantum statistical theories of spontaneous emission and their relation to other approaches, in *Quantum Optics*, edited by G. Höhler (Springer Berlin Heidelberg, Berlin, Heidelberg, 1974) pp. 1–128.

[92] S. Menon and G. S. Agarwal, Phys. Rev. A **57**, 4014 (1998).

[93] A. Lezama, S. Barreiro, and A. M. Akulshin, Phys. Rev. A **59**, 4732 (1999).

[94] A. V. Taichenachev, A. M. Tumaikin, and V. I. Yudin, Phys. Rev. A **61**, 011802 (1999).

[95] W.-H. Xu, J.-H. Wu, and J.-Y. Gao, Optics Communications **215**, 345 (2003).

[96] E. Paspalakis, S.-Q. Gong, and P. L. Knight, Optics Communications **152**, 293 (1998).

[97] D. Wang and Y. Zheng, Phys. Rev. A **83**, 013810 (2011).

[98] Z. Song, Y. Peng, Z.-D. Sun, and Y. Zheng, Journal of Physics B: Atomic, Molecular and Optical Physics **49**, 015001 (2015).

[99] A. Silatan, M. Ghaderi GoranAbad, and M. Mahmoudi, Scientific Reports **13**, 364 (2023).

[100] P. R. Berman, Phys. Rev. A **72**, 035801 (2005).

[101] Z. Ficek and S. Swain, Phys. Rev. A **69**, 023401 (2004).

[102] W. T. Rhodes, T. Asakura, K.-H. Brenner, T. W. Hänsch, T. Kamiya, F. Krausz, B. Monemar, H. Venghaus, H. Weber, and H. Weinfurter, eds., Quantum interference in atomic systems: Mathematical formalism, in *Quantum Interference and Coherence: Theory and Experiments* (Springer New York, New York, NY, 2005) pp. 47–84.

[103] K. Yadav and A. Wasan, Journal of Optics **48**, 65 (2019).

[104] V. Bharti and A. Wasan, Optics Communications **324**, 238 (2014).

[105] V. B. Paramjit Kaur and A. Wasan, Journal of Modern Optics **61**, 1339 (2014), https://doi.org/10.1080/09500340.2014.931479 .

[106] Expm function in matlab, `https://in.mathworks.com/help/matlab/ref/expm.html` (2024), accessed: 2024-5-9.

[107] D. Shylla, E. O. Nyakang'o, and K. Pandey, Scientific Reports **8**, 8692 (2018).

[108] E. O. Nyakang'o and K. Pandey, The European Physical Journal D **74**, 1434 (2020).

[109] M. Bhattarai, S. Khan, V. Natarajan, and K. Pandey, Journal of Physics B: Atomic, Molecular and Optical Physics **54**, 075401 (2021).

[110] J. Javanainen, Europhysics Letters **17**, 407 (1992).

[111] S.-C. Zhao, JETP Letters **94**, 347 (2011).

[112] H. Li, H. Zhang, H. Sun, X. Hu, D. Sun, and X. Li, Appl. Opt. **56**, 4995 (2017).

[113] W. juan Jiang, X. Yan, J. ping Song, H. bin Zheng, C. Wu, B. yin Yin, and Y. Zhang, Optics Communications **282**, 101 (2009).

[114] G. S. Agarwal, Phys. Rev. Lett. **84**, 5500 (2000).

[115] H. mei Ma, S. qing Gong, C. pu Liu, Z. rong Sun, and Z. zhan Xu, Optics Communications **223**, 97 (2003).

[116] P. D. Lett, R. N. Watts, C. I. Westbrook, W. D. Phillips, P. L. Gould, and H. J. Metcalf, Phys. Rev. Lett. **61**, 169 (1988).

[117] W. Lunden, L. Du, M. Cantara, P. Barral, A. O. Jamison, and W. Ketterle, Phys. Rev. A **101**, 063403 (2020).

[118] B. Plotkin-Swing, A. Wirth, D. Gochnauer, T. Rahman, K. E. McAlpine, and S. Gupta, Review of Scientific Instruments **91**, 093201 (2020), https://pubs.aip.org/aip/rsi/article-pdf/doi/10.1063/5.0011361/14798714/093201_1_online.pdf .

[119] W. Demtröder, *Laser spectroscopy*, Vol. 2 (Springer, 1982).

[120] D. A. Smith and I. G. Hughes, American Journal of Physics **72**, 631 (2004), https://pubs.aip.org/aapt/ajp/article-pdf/72/5/631/8504974/631_1_online.pdf .

[121] M. L. Harris, S. L. Cornish, A. Tripathi, and I. G. Hughes, Journal of Physics B: Atomic, Molecular and Optical Physics **41**, 085401 (2008).

[122] E. O. Nyakang'o, D. Shylla, V. Natarajan, and K. Pandey, Journal of Physics B: Atomic, Molecular and Optical Physics **53**, 095001 (2020).

[123] E. O. Nyakang'o and K. Pandey, Phys. Rev. A **103**, 013107 (2021).

[124] D. Shylla, *Atomic Coherence Based Electromagnetic Wave Interferometry*, Ph.D. thesis, Indian Institute of Technology Guwahati (2022).

[125] R. Ding, Narrow line cooling of 84sr (2016), available at `https://hdl.handle.net/1911/96623`.

[126] S. Khan, M. P. Kumar, V. Bharti, and V. Natarajan, The European Physical Journal D **71**, 38 (2017).

[127] B. Wu, Y. Zhou, K. Weng, D. Zhu, Z. Fu, B. Cheng, X. Wang, and Q. Lin, J. Opt. Soc. Am. B **35**, 2705 (2018).

[128] D. Das and V. Natarajan, Journal of Physics B: Atomic, Molecular and Optical Physics **39**, 2013 (2006).

[129] A. Banerjee and V. Natarajan, Optics letters **28**, 1912 (2003).

[130] D. Das and V. Natarajan, The European Physical Journal D-Atomic, Molecular, Optical and Plasma Physics **37**, 313 (2006).

[131] H. Gerhardt, E. Matthias, F. Schneider, and A. Timmermann, Zeitschrift für Physik A Atoms and Nuclei **288**, 327 (1978).

[132] W. Dong-Ying, W. Yan-Fei, T. Zhi-Ming, Z. S.-N. H. Ye-Long, Z. Wei, and C. Jing-Biao, Chinese Physics Letters **30**, 060601 (2013).

[133] J. Miao, T. Shi, J. Zhang, and J. Chen, Phys. Rev. Appl. **18**, 024034 (2022).

[134] X. Zhang, Z. Jiang, Z. Tao, H. Shang, C. Zhang, and J. Chen, in *2016 IEEE International Frequency Control Symposium (IFCS)* (2016) pp. 1–3.

[135] S. Zhang, X. Zhang, Z. Jiang, D. Pan, X. Peng, H. Chen, J. Chen, and H. Guo, in *2016 IEEE International Frequency Control Symposium (IFCS)* (2016) pp. 1–4.

[136] C. Glaser, F. Karlewski, J. Kluge, J. Grimmel, M. Kaiser, A. Günther, H. Hattermann, M. Krutzik, and J. Fortágh, Phys. Rev. A **102**, 012804 (2020).

[137] A. Hemmerich, D. H. McIntyre, C. Zimmermann, and T. W. Hänsen, Opt. Lett. **15**, 372 (1990).

[138] K. Hayasaka, Optics Communications **206**, 401 (2002).

[139] P. Chang, S. Zhang, H. Shang, and J. Chen, Applied Physics B **125**, 196 (2019).

[140] D. Pizzey, J. Briscoe, F. Logue, F. Ponciano-Ojeda, S. Wrathmall, and I. Hughes, New Journal of Physics **24**, 125001 (2022).

[141] W. Xia, S.-Y. Dai, Y. Zhang, K.-Q. Li, Q. Yu, and X.-Z. Chen, Chinese Physics Letters **33**, 053201 (2016).

[142] M. V. Romalis, E. Miron, and G. D. Cates, Phys. Rev. A **56**, 4569 (1997).

[143] C. Glaser, F. Karlewski, J. Kluge, J. Grimmel, M. Kaiser, A. Günther, H. Hattermann, M. Krutzik, and J. Fortágh, Phys. Rev. A **102**, 012804 (2020).

[144] M. S. Safronova, C. J. Williams, and C. W. Clark, Phys. Rev. A **69**, 022509 (2004).

[145] E. Gomez, S. Aubin, L. A. Orozco, and G. D. Sprouse, J. Opt. Soc. Am. B **21**, 2058 (2004).

[146] C. C. Kwong, *Coherent transmission of light through a cold atomic cloud*, Ph.D. thesis, Nanyang Technological University, Singapore (2017).

[147] T. Yang, K. Pandey, M. S. Pramod, F. Leroux, C. C. Kwong, E. Hajiyev, Z. Y. Chia, B. Fang, and D. Wilkowski, The European Physical Journal D **69**, 226 (2015).

[148] M. Lu, S. H. Youn, and B. L. Lev, Phys. Rev. Lett. **104**, 063001 (2010).

[149] M. Lu, N. Q. Burdick, S. H. Youn, and B. L. Lev, Phys. Rev. Lett. **107**, 190401 (2011).

[150] S. Chang and V. Minogin, Physics Reports **365**, 65 (2002).

[151] C. Zhong-Yi, *Checking of Lab Control PCBs*, Report (National University of Singapore, Singapore, 2013).

* * *